Dissertation for the Degree of Doctor of Philosophy

# System Design and Modeling of Optical Scattering Communications

by

Sudhanshu Arya

Department of Information and Communications Engineering

The Graduate School

Pukyong National University

February 2022

# System Design and Modeling of Optical Scattering Communications

# 광 산란 통신 시스템 설계 및 모델링

Advisor: Prof. Yeon Ho Chung

by

Sudhanshu Arya

A dissertation submitted in partial fulfillment of the requirements for the degree of

Doctor of Philosophy

in Department of Information and Communications Engineering,
The Graduate School,
Pukyong National University

February, 2022

# System Design and Modeling of Optical Scattering Communications

A dissertation
by
Sudhanshu Arya

Approved by:

Professor Kyu-Chil Park,
(Chairman)

Professor Sung-Man Kim,
(Member)

Professor Sunghwan Kim,
(Member)

Professor Hoon Lee,
(Member)

Professor Yeon Ho Chung,
(Member)

February, 25th, 2022

## Table of Contents

## List of Abbreviations

| | |
|---|---|
| AI | Artificial Intelligence |
| ANN | Artificial Neural Network |
| BER | Bit Error Rate |
| CDF | Cumulative Distribution Function |
| CSI | Channel State Information |
| FOV | Field-of-View |
| IR | Infrared |
| IVC | Intervehicular Communicatio |
| LOS | Line-of-Sight |
| MGF | Moment Generating Function |
| MISO | Multiple-Input Single-Output |
| MLSD | Maximum Likelihood Sequence Detection |
| MMSE | Minimum Mean Square Error |
| M-PSK | M-ary Phase-Shift Keying |
| MSE | Mean Square Error |
| MSTD | Maximum Selection Transmit Diversity |
| NLOS | Non-Line-of-Sight |
| OAM | Orbital Angular Momentum |
| OWC | Optical Wireless Communication |
| PAT | Pointing, Acquisition, and Tracking |
| PMT | Photon Multiplier Tube |
| RF | Radio Frequency |
| SINR | Signal-to-Interference-Plus-Noise Ratio |
| SNR | Signal-to-Noise Ratio |
| SSC | Switch and Stay Combining |
| UV | Ultraviolet Communication |
| V2V | Vehicular-to-Vehicular |

## List of Figures

## List of Tables

## Acknowledgment

I would like to present my gratitude primarily to my supervisor, Professor Yeon Ho Chung not only for his guidance and unconditional support but also for providing me with the opportunity to pursue the Ph.D. degree in the Mobile Transmission Systems (MTS) Laboratory at Pukyong National University, Busan, South Korea. His thorough supervision and support have enabled me to materialize my objective of successful completion of the Ph.D. degree in Korea to the greatest extent.

I extend my humble gratitude to all members of the Office of International Relations and other department offices in Pukyong National University for the facilities and supports provided for my stay in Korea.

I would like to express deep gratitude to all my colleagues in the MTS laboratory. My sincere thanks to my colleagues for their unfailing support and guidance throughout my study period.

My special and lovable thanks to my wife, Hina Tuteja, for her unstinting support and encouragement. I would like to express my benevolent thanks to my entire family, including my father, mother, all my in-laws, and my beloved friends for their words of encouragement and great love which

brought me perseverance, faith, joy, and a grateful life while being away from my country.

**Sudhanshu Arya**
Department of Information & Communication Engineering
Pukyong National University, Busan, South Korea

System Design and Modeling of Optical Scattering Communications

Sudhanshu Arya

Department of Information and Communications Engineering,
the Graduate School,
Pukyong National University

## Abstract

Demand for optical wireless communications (OWCs) is growing at a rapid pace. There is a growing interest from the commercial and the military in having secure, efficient, and high bandwidth OWC systems for tactical applications. An OWC system relies on optical wavelength, ranging from infrared to ultraviolet (UV) to convey a piece of information. With recent advances in the design and manufacturing of UV sources and detectors, optical scattering communication has attracted much interest for diverse applications. Atmospheric scattering in the deep UV band is much higher than other optical bands. This phenomenon enables establishing of a non-line-of-sight (NLOS) link. This thesis is devoted to the system design and modeling of various aspects of optical scattering communications employing ultraviolet wavelength. It provides the most comprehensive NLOS optical scattering communication systems design and modeling.

The focus of the studies discussed in the second chapter is to investigate the spatial diversity techniques for optical scattering communications. With the received signal characterized by a continuous waveform detector, the switch and stay combining (SSC) diversity technique is implemented at the receiver over correlated turbulence fading channel. Next, to avoid the requirement of an adaptive threshold in demodulating the on-off keying (OOK) symbol, the SSC diversity technique equipped with M-ary phase-shift keying (MPSK) is presented. The chapter also presents a maximal selection transmit diversity for optical scattering communications.

The third chapter presents techniques for optical spectrum sensing for distributed optical scattering communications. First, we develop an energy detection-based optical spectrum sensing for a UV network where each user is equipped with a continuous waveform detector. Second, we propose a new generic blind optical spectrum sensing technique. The proposed technique is based on finding the statistical ratio of the received continuous waveform signal. It does not require prior knowledge of the signal and noise power. Next, we propose two novel cooperative spectrum sensing techniques for optical scattering communication networks with randomly distributed collaborative users pointing in arbitrary directions. In particular, we present centralized- and decentralized-based cooperative spectrum sensing with hard decision fusion. We assume multiple scattering and characterize the received signal by the photon-counting receiver. To obtain the distribution of the received irradiance over the multi-scattering channel, a novel method based on the Mellin transform is proposed. In the centralized technique, all the raw data (in the form of statistically dependent random variables) available at the collaborative users are combined using AND rule for

decision, whereas, in the decentralized-based spectrum sensing, instead of sending all the raw data, only one-bit information is required to be sent to the fusion center to make the decision.

In the fourth chapter, we present an artificial neural network (ANN) based algorithm to estimate the data. In addition, analytical frameworks are presented to estimate the channel model parameters under different fading distributions.

In the fifth chapter, we present a novel state-of-the-art UV-based indoor optical communications. The channel model is developed and analyzed. To ensure that the UV radiations are under allowable safety exposure limits, strict peak and average power constraints are imposed. Based on the power budget, the necessary conditions for the input distribution of the intensity-modulated direct detection (IM/DD) OOK modulated signal are derived. The link gain analysis is presented to investigate the directed line-of-sight (LOS) component and diffused links with multiple reflections and NLOS scattered components. The time-delay statistics for various paths are analyzed. Next, we present a novel multiuser indoor communication over a power-constrained Poisson channel. To reject the interference from multiple users, we present a minimum mean square error (MMSE) receiver. Moreover, a downlink beamforming optimization problem is formulated using second-order cone programming to maximize the received signal-to-interference-plus-noise ratio (SINR). The proposed multiuser system is also realized in the experiment. The influence of the control parameter, that is, the average-to-peak power ratio, on the performance is investigated.

The next chapter is dedicated to implementing orbital angular momentum (OAM) with UV communications. As a method to improvise the reliability of the UV communication

system, we develop an OAM-based UV communication. Our work presents a significant increase in the UV channel capacity.

The seventh chapter presents a novel decentralized and self-organizing non-line-of-sight (NLOS) UV-based V2V communication (IVC). Experiments for proof-of-principle purposes were conducted with two vehicles in both stationary and time-varying UV channels. It is demonstrated that the proposed UV-IVC is capable of providing low-cost, low-power, and NLOS capable V2V communications with acceptable performance.

The last chapter concludes and summarizes the optical scattering communication systems developed in the previous chapters. In conclusion, the results and analysis presented in this thesis show the feasibility of employing optical scattering communication technologies in next-generation free-space optical communications. The future scope of optical scattering communications is also elaborated in the conclusion.

# 광 산란 통신 시스템 설계 및 모델링

Sudhanshu Arya

부경대학교 대학원 정보통신공학과

요약

광 무선 통신 (OWC) 에 대한 수요가 빠른 속도로 증가하고 있습니다. 전술적 애플리케이션을 위한 안전하고 효율적이며 고대역폭 OWC 시스템을 보유하는 데 대한 상업 및 군대의 관심이 증가하고 있습니다. OWC 시스템은 정보를 전달하기 위해 적외선에서 자외선 (UV) 에 이르는 광학 파장에 의존합니다. 최근 UV 소스 및 검출기의 설계 및 제조가 발전함에 따라 광학 산란 통신은 다양한 응용 분야에서 많은 관심을 끌고 있습니다. 깊은 UV 대역의 대기 산란은 다른 광학 대역보다 훨씬 높습니다. 이 현상을 통해 NLOS (Non-Line-of-Sight) 링크를 설정할 수 있습니다. 이 논문은 자외선 파장을 사용하는 광학 산란 통신의 다양한 측면의 시스템 설계 및 모델링에 전념합니다. 가장 포괄적인 NLOS 광 산란 통신 시스템 설계 및 모델링을 제공합니다.

두 번째 장에서 논의된 연구의 초점은 광학 산란 통신을 위한 공간적 다양성 기술을 조사하는 것입니다. 연속 파형 검출기를 특징으로 하는 수신 신호를 사용하여 SSC(스위치 및 스테이 결합) 다이버시티 기술은 상관된 난류 페이딩 채널을 통해

수신기에서 구현됩니다. 다음으로, OOK (On-Off Keying) 심볼을 복조할 때 적응 임계값의 요구 사항을 피하기 위해 MPSK (M-ary Phase-Shift Keying) 가 장착된 SSC 다이버시티 기술이 제시됩니다. 이 장에서는 또한 광학 산란 통신을 위한 최대 선택 전송 다이버시티를 제시합니다.

세 번째 장에서는 분산된 광학 산란 통신을 위한 광학 스펙트럼 감지 기술을 제공합니다. 첫째, 각 사용자에게 연속 파형 검출기가 장착된 UV 네트워크용 에너지 검출 기반 광학 스펙트럼 감지를 개발합니다. 둘째, 새로운 일반 블라인드 광학 스펙트럼 감지 기술을 제안합니다. 제안된 기법은 수신된 연속파형 신호의 통계적 비율을 구하는 것을 기반으로 한다. 신호 및 잡음 전력에 대한 사전 지식이 필요하지 않습니다. 다음으로, 무작위로 분산된 협업 사용자가 임의의 방향을 가리키는 광학 산란 통신 네트워크에 대한 두 가지 새로운 협업 스펙트럼 감지 기술을 제안합니다. 특히, 우리는 하드 디시전 융합을 통한 중앙 집중식 및 분산 기반 협력 스펙트럼 센싱을 제시합니다. 우리는 다중 산란을 가정하고 광자 계수 수신기에 의해 수신된 신호를 특성화합니다. 다중 산란 채널에서 수신된 복사조도의 분포를 얻기 위해 Mellin 변환을 기반으로 하는 새로운 방법이 제안됩니다. 중앙 집중식 기술에서는 협업 사용자가 사용할 수 있는 모든 원시 데이터(통계적으로 종속된 임의 변수 형태)를 AND 규칙을 사용하여 결합하여 결정하는 반면, 분산 기반 스펙트럼 감지에서는 모든 원시 데이터를 보내는 대신, 결정을 내리기 위해 1 비트 정보만 융합 센터로 보내면 됩니다.

4 장에서는 데이터 추정을 위한 인공신경망(ANN) 기반 알고리즘을 제시한다. 또한 다양한 페이딩 분포에서 채널 모델 매개변수를 추정하기 위한 분석 프레임워크가 제공됩니다.

다섯 번째 장에서는 새로운 최첨단 UV 기반 실내 광통신을 소개합니다. 채널 모델이 개발되고 분석됩니다. UV 방사선이 허용 가능한 안전 노출 제한 아래에 있도록 하기 위해 엄격한 피크 및 평균 전력 제한이 적용됩니다. 전력 예산을 기반으로 강도 변조 직접 검출(IM/DD) OOK 변조 신호의 입력 분포에 필요한 조건이 도출됩니다. 링크 이득 분석은 지향성 가시선(LOS) 구성 요소와 다중 반사 및 NLOS 산란 구성 요소가 있는 확산 링크를 조사하기 위해 제공됩니다. 다양한 경로에 대한 시간 지연 통계가 분석됩니다. 다음으로 전력이 제한된 푸아송 채널을 통한 새로운 다중 사용자 실내 통신을 제시합니다. 여러 사용자의 간섭을 거부하기 위해 최소 평균 제곱 오차 (MMSE) 수신기를 제시합니다. 더욱이, 다운링크 빔포밍 최적화 문제는 2 차 원뿔 프로그래밍을 사용하여 공식화되어 수신 신호 대 간섭 플러스 잡음 비율 (SINR) 을 최대화합니다. 제안하는 다중 사용자 시스템도 실험에서 구현된다. 제어 매개변수, 즉 평균 대 피크 전력 비율이 성능에 미치는 영향을 조사합니다.

다음 장에서는 UV 통신으로 궤도 각운동량 (OAM) 을 구현하는 데 전념합니다. UV 통신 시스템의 신뢰성을 향상시키기 위한 방법으로 OAM 기반의 UV 통신을 개발합니다. 우리의 작업은 UV 채널 용량의 상당한 증가를 나타냅니다.

일곱 번째 장은 새로운 분산 및 자체 구성 NLOS (Non-Line-of-Sight) UV 기반 V2V 통신 (IVC) 을 제시합니다. 원리 증명을 위한 실험은 고정 및 시변 UV 채널

모두에서 두 대의 차량으로 수행되었습니다. 제안된 UV-IVC 는 허용 가능한 성능으로 저비용, 저전력 및 NLOS 가능 V2V 통신을 제공할 수 있음이 입증되었습니다.

마지막 장에서는 이전 장에서 개발된 광 산란 통신 시스템을 결론짓고 요약합니다. 결론적으로 본 논문에서 제시한 결과와 분석은 차세대 자유공간 광통신에 광 산란 통신 기술을 적용할 수 있는 가능성을 보여준다. 광 산란 통신의 미래 범위도 결론에서 자세히 설명합니다.

# 1 Introduction

## 1.1 Optical Wireless Communications

Sixth-generation (6G) and beyond mobile communication systems will be developed and in use in the near future. Future mobile communication systems aim to provide uninterrupted wireless connectivity anywhere and anytime for anyone and anything. 6G applications and systems will be characterized by being bandwidth-intensive and performance-sensitive. One of the fundamental technologies for 6G and beyond will be radio frequency (RF), as it is a mature wireless technology and is being deployed in many terrestrial and indoor communication systems. However, being widely used, the RF spectrum is becoming more congested and scarce, and thus expensive to accommodate. To meet ample data rate requirements of future wireless communication systems, there is a need for new and orthogonal communication technologies that could be used in combination with existing wireless RF technologies. Recently, optical wireless communications (OWCs) is being extensively investigated as an attractive alternative technology to RF [1].

Optical wireless communication (OWC) refers to the transmission of information in an unguided propagation channel by utilizing optical carriers with wavelengths ranging from ultraviolet (UV) to visible light to infrared (IR).

Compared with the communication system that relies on radio frequency (RF) to convey information, the potential advantages of employing optical wavelengths are, for example, huge unlimited bandwidth, higher power densities, high channel capacity, and miniaturized transceiver circuits with low transmit power [2].

The OWC systems can broadly be classified into two categories: indoor and outdoor OWC systems, as illustrated in Figure 1.1. Indoor optical communications employ visible light or IR to convey information via different kinds of links. Outdoor optical wireless communication (commonly known as free-space optical (FSO) communication) can be further classified into two categories, namely, terrestrial and space optical links [3].

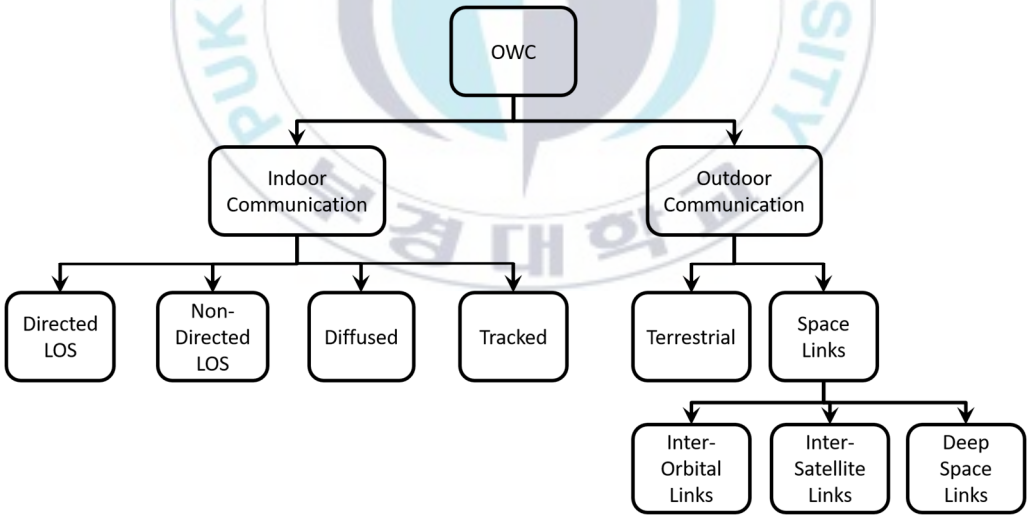


Figure 1.1 Classification of the OWC systems.

## 1.2 Optical Scattering Communications

The application of optical scattering communications for non-line-of-sight (NLOS) links has recently attracted increasing interest because of its robustness against shadowing and relatively insensitivity to pointing errors [4]. Optical scattering communication (commonly known as ultraviolet communication) utilizes UV wavelength as a communication medium. The motivation for the deployment of optical scattering communication includes unique channel characteristics that enable NLOS link establishment and recent advancement and commercialization of solid-state device technology. The UV spectrum can be loosely classified into four different subbands, as illustrated in Figure 1.2. That is, they are extreme UV band (EUV) (4 ~ 100 nm), far UV band (FUV) (100 ~ 200 nm), mid UV band (MUV) (200 ~ 300 nm), and near UV band (NUV) (300 ~ 400 nm) [5]. The NUV band is part of the solar UV spectrum, and the EUV spectrum includes wavelengths that are strongly attenuated by the atmosphere due to high absorption. Within the entire UV band (4 ~ 400 nm), UV-C band (200 ~ 280 nm) (also known as the deep UV band) is solar blind at the ground due to the ozone absorption in the upper atmosphere. An optical scattering communication operating under the UV-C band can approach quantum-limited photon-counting detection performance, and therefore, can operate with low-power sources [6].

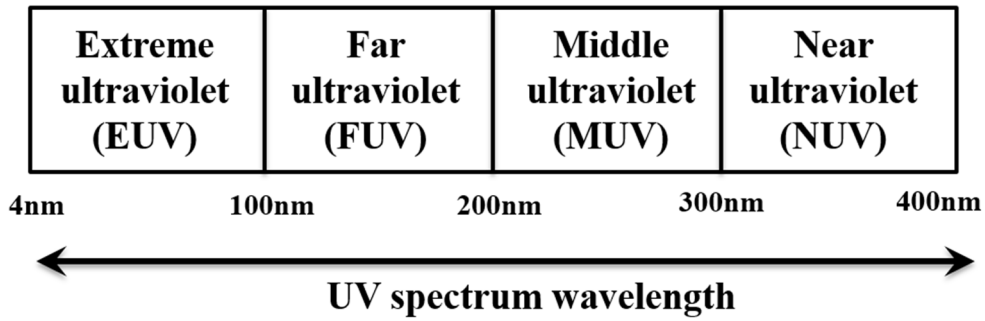


Figure 1.2 Classification of the UV spectrum.

### 1.2.1 Atmospheric Scattering of UV Signal

In optical scattering communications, strong atmospheric scattering occurs, which facilitates the means of transferring information from the transmitter to the receiver when the line-of-sight (LOS) condition does not exist. The molecular scattering of the UV signal provides an indirect propagation link from the transmitter to the receiver.

A high degree of relatively angle-independent scattering occurs due to the interaction of the UV photons with the atmospheric particles, thereby creating multiple NLOS diverse communication links from the transmitter to the receiver [6]. UV wavelengths undergo strong atmospheric absorption and rich scattering. A typical UV-based single-scattering NLOS transmission link over coplanar geometry is illustrated in Figure 1.3.

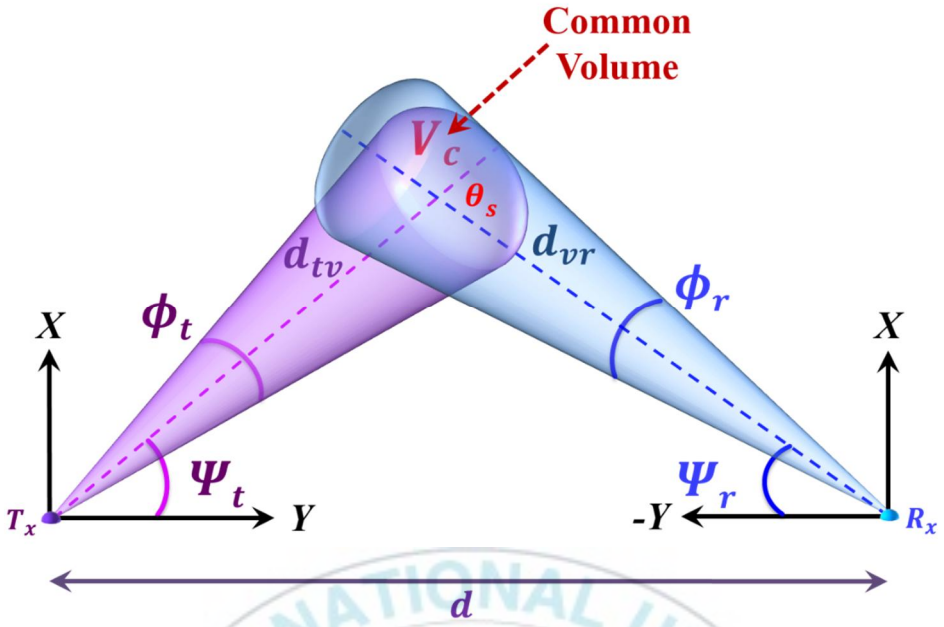


Figure 1.3 NLOS UV communication coplanar link geometry, depicting the single-scattering event.

In Figure 1.3, $T_x$ is the transmitter and $R_x$ is the receiver. $\phi_t$ and $\phi_r$ are the transmit beam angle and the receiver FOV, respectively. $\psi_t$ and $\psi_r$ are the transmitter and the receiver elevation angle. $d$ is the baseline distance between $T_x$ and $R_x$. $V_c$, known as the common volume, is formed by the overlapping of the transmit beam and the receiver FOV. $d_{tv}$ and $d_{vr}$ are the distances from the transmitter to the common volume and from the common volume to the receiver, respectively.

Particle scattering of the UV signal consists of Mie scattering and Rayleigh scattering, as shown in Figure 1.4.

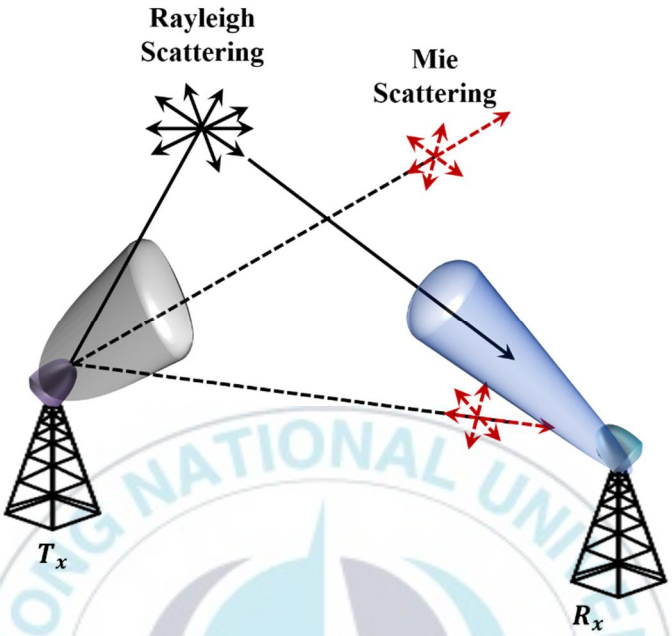


Figure 1.4 Particle scattering of the UV signal.

In the Mie scattering, the scattered light is largely focused in the forward direction. In the Rayleigh scattering, however, the UV light is scattered uniformly in all directions [7, 8]. Rayleigh scattering occurs when the particle size is much less than the UV wavelength, such as air molecules. Mie scattering generally occurs when the UV photon interacts with the suspended particles with dimensions comparable to or larger than the transmitted UV wavelength. The NLOS UV communication performance is determined by the scattering and absorption, which, in turn, is determined by the atmospheric particle density,

dimension distribution, and refractive index. When the aerosol particles (air molecules) size is relatively smaller than the wavelength of the signal, the Rayleigh scattering dominates the Mie scattering and facilitates the NLOS scattering communication link [8].

The total attenuation of the UV signal in the atmosphere is due to the component from the scattering and due to the atmospheric absorption, as shown in Figure 1.5. For wavelengths less than 200 nm, the atmospheric absorption is

very strong and propagation is severely impaired; therefore, it is not feasible to operate below 200 nm.

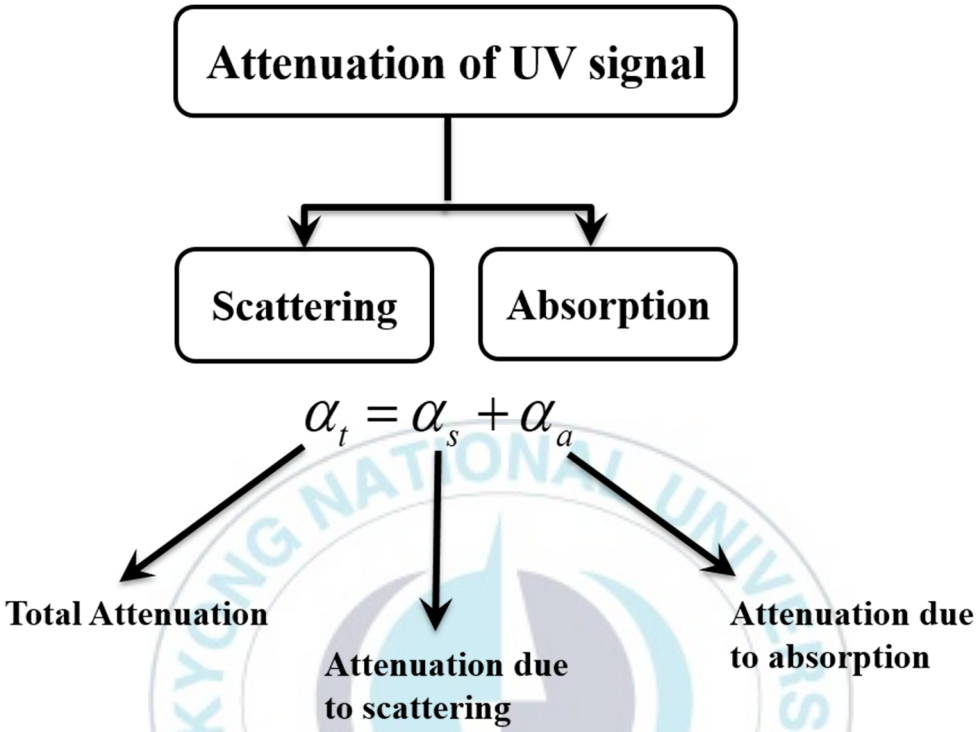


Figure 1.5 Types of attenuations in optical scattering communications.

### 1.2.2 Common Volume and UV Channel Bandwidth

Based on the overlapping of the transmit beam and receiver FOV, the following cases may arise. As shown in Figure 1.6, Case I corresponds to the unbounded common volume and yields the lowest transmission bandwidth [6]. In Case II, the common volume is bounded due to the narrow transmit beam pointing towards the receiver FOV. The width of the temporal distribution in

Case II is narrow than that in Case I and yields a channel bandwidth higher than that in Case I. Case III, where both the transmit beam and the receiver FOV are pointing towards each other and form a bounded common volume, yields a maximum channel bandwidth.

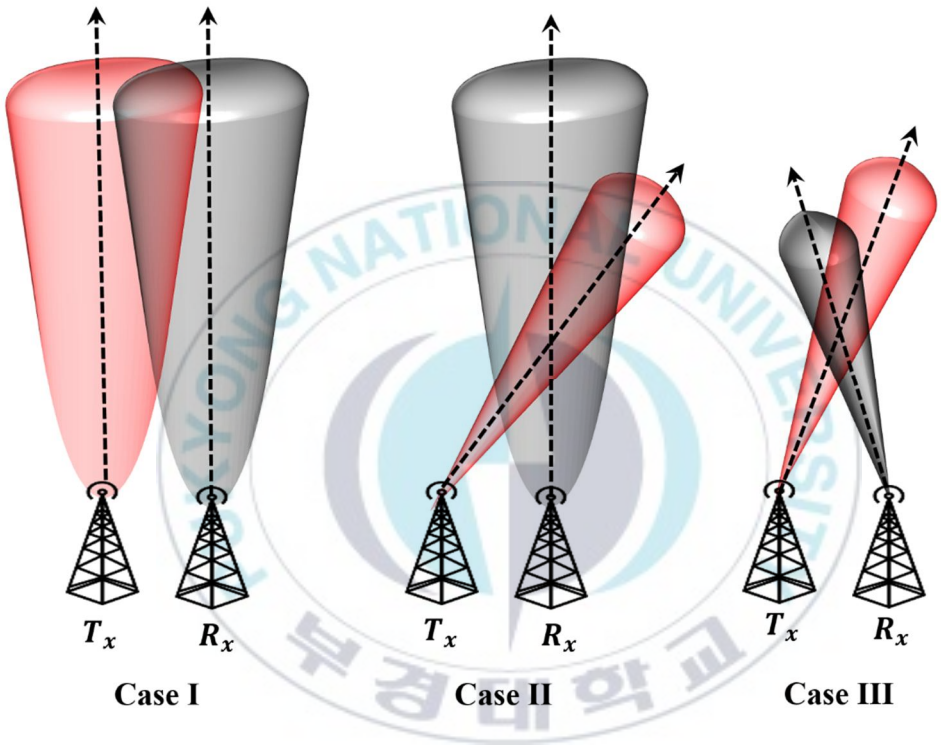


Figure 1.6 NLOS optical scattering link configurations.

### 1.2.3 UV Safety Exposure Limit

The intensity of the radiations from the UV source is measured in the unit of milliwatts per square centimeter ($mW/cm^2$), which is the received energy per

square centimeter per second. It is also analyzed in the unit of millijoules per square centimeter ($mJ/cm^2$), which is the received energy per unit area in a given time. The level of the UV radiations a human can receive on their eyes and skin for a given time duration varies with the wavelength of the UV radiation.

The International Commission on Non-Ionizing Radiation Protection [9] and the International Electrotechnical Commission [10] govern UV radiation exposure power limits. In the UV-C band, the allowable continuous exposure limits at 200 nm, 270 nm, and 280 nm are 100, 3, and 3.4 mJ per $cm^2$ for an eight-hour exposure, respectively. Therefore, the minimum allowable continuous exposure occurs at 270 nm. In addition, as reported in [5, 11], for continuous UV exposure, the maximum allowable UV power limit is 0.1 $\mu W$ per $cm^2$, and for the UV exposure less than 7 hours, it is 0.5 $\mu W$ per $cm^2$.

The National Institute for Occupational Safety and Health (NIOSH) also proposed the UV exposure standard for conventional UV sources [12]. This standard is based on an envelope action spectrum which combines the action spectra for photokeratitis with Caucasian skin erythema over a high sensitive UV wavelength range, that is, 200 nm to 315 nm. The recommended standard says 4.6 mJ per $cm^2$ as the maximum safe or permissible exposure to 260 nm and 4.7 mJ per $cm^2$ corresponding to 290 nm. As defined by this standard, any exposure

that is below these limits is considered to be safe for humans. These are important safety considerations that a UV-based communication system design should follow.

### 1.3 Motivation

In the recent past, infrared and visible light communications have shown significant progress in the optical wireless communications domain. The infrared communication may provide low-power and low-cost implementation, however, infrared links are vulnerable to blockage, due to their directionality [13]. Though VLC offers information transmission in addition to illumination, establishing an efficient uplink for VLC is difficult. In addition, artificial light sources, like a fluorescent lamp, and the light from the natural sources produce interference and may result in receiver saturation. The UV-based optical scattering communication overcomes basic limitations and eliminates the requirement of pointing, acquisition, and tracking (PAT), and accommodates the NLOS conditions. Moreover, communication via the UV-C band is less sensitive to the interference from the solar and background illumination. Another important aspect is security. The higher atmospheric attenuation makes the UV signal beyond a certain extinction range difficult to intercept. This enables UV communication to find applications in the tactical domain. Moreover, a huge unlicensed spectrum makes UV-C a potential candidate that may facilitate low-

power applications with high data rate requirements. Therefore, for communication applications that require minimum implementation cost, low power, NLOS operability, and security, UV-C-based optical scattering communication is ideal. Consequently, it inspires us to develop state-of-the-art UV communication systems that can offer the potential of small-size, high data rate, low power, low cost, and high reliability.

### 1.4 Dissertation Organization

The first chapter introduces the fundamentals and the propagation concepts of optical scattering communication employing UV wavelength. The second chapter of the dissertation presents various spatial diversity techniques for NLOS UV communications. In the third chapter, we develop optical spectrum sensing techniques for continuous waveform detectors and photon-counting receivers. The fourth chapter investigates the applications of the artificial neural network (ANN), artificial intelligence (AI), and Game Theory in the context of UV communications. The state-of-the-art UV-based indoor communication is presented in the fifth chapter. The orbital angular momentum (OAM) based UV communication is presented in Chapter 6. The seventh chapter finally concludes the findings in the dissertation.

# 2 Diversity Techniques for Optical Scattering Communications

The primary purpose of this chapter is to introduce diversity techniques for optical scattering communications. In particular, we focus on the performance evaluation of the NLOS optical scattering communications when employed with the switch-and-stay combing (SSC) and maximal selective transmit diversity techniques. More comprehensive and in-depth treatments that include analytical and numerical results can be found in [14, 15, 16, 17].

The remainder of this chapter is organized as follows. In the next section, we present the SSC diversity technique for UV communications. Based on the two different modulation techniques, that is, on-off keying (OOK) and M-arry phase-shift keying (MPSK), we derive the average bit error rate (BER) and the outage probability over Gamma-Gamma distributed turbulence-induced fading.

## 2.1 Spatial Diversity

Many of the emerging and current free-space optical communication systems make use in one form or another of diversity to combat the channel impairment due to the turbulence-induced fading. Indeed, diversity combining, in which two or more branches carrying the same signal are combined to increase the received signal power, offers the potentials to increase the optical link performance [18].

## 2.2 Switch and Stay Combining

We investigate the switch and stay combining (SSC) diversity for NLOS UV communications to mitigate the channel impairment due the turbulence-induced fading. We consider dual-branch SSC receive diversity with each branch assumed to be exponentially correlated with another branch. The received signal is characterized by a continuous waveform detector.

### 2.2.1 System Model

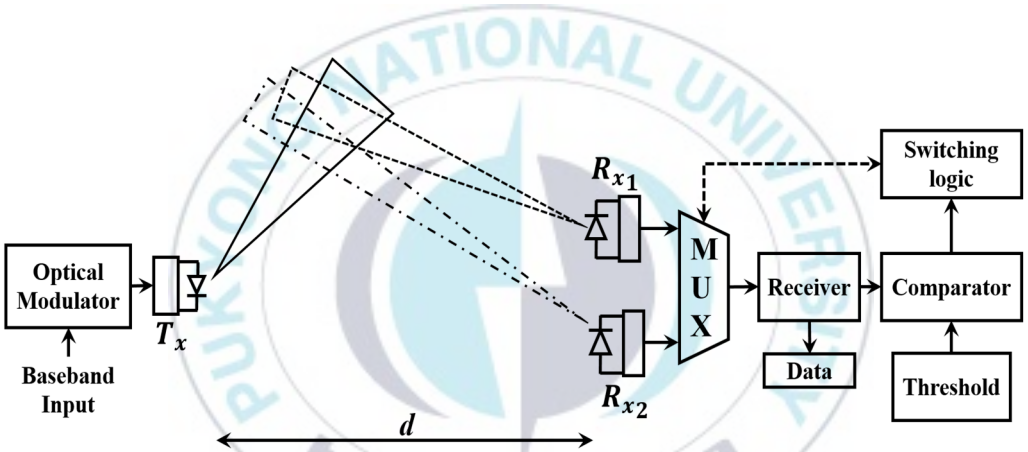


Figure 2.1 Dual-branch exponentially correlated SSC for NLOS optical scattering communications.

The proposed system utilizing dual-branch switch and stay combining spatial diversity is illustrated in Figure 2.1. The working principle of the proposed system is based on the idea of selecting a particular link until its SNR falls below a predetermined threshold value, rather than continually picking the

best link. The comparator block compares the received optical signal with the threshold $\gamma_{Th}$, and, for instance, at any particular time instant, if the switching logic is locked at $R_{x_1}$, the switching logic will then switch to $R_{x_2}$, if the SNR of branch 1 falls below the predetermined threshold value.

The received signal is modeled as

$$y_i = SP_{r,NLOS} I_i + n_i, \quad i = 1, \cdots, L, \tag{2.1}$$

where $S$ is the responsivity of the detector, $P_{r,NLOS}$ is the deterministic received power with a single-scattering assumption. $n_i, i \in \{1, 2\}$ is the additive white Gaussian noise (AWGN) at the detector of the $i$th branch. The received power $P_{r,NLOS}$ accounts for the molecular absorption and Rayleigh and Mie scattering [5]. $I_i$ is the irradiance corresponds to the $i$th branch and is modeled as Gamma-Gamma distributed random variable with $E[I_i] = 1,\ i \in \{1, 2\}$, where $E[\cdot]$ denotes the expectation operation.

### 2.2.2 Performance Analysis

We derive the closed-form expression for the outage probability and the average BER. The outage probability is derived as

$$P_{out} = F_{SSC}\left(\gamma_{Th}\right) = \frac{\left(1-\rho\right)^2}{4\left[\Gamma\left(\alpha\right)\right]^2\Gamma\left(\beta\right)}\sum_{l=0}^{\infty}\frac{\rho^{2l}}{\Gamma\left(\beta+l\right)l!} \times\left\{G_{1,3}^{2,1}\left(\sqrt{\frac{\Xi^2\gamma_{Th}}{\gamma_{avg}}}\middle|\begin{matrix}\frac{\alpha+\beta+l+4}{4}\\ \beta+l,\alpha,\frac{\alpha+\beta+l}{4}\end{matrix}\right)\right\}, \quad (2.2)$$

where $F_{SSC}(\cdot)$ is the cumulative distribution function (CDF) of the received SNR at the combiner output. $\alpha$ and $\beta$ are the model parameters for the Gamma-Gamma distributed turbulence fading. We consider the spherical wave propagation. $G_{u,v}^{s,t}(\cdot)$ is the Meijer G-function. $\gamma_{avg}$ is the average received SNR. $\Xi$ is given by $\Xi = \frac{\alpha\beta}{\{E[I](1-\rho^2)\}}$ and $\rho, 0 \leq \rho < 1$, is the power correlation coefficient with $\rho^{|i-j|}$ denoting the correlation coefficient between the $i$th and the $j$th branch. Similarly, we obtain the closed-form expression for the average BER, as illustrated in Equation (2.3).

$$P_{e,avg} = \frac{(1-\rho)^2}{16\pi^{3/2}\left[\Gamma(\alpha)\right]^2\Gamma(\beta)}\sum_{l=0}^{\infty}\frac{\rho^{2l}}{\Gamma(\beta+l)l!}$$
$$\times 2^{(\alpha+\beta+l)} G_{1,3}^{2,1}\left(\sqrt{\frac{\Xi^2\gamma_{Th}}{\gamma_{avg}}}\middle|\begin{matrix}\alpha+\beta+l+1\\ \beta+l,\alpha,0\end{matrix}\right)$$
$$\times G_{2,5}^{4,2}\left(\frac{\Xi^2}{2\gamma_{avg}}\middle|\begin{matrix}1,\frac{4-\alpha-\beta-l}{4}\\ \frac{\beta+l}{2},\frac{\beta+l+1}{2},\frac{\alpha}{2},\frac{\alpha+1}{2},0\end{matrix}\right)$$
$$+\left(\frac{1}{16}\right)^{\alpha+\beta}\frac{1}{\pi^{3/2}\Gamma(\alpha)\Gamma(\beta)}$$
$$\times G_{2,5}^{4,2}\left(\frac{\Xi^2}{2\gamma_{avg}}\middle|\begin{matrix}1,\frac{4-\alpha-\beta}{4}\\ \frac{3\alpha-\beta}{4},\frac{3\alpha-\beta+4}{4},\frac{3\beta-\alpha}{4},\frac{3\beta-\alpha+4}{4},\frac{\alpha+\beta}{2}\end{matrix}\right) \quad (2.3)$$

### 2.2.3 Results and Discussions

The simulation parameters are illustrated in Table 2.1. We assume the isotropic scattering.

Table 2.1 Simulation Parameters.

| Parameter | Value |
|---|---|

| | |
|---|---|
| UV wavelength $\lambda$ | 260 nm |
| Visibility $v$ | 21 km |
| Refractive index structure parameter $C_n^2$ | $6 \times 10^{-15}$ m$^{-\frac{2}{3}}$ |
| Correlation coefficient $\rho$ | 0.4 |
| Transmitter apex angle | $\frac{\pi}{6}$ radian |
| Receiver apex angle | $\frac{\pi}{4}$ radian |
| Transmit beam angle | $\frac{\pi}{180}$ radian |
| Receiver FOV | $\frac{\pi}{3}$ radian |
| Threshold SNR $\gamma_{Th}$ | 4 dB |
| Aperture diameter $R$ | $5 \times 10^{-2}$ m |
| Absorption coefficient $\alpha_a$ | 0.802 km$^{-1}$ |
| Molecular density $N$ | $2.4481 \times 10^{25}$ m$^{-3}$ |
| Depolarization ratio $\rho_\mu$ [19] | $3.501 \times 10^{-2}$ |

The system performance in terms of the outage probability for exponentially correlated Gamma-Gamma distributed turbulence fading channels is illustrated in Figure 2.2. The performance is investigated for different SNR and baseline distance values.

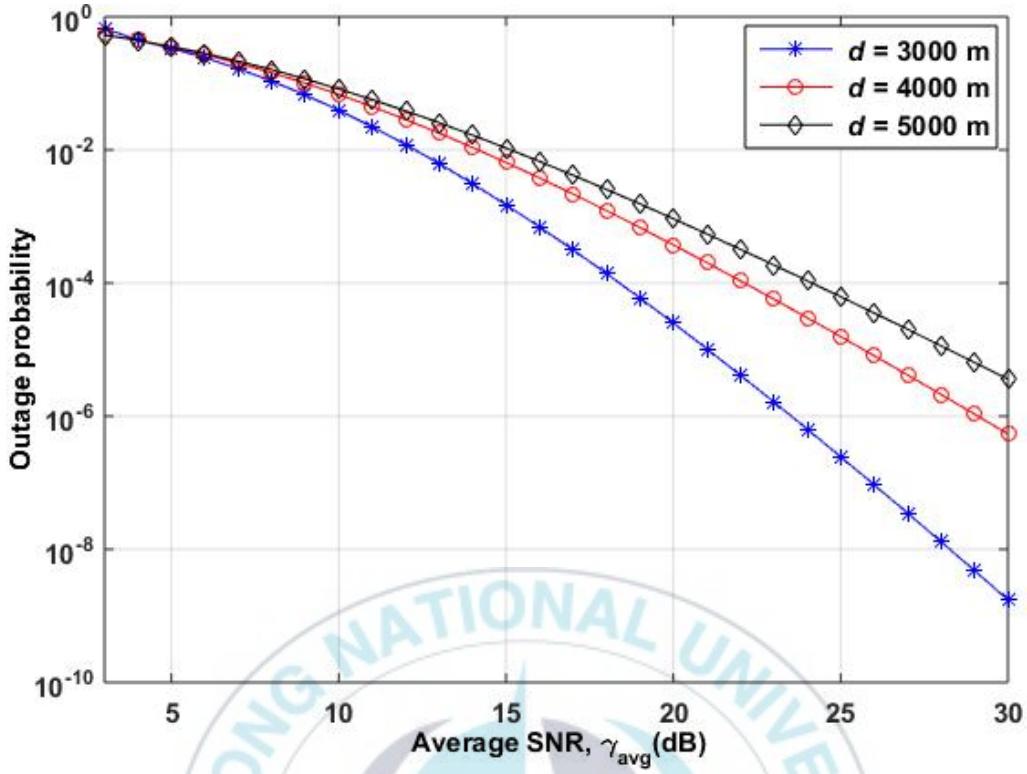


Figure 2.2 Outage probability against the average received SNR for different baseline distances.

The impact of the correlation on the outage probability is shown in Figure 2.3. The baseline distance $d$ is set to 4000 m. It is interesting to note that for the uncorrelated branches, the performance of the SSC diversity technique outperformed the similar system with correlated branches ($\rho = 0.4$) by approximately 2 dB. Moreover, to validate the importance of the SSC for the NLOS UV communications, its performance is compared with the receiver with

no diversity employed. It can be seen that the SSC-based receiver outperforms by 5 dB and 7 dB for $\rho = 0.4$ and $\rho = 0$, respectively.

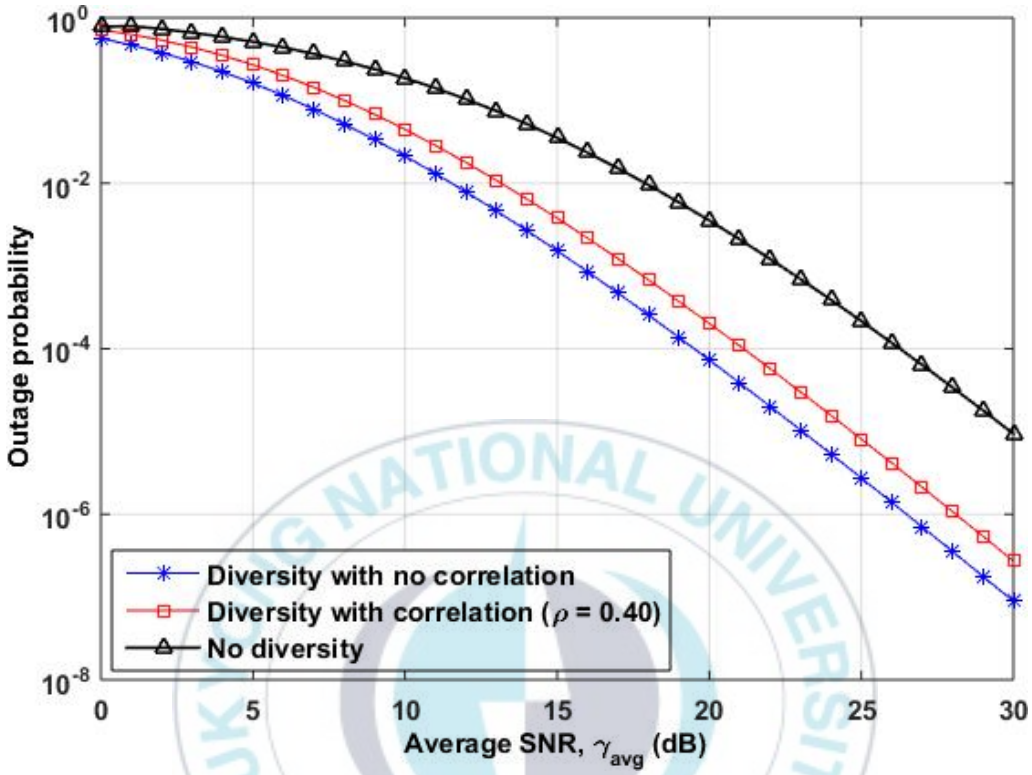


Figure 2.3 Impact of the correlated branches on the system performance.

For the correlated dual branch ($\rho = 0.4$) SSC diversity technique, the average BER performance relative to the switching threshold $\gamma_{Th}$ for different SNR values is depicted in Figure 2.5. The baseline distance is set to 4000 m.

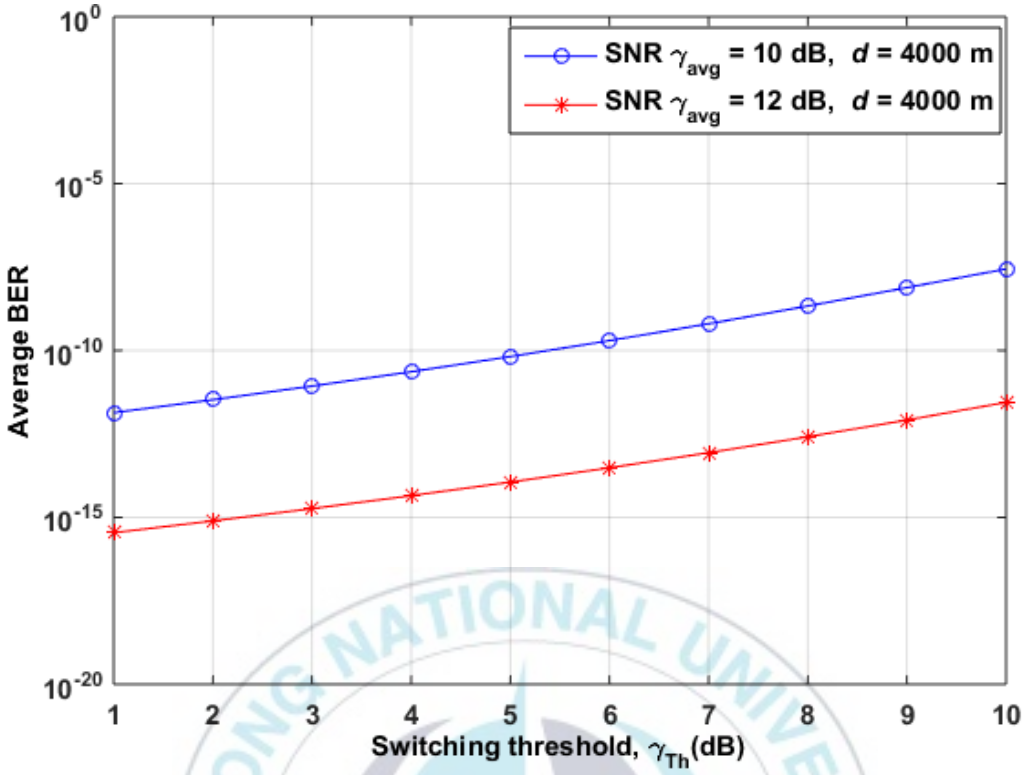


Figure 2.4 Average BER against the switching threshold.

## 2.3 Switch and Stay Combining with M-PSK Subcarrier Intensity Modulation

One of the major challenges facing optical wireless communication systems in a clear atmosphere is fluctuation in the received intensity due to the turbulence-induced fading. This scintillation is due to temperature fluctuation (0.01 to 0.1 degree) on the spatial scale of 0.1 cm to 10 m, which, in turn, results in fluctuations in the refractive index of the atmosphere [20, 21]. The OOK modulation is a widely accepted transmission scheme for OWC links. However, over the turbulence channel, the OOK modulation requires an adaptive threshold at the detector for optimal performance. This, however, makes the detection process difficult [21]. To alleviate this problem, we consider a SSC spatial diversity technique equipped with M-ary phase-shift keying (M-PSK).

### 2.3.1 System Model

The proposed NLOS optical scattering communication system equipped with the M-PSK subcarrier intensity modulation assisted dual branch SSC diversity technique is illustrated in Figure 2.5. We consider exponentially correlated branches. The turbulence-induced fading is modeled as Gamma-Gamma distribution. The binary information data is modulated on the RF subcarrier, which in turn, modulates the intensity of the continuous wave UV

signal. A DC bias is applied to eliminate the impact of the negative cycles of the pre-modulated sinusoidal RF signal.

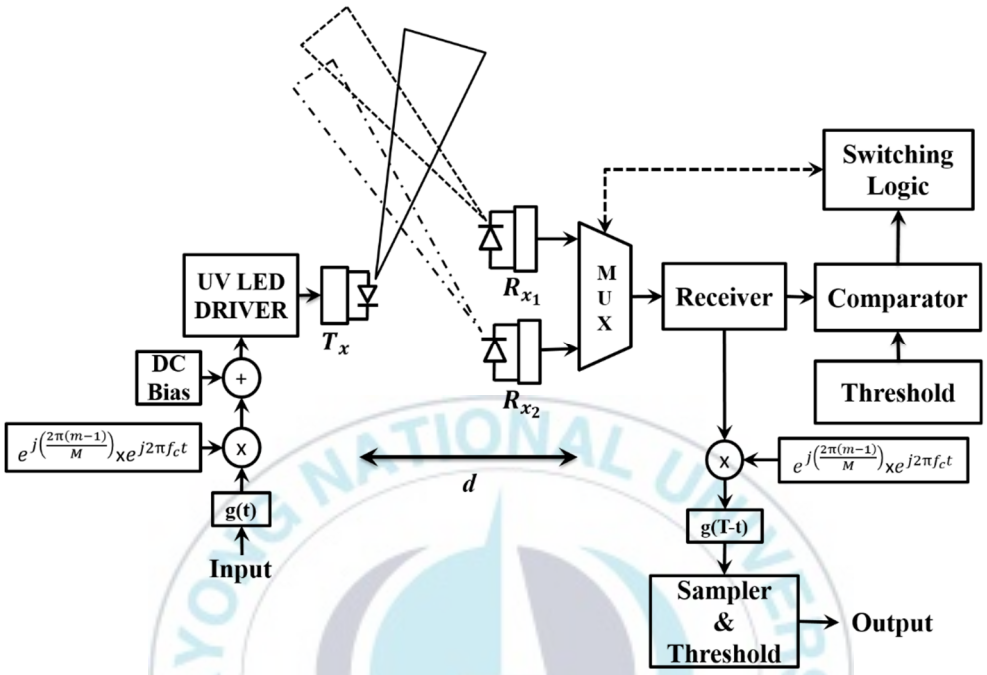


Figure 2.5 Correlated dual branch SSC diversity technique equipped with M-PSK subcarrier intensity modulation.

The pre-modulated RF signal is converted into a UV signal by modulating the current of the driver circuit. The power of the transmitted optical signal can then be given by [21]

$$P_t(t) = P_{t0}\left\{1 + m_d\, g(t)\cos\left[2\pi f_c t - \frac{2\pi}{M}(m-1)\right]\right\}, \qquad (2.4)$$

where $P_{t0}$ represents the power of the transmitted optical signal with $m_d = 0$, where $m_d$ is the modulation index. $g(t)$ denotes the pulse-shaping filter and the value of $m \in \{1,\cdots,M\}$ depends upon the symbol mapping. $M$ represents the order of the modulation. The instantaneous received optical power $P_{r,NLOS}$ over an NLOS UV link is then given by $P_{r,NLOS} = P_t(t) \times P_L$, where $P_L$ is the deterministic NLOS path loss. We assume that all the emitted UV photons are scattered only once before falling into the receiver's FOV. The instantaneous photocurrent at the detector of the $i$th branch, $i \in \{1,2\}$, is given by

$$y_i(t) = SG_r P_{r,NLOS} I_i + n_i(t), \tag{2.5}$$

where $S$ is the responsivity of the detector in A/W, $G_r$ is the gain of the detector, and $n_i(t)$ is the AWGN with zero-mean and uniform power spectral density $\frac{N_0}{2}$. $I_i$ accounts for the scintillation fading and is modeled as Gamma-Gamma distribution.

The M-PSK subcarrier intensity-modulated optical signals received over different branches are correlated due to the proximity of the detectors. The fading correlation arises due partially from small-scale and partly from large-scale turbulent eddies. The autocorrelation matrix with elements being the correlation coefficients is given by [22]

$$\mathbf{R}_{\rho} = \frac{\alpha \mathbf{R}_L + \beta \mathbf{R}_S + \mathbf{R}_S \square \mathbf{R}_L}{\alpha + \beta + 1}, \tag{2.6}$$

where $\mathbf{R}_S$ and $\mathbf{R}_L$ are the autocorrelation matrices of small- and large-scale fading coefficients, respectively. The joint PDF of the instantaneous SNR is derived as

$$f_{\gamma_1,\gamma_2}(\gamma_1,\gamma_2) = \frac{\left(1-\rho^2\right)^{\beta}}{4\left[\Gamma(\alpha)\right]^2\Gamma(\beta)} \sum_{l=0}^{\infty} \left( \frac{\Xi}{\sqrt{\gamma_{avg}}} \right) \frac{\rho^{2l}}{\Gamma(\beta+l)l!}$$
$$\times \gamma_1^{\frac{(\alpha+\beta+l-4)}{4}} G_{0,2}^{2,0}\left( \sqrt{\frac{\Xi\gamma_1}{\gamma_{avg}}} \middle| \begin{matrix} - \\ \frac{\beta+l-\alpha}{2}, \frac{\beta+l-\alpha}{2} \end{matrix} \right) ,$$
$$\times \gamma_2^{\frac{(\alpha+\beta+l-4)}{4}} G_{0,2}^{2,0}\left( \sqrt{\frac{\Xi\gamma_2}{\gamma_{avg}}} \middle| \begin{matrix} - \\ \frac{\beta+l-\alpha}{2}, \frac{\beta+l-\alpha}{2} \end{matrix} \right) \tag{2.7}$$

where $\gamma_i, i \in \{1,2\}$ is the instantaneous received SNR at the $i$th branch. $\gamma_{avg}$ denotes the average received SNR. $\rho$ is the correlation coefficient. $\Xi = \frac{\alpha\beta}{\{E[I](1-\rho^2)\}}$. $\alpha$ and $\beta$ are the model parameters of the Gamma-Gamma distribution.

### 2.3.2 Average Bit Error Rate

The average BER of the proposed system can be obtained as

$$P_{e,avg} = \int_0^{\infty} P_e f_{SSC}(\gamma) d\gamma , \tag{2.8}$$

where $P_e = \text{erfc}\left(\sqrt{\sin^2\left(\frac{\pi}{M}\right)\gamma}\right)$ and $f_{SSC}(\gamma)$ is the PDF of the instantaneous received SNR at the output of the detector [23]

$$f_{SSC}(\gamma) = \begin{cases} g_\gamma(\gamma_{Th}, \gamma), & \gamma \le \gamma_{Th} \\ f_\gamma(\gamma) + g_\gamma(\gamma_{Th}, \gamma), & \gamma > \gamma_{Th} \end{cases} . \tag{2.9}$$

$f_\gamma(\gamma)$ denotes the marginal PDF of the received SNR and $g_\gamma(\gamma_{Th}, \gamma)$ is given by

$$g_\gamma(\gamma_{Th}, \gamma) = \int_0^{\gamma_{Th}} f_{\gamma_1,\gamma_2}(\gamma, \gamma_2) d\gamma_2 . \tag{2.10}$$

$\gamma_{Th}$ is the switching threshold. Utilizing Equations (2.7), (2.8), (2.9), and (2.10), the closed-form expression of the average BER is derived as

$$P_{e,avg} = \frac{\left(1-\rho^2\right)^{\beta}}{\pi^{3/2}\left[\Gamma(\alpha)\right]^2\Gamma(\beta)}\sum_{l=0}^{\infty}\frac{\rho^{2l}}{\Gamma(\beta+l)l!}$$

$$\times 2^{(\alpha+\beta+l-3)} G_{1,3}^{2,1}\left(\sqrt{\frac{\Xi^2\gamma_{Th}}{\gamma_{avg}}}\,\middle|\, \begin{matrix} 1+\frac{(\alpha+\beta+l)}{4} \\ \beta+1,\alpha,\frac{(\alpha+\beta+l)}{4}\end{matrix}\right)$$

$$\times G_{2,5}^{4,2}\left(\frac{\Xi^2}{4\sin\left(\frac{\pi}{M}\right)\sqrt{\gamma_{avg}}}\,\middle|\, \begin{matrix} 1,\frac{1}{2} \\ \frac{\beta+l}{2},\frac{\beta+l+1}{2},\frac{\alpha}{2},\frac{\alpha+1}{2},0\end{matrix}\right). \quad (2.11)$$

### 2.3.3 Outage Probability

The CDF of the instantaneous received SNR at the output of the SSC receiver is given by

$$F_{SSC}(\gamma) = \begin{cases} F_{\gamma_1,\gamma_2}(\gamma,\gamma_{Th}), & \gamma \le \gamma_{Th} \\ F_{\gamma_1}(\gamma) - F_{\gamma_1}(\gamma_{Th}) + F_{\gamma_1,\gamma_2}(\gamma,\gamma_{Th}), & \gamma > \gamma_{Th} \end{cases}, \quad (2.12)$$

where $F_{\gamma}(\gamma)$ is the CDF of the received SNR. $F_{\gamma_1,\gamma_2}(\gamma,\gamma_{Th})$ is expressed as

$$F_{\gamma_1,\gamma_2}(\gamma,\gamma_{Th}) = \int_0^{\gamma}\int_0^{\gamma_{Th}} f_{\gamma_1,\gamma_2}(\gamma_1,\gamma_2)\,d\gamma_1 d\gamma_2, \quad (2.13)$$

where $f_{\gamma_1,\gamma_2}(\gamma_1,\gamma_2)$ is defined in Equation (2.7).

The outage probability is defined as $P_{out} = F_{SSC}(\gamma_{Th,out})$, where $\gamma_{Th,out}$ is the outage threshold. Utilizing Equations (2.7), (2.12), and (2.13), the closed-form expression for the outage probability is derived as

$$P_{out} = F_{SSC}\left(\gamma_{Th,out}\right) = \frac{\left(1-\rho^2\right)^{\beta}}{4\left[\Gamma(\alpha)\right]^2\Gamma(\beta)}\sum_{l=0}^{\infty}\frac{\rho^{2l}}{\Gamma(\beta+l)l!} \times G_{1,3}^{2,1}\left(\sqrt{\frac{\Xi^2\gamma_{Th}}{\gamma_{avg}}}\middle| \begin{matrix}\frac{\alpha+\beta+l+4}{4} \\ \beta+l,\alpha,\frac{\alpha+\beta+l}{4}\end{matrix}\right) \times G_{1,3}^{2,1}\left(\sqrt{\frac{\Xi^2\gamma_{Th,out}}{\gamma_{avg}}}\middle| \begin{matrix}\frac{\alpha+\beta+l+4}{4} \\ \beta+l,\alpha,\frac{\alpha+\beta+l}{4}\end{matrix}\right), \gamma_{Th,out} \le \gamma_{Th} \quad (2.14)$$

### 2.3.4 Results and Discussions

The simulation parameters are illustrated in Table 2.2. We assume the isotropic scattering. Unless otherwise stated, the switching threshold $\gamma_{Th}$ is set equal to the average received SNR $\gamma_{avg}$.

Table 2.2 Simulation Parameters.

| Parameter | Value |
|---|---|
| UV wavelength $\lambda$ | 260 nm |
| Visibility $v$ | 21 km |
| Refractive index structure parameter $C_n^2$ | $5 \times 10^{-14}$ m$^{-\frac{2}{3}}$ |
| Correlation coefficient $\rho$ | 0.4 |
| Transmitter apex angle | $\frac{\pi}{3}$ |
| Receiver apex angle | $\frac{\pi}{3}$ |
| Transmit beam angle | $\frac{\pi}{180}$ |
| Receiver FOV | $\frac{\pi}{3}$ |
| Gain $G_r$ | 1 |
| Threshold SNR $\gamma_{Th}$ | 4 dB |
| Absorption coefficient $\alpha_a$ | 0.802 km$^{-1}$ |
| Molecular density $N$ | $2.4481 \times 10^{25}$ m$^{-3}$ |
| Air pressure | 1013 hPa |
| Depolarization ratio $\rho_\mu$ [19] | $3.501 \times 10^{-2}$ |
| $\rho_S$ | 0.45 |
| $\rho_L$ | 0.30 |

The average BER performance against the SNR is illustrated in Figure 2.6. The curves are obtained for $M = 2$ and $M = 4$. As expected, as the constellation size increases, the BER increases. For the given BER, the received SNR required for $M = 2$ is approximately 1.5 dB less than the one required for $M = 4$. It can be accounted for from the fact that the BER is given by $P_e = \text{erfc}\left(\sqrt{\sin^2\left(\frac{\pi}{M}\right)\gamma}\right)$, and, since $\text{erfc}(x)$ is a decreasing function of $x$, increasing $M$ leads to decreasing argument of the $\text{erfc}(\cdot)$, which in turn, increases the BER.

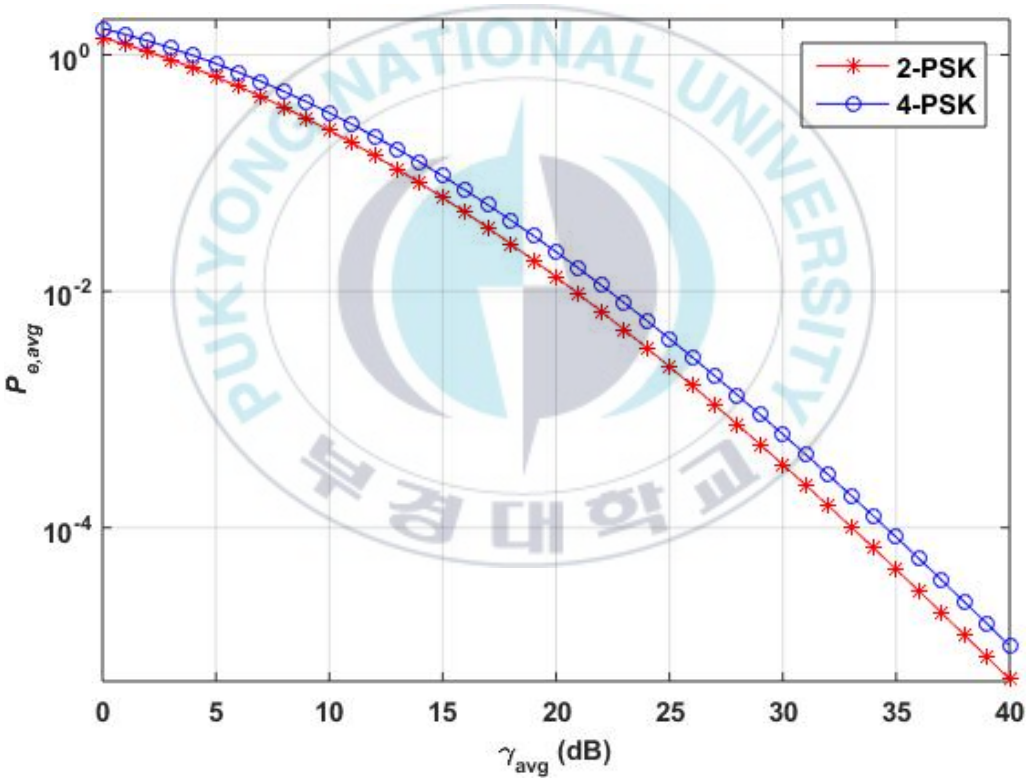


Figure 2.6 Average BER relative to the average received SNR for different $M$.

The BER as a function of the modulation depth is illustrated in Figure 2.7. The transmit power $P_t$ is set to 1 W. As depicted, as the modulation depth increases, the BER reduces. This can be attributed to the fact that an increase in $m_d$ yields a higher received SNR, thereby reducing the BER.

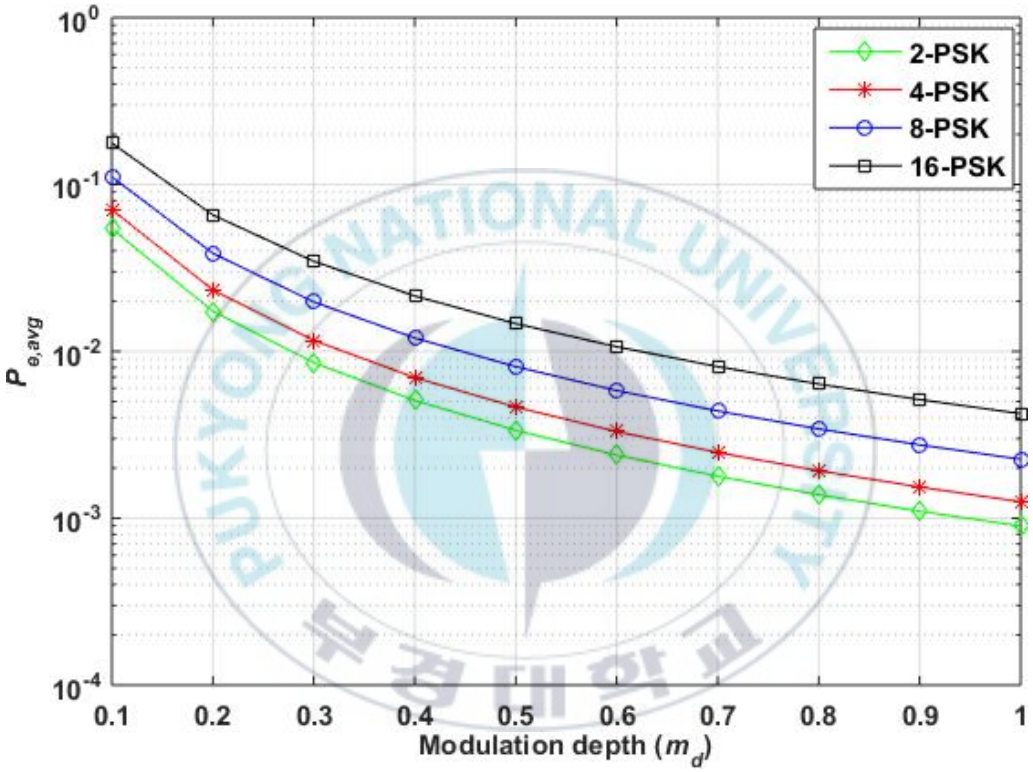


Figure 2.7 Average BER relative to the modulation depth for different constellation sizes.

Figure 2.8 depicts the outage probability as a function of the received SNR for different baseline distances. It is interesting to note that the outage performance is *not linearly* related to the baseline distance $d$. For instance, at an SNR of 26 dB, the outage probability $P_{out}$ is equal to $10^{-4}$ for $d = 2000$ m and reduced by approximately 10 times to $10^{-5}$ at $d = 1500$ m. However, at $d = 1000$ m, $P_{out}$ reduces significantly by 1000 times to that obtained at $d = 1500$ m.

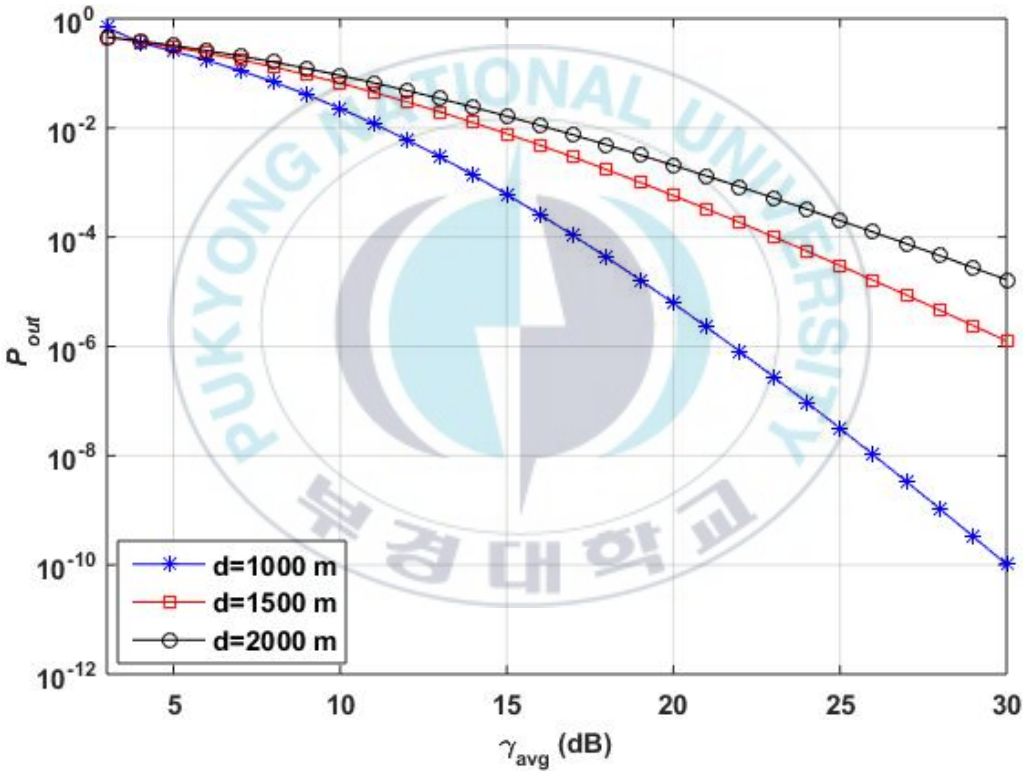


Figure 2.8 Outage probability relative to the modulation depth for different constellation sizes.

The impact of correlation on the performance of the proposed system is illustrated in Figure 2.9. The outage threshold is set to 4 dB, whereas the switching threshold is set to 5 dB. The baseline distance $d$ is set to 2000 m. As expected, the correlated links are found to deteriorate the performance.

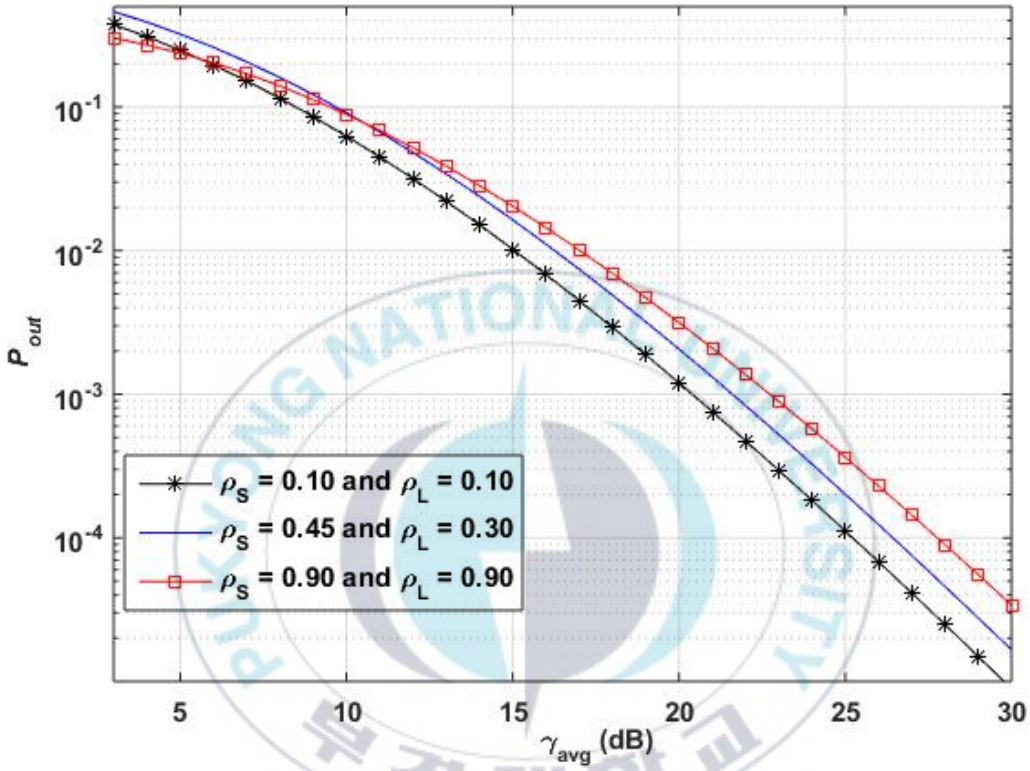


Figure 2.9 Impact of correlation on the outage performance at different SNR values.

## 2.4 Maximal Selection Transmit Diversity

Motivated by the fact that an optical channel is slow time-varying, we investigate the maximal selection transmit diversity for NLOS optical scattering

communications. We characterize the received UV signal by a continuous waveform detector. Given the fact that the turbulence-induced fading is a slow time-varying process, it is safe to assume that the channel information can readily be made available at the transmitter. Following this, we quantify the CDF of the largest order statistics of the received signal, based on the single-scattering assumption. Subsequently, we derive the closed-form mathematical tractable expressions for the average BER, outage probability, and channel capacity.

### 2.4.1 System Model

The proposed system model is illustrated in Figure 2.10. The communication is established via multiple-input single-input (MISO) with $L$ number of diverse branches. We consider non-return-to-zero intensity-modulation with direct detection (IM/DD) OOK transmission scheme. The information data is represented by $b \in \{\alpha P_t,\ P_t\}$, where $P_t$ represents the transmit optical power and $\alpha, 0 \leq \alpha < 1$, denotes the optical source extinction ratio.

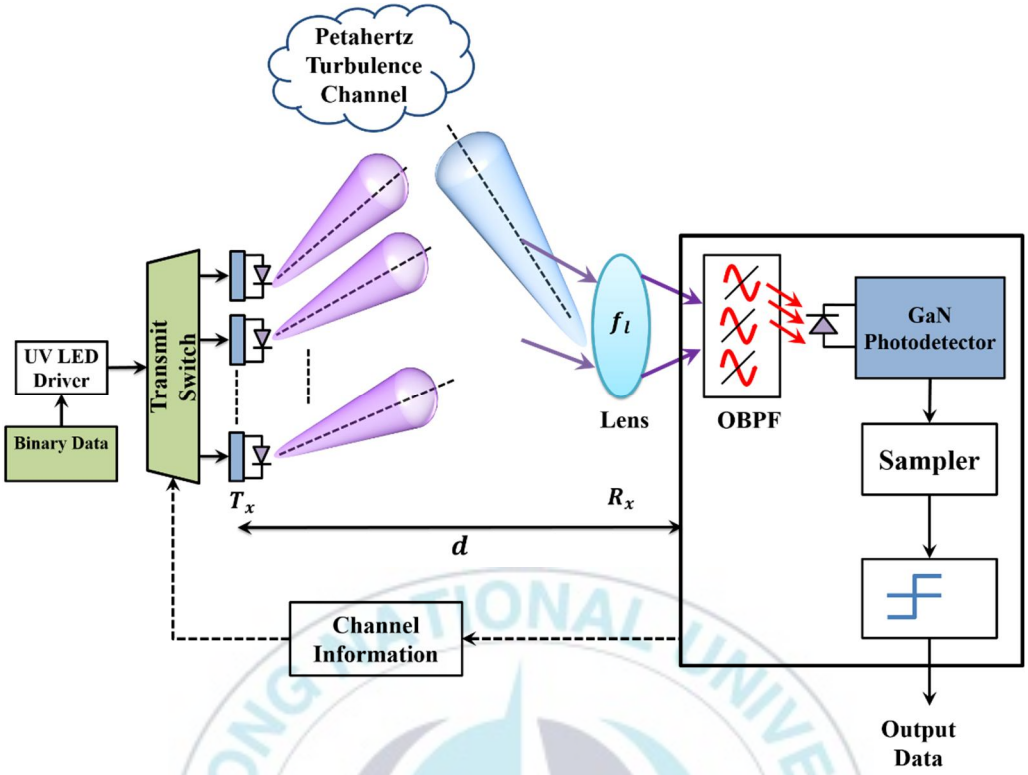


Table 2.10 Maximal selection transmit diversity for NLOS optical scattering communications.

The instantaneous signal received over the turbulence channel can be expressed as

$$y(t) = SHP_t(t)I + n(t), \tag{2.15}$$

where the responsivity of the detector is denoted by $S$ (A/W). $n(t)$ is the AWGN with zero mean and variance $N_0$. $H = H_T \times H_{PL} \times H_G$ represents the

channel state. $H_T$ denotes the attenuation due to the atmospheric turbulence and is given by [24]

$$H_T = 10^{\frac{\sqrt{23.17 C_n^2 k^{7/6}}\left(\sqrt{d_{tv}^{11/6}+d_{vr}^{11/6}}\right)}{5}}. \tag{2.16}$$

$C_n^2$ in Equation (2.16) represents the refractive index structure parameter and determines the strength of the turbulence. Its typical values lie in the range from $10^{-13}$ to $10^{-15}$ $\mathrm{m}^{-2/3}$ [25]. $k$ is the wave number. $H_{PL}$ represents the path loss due to the atmospheric scattering and attenuation, and can be obtained as [26]

$$H_{PL} = \frac{A_r \alpha_s q_s \phi_r \phi_t^2 \sin\theta_s \left(12\sin^2\psi_r + \phi_r \sin^2\psi_t\right)}{96 d \sin^2\psi_r \sin\psi_t \left(1-\cos\frac{\phi_t}{2}\right)\exp\left[\frac{\alpha_t d\left(\sin\psi_r + \sin\psi_t\right)}{\sin\theta_s}\right]}, \tag{2.17}$$

where all the parameters in Equation (2.17) are defined in Chapter 1 (Figure 1.1). $H_G$ is the loss due to the geometric spreading. It can be expressed as [27]

$$H_G = \int_{A_r} U_{beam}\left(\rho - r_{bc}; d_{vr} \middle| d_{tv}\right), \tag{2.18}$$

where $U_{beam}$ represents the conditional normalized spatial distribution at any distance $d_{vr}$ of the beam scattered in the common volume. $\rho$ in Equation (2.19)

represents a radial vector measured from the beam center and $r_{bc}$ is the beam center.

### 2.4.2 Marginal Distribution of Received UV signal

To describe the geometric spreading, we consider a Gaussian beam profile. The impact of atmospheric turbulence on the propagation of the Gaussian beam can be best analyzed using the Gamma-Gamma distribution. The PDF of the atmospheric scintillation observed from the transmitter to the common volume can be expressed as

$$f_{I_v}\left(I_v\right)=\frac{2\left(\alpha_v\beta_v\right)^{\frac{\alpha_v+\beta_v}{2}}}{\Gamma\left(\alpha_v\right)\Gamma\left(\beta_v\right)}I_v^{\frac{\alpha_v+\beta_v}{2}-1}K_{\alpha_v-\beta_v}\left(2\sqrt{\alpha_v\beta_vI_v}\right), \tag{2.20}$$

where $\alpha_v$ and $\beta_v$ are the model parameters and denote the effective number of small- and large-scale eddies in the turbulence channel. Assuming a single-scattering event, the conditional PDF of the received signal is given by

$$f_{I_r}\left(I_r\left|I_v\right.\right)=\frac{2\left(\alpha_r\beta_r\right)^{\frac{\alpha_r+\beta_r}{2}}}{\Gamma\left(\alpha_r\right)\Gamma\left(\beta_r\right)}I_r^{\frac{\alpha_r+\beta_r}{2}-1}K_{\alpha_r-\beta_r}\left(2\sqrt{\alpha_r\beta_rI_r}\right). \tag{2.21}$$

Utilizing Equations (2.20) and (2.21), the marginal PDF of the received irradiance is derived as

$$f_{I_r}\left(I_r\right)=\int_0^{\infty} f_{I_r}\left(I_r\left|I_v\right.\right) f_{I_v}\left(I_v\right) dI_v, I_v>0$$

$$=\frac{\left(\alpha_v\beta_v\right)\left(\alpha_r\beta_r\right)^{\frac{\alpha_r+\beta_r}{2}}}{\Gamma\left(\alpha_v\right)\Gamma\left(\beta_v\right)\Gamma\left(\alpha_r\right)\Gamma\left(\beta_r\right)} I_r^{\frac{\alpha_r+\beta_r}{2}-1} \quad . \qquad (2.22)$$

$$\times G_{0,2}^{2,0}\left[\alpha_r\beta_r I_r\left|\begin{matrix}-\\ \frac{\alpha_r-\beta_r}{2}, -\frac{\alpha_r-\beta_r}{2}\end{matrix}\right.\right]$$

***Remark 2.1:*** *Kindly note that the received scattered UV signal is impaired by the multiplicative effect of the turbulence-induced fading* $I_r$*. We normalize the random variable* $I_r$ *with statistical average* $E[I_r]=1$*. In addition, it is to be noted that atmospheric scintillation denoted by* $I_r$ *is a slow time-varying process* [28].

### 2.4.3 CDF of Largest Order Statistics

We assume that the random variables representing the channel irradiance are independent and identically distributed. Following this, the CDF of the largest order statistics $I_{r,\max}$ is given by

$$F_{I_{r,\max}}\left(I_{r,\max}\right)=P_r\left[I_{r,\max}\le I_r\right]$$

$$=P_r\left[\begin{matrix}I_{r,l}\\ \forall l=\{1,\cdots,L\}\end{matrix}\le I_r\right]=\left[F_{I_r}\left(I_r\right)\right]^L, \qquad (2.23)$$

where $L$ is the number of transmitting lasers employed and $F_{I_r}(I_r)$ is the CDF of the $I_r$, and is derived as

$$F_{I_r}\left(I_r\right)=\frac{\left(\alpha_v\beta_v\right)\left(\alpha_r\beta_r\right)^{\frac{\alpha_r+\beta_r}{2}}}{\Gamma\left(\alpha_v\right)\Gamma\left(\beta_v\right)\Gamma\left(\alpha_r\right)\Gamma\left(\beta_r\right)}I_r^{\frac{\alpha_r+\beta_r}{2}}$$
$$\times G_{1,3}^{2,1}\left[\alpha_r\beta_r I_r\left|\begin{matrix}\frac{2-\alpha_r-\beta_r}{2}\\ \frac{\alpha_r-\beta_r}{2},-\frac{\alpha_r-\beta_r}{2},-\frac{\alpha_r+\beta_r}{2}\end{matrix}\right.\right]. \quad (2.24)$$

Utilizing Equations (2.23) and (2.24), the PDF of the largest order statistics is derived as

$$f_{I_{r,\max}}\left(I_{r,\max}\right)=L\left[F_{I_r}\left(I_r\right)\right]^{L-1}f_{I_r}\left(I_r\right)$$
$$=\frac{2\left(\alpha_v\beta_v\right)^2\left(\alpha_r\beta_r\right)^{\alpha_r+\beta_r}}{\left[\Gamma\left(\alpha_v\right)\Gamma\left(\beta_v\right)\Gamma\left(\alpha_r\right)\Gamma\left(\beta_r\right)\right]^2}I_{r,\max}^{\alpha_r+\beta_r-1}$$
$$\times G_{0,2}^{2,0}\left[\alpha_r\beta_r I_{r,\max}\left|\begin{matrix}-\\ \frac{\alpha_r-\beta_r}{2},-\frac{\alpha_r-\beta_r}{2}\end{matrix}\right.\right] \quad . (2.25)$$
$$\times G_{1,3}^{2,1}\left[\alpha_r\beta_r I_{r,\max}\left|\begin{matrix}\frac{2-\alpha_r-\beta_r}{2}\\ \frac{\alpha_r-\beta_r}{2},-\frac{\alpha_r-\beta_r}{2},-\frac{\alpha_r+\beta_r}{2}\end{matrix}\right.\right]$$

### 2.4.4 Average BER

$$P_{e,avg} = \int_0^{\infty} P_e\left(\gamma \middle| I_{r,\max}\right) f_{I_{r,\max}}\left(I_{r,\max}\right) dI_{r,\max}$$

$$-\frac{\left(\alpha_v\beta_v\right)^2\left(\alpha_r\beta_r\right)^{\left(\frac{3\alpha_r+\beta_r}{2}\right)}}{4\pi\left[\Gamma\left(\alpha_v\right)\Gamma\left(\beta_v\right)\Gamma\left(\alpha_r\right)\Gamma\left(\beta_r\right)\right]^2}\int_0^{\infty} I_{r,\max}^{\left(\frac{3\alpha_r+\beta_r-2}{2}\right)} \exp\left(-2\sqrt{\alpha_r\beta_r I_{r,\max}}\right)$$

$$\times G_{2,6}^{4,2}\left[\frac{\left(\alpha_r\beta_r\right)^2 I_{r,\max}^2}{16}\middle| \begin{matrix} \frac{2-\alpha_r-\beta_r}{4}, \frac{4-\alpha_r-\beta_r}{4} \\ \frac{\alpha_r-\beta_r}{4}, \frac{\alpha_r-\beta_r+2}{4}, \frac{\beta_r-\alpha_r}{4}, \frac{\alpha_r-\beta_r+2}{4}, \frac{-\alpha_r-\beta_r}{4}, \frac{2-\alpha_r-\beta_r}{4} \end{matrix}\right]$$

$$\times G_{1,2}^{2,0}\left[\frac{\gamma_{avg} I_{r,\max}^2}{8}\middle| \begin{matrix} 1 \\ 0, \frac{1}{2} \end{matrix}\right] dI_{r,\max}$$

(2.26)

Solving the integration in Equation (2.26) using the identity given by Equation (1) in [29], we obtain

$$P_{e,avg} = \frac{2^{\frac{6\alpha_r+2\beta_r-7}{2}}\left(\alpha_v\beta_v\right)^2\left(\alpha_r\beta_r\right)^{-\beta_r}}{\pi^{5/2}\left[\Gamma\left(\alpha_v\right)\Gamma\left(\beta_v\right)\Gamma\left(\alpha_r\right)\Gamma\left(\beta_r\right)\right]^2}$$

$$\mathbf{S}\left[\begin{matrix}\begin{bmatrix}4,0\\0,0\end{bmatrix}\\\begin{pmatrix}2,4\\0,2\end{pmatrix}\\\begin{pmatrix}0,2\\1,0\end{pmatrix}\end{matrix}\right| \begin{matrix}\frac{3\alpha_r+\beta_r}{4},\frac{3\alpha_r+\beta_r+1}{4},\frac{3\alpha_r+\beta_r+2}{4},\frac{3\alpha_r+\beta_r+3}{4};-\\ \frac{2-\alpha_r-\beta_r}{4},\frac{4-\alpha_r-\beta_r}{4},\frac{\alpha_r-\beta_r}{4},\frac{\alpha_r-\beta_r+2}{4},\frac{-\alpha_r+\beta_r}{4},\frac{-\alpha_r+\beta_r+2}{4},\frac{-\alpha_r-\beta_r}{4},\frac{2-\alpha_r-\beta_r}{4}\\ 1;0,2\end{matrix}\left|\begin{matrix}1\\\frac{2\gamma_{avg}}{\left(\alpha_r\beta_r\right)^2}\end{matrix}\right.\right] \tag{2.27}$$

where **S**[·] in Equation (2.27) represents the extended generalized bivariate function.

### 2.4.5 Outage Probability

Mathematically, the outage probability can be written as

$$P_{out}\left(\gamma_{Th}\right) = P_r\left[\gamma < \gamma_{Th}\right] = \int_0^{\gamma_{Th}} f_\gamma\left(\gamma\right)d\gamma\,, \tag{2.28}$$

where $\gamma_{Th}$ is the outage threshold and $f_\gamma(\gamma)$ is the PDF of the received instantaneous SNR. Solving for Equation (2.28), we obtain

$$P_{out}(\chi_{Th}) = \frac{\left[(\alpha_v\beta_v)(\alpha_r\beta_r)^{\left(\frac{\alpha_r+\beta_r}{2}\right)}\right]^2}{\left[\Gamma(\alpha_v)\Gamma(\beta_v)\Gamma(\alpha_r)\Gamma(\beta_r)\right]^2}\left(\frac{1}{\gamma_{avg}}\right)^{\left(\frac{\alpha_r+\beta_r}{2}\right)}$$
$$\times\sqrt{2\pi}\sum_{k=0}^{\infty}\left\{\frac{(-1)^k}{k!}\sum_{j=0}^{\left\lfloor|\alpha_r-\beta_r|-\frac{1}{2}\right\rfloor}\left[\frac{\left(j+|\alpha_r-\beta_r|-\frac{1}{2}\right)!}{j!\left(-j+|\alpha_r-\beta_r|-\frac{1}{2}\right)!}2^{k-2j-\frac{1}{2}}(\alpha_r\beta_r)^{\left(\frac{2k-2j-1}{4}\right)}\left(\frac{1}{\gamma_{avg}}\right)^{\left(\frac{2k-2j-1}{8}\right)}\right.\right.$$
$$\left.\left.\times\int_0^{\gamma_{Th}}\gamma^{\left(\frac{4\alpha_r+4\beta_r+2k-2j-1}{8}-1\right)}G_{1,3}^{2,1}\left[\alpha_r\beta_r\sqrt{\frac{\gamma}{\gamma_{avg}}}\middle|\begin{matrix}\frac{2-\alpha_r-\beta_r}{2}\\ \frac{\alpha_r-\beta_r}{2},-\frac{\alpha_r-\beta_r}{2},-\frac{\alpha_r+\beta_r}{2}\end{matrix}\right]d\gamma\right]\right\}$$

(2.29)

The integral in Equation (2.29) can be obtained in closed-form using the identity Equation (07.34.21.0084.01) in [30], as shown in Equation (2.30).

$$P_{out}(\chi_{Th}) = \frac{\left[(\alpha_v\beta_v)(\alpha_r\beta_r)^{\left(\frac{\alpha_r+\beta_r}{2}\right)}\right]^2}{\sqrt{8\pi}\left[\Gamma(\alpha_v)\Gamma(\beta_v)\Gamma(\alpha_r)\Gamma(\beta_r)\right]^2}\left(\frac{1}{\gamma_{avg}}\right)^{\left(\frac{\alpha_r+\beta_r}{2}\right)}$$
$$\times\sqrt{2\pi}\sum_{k=0}^{\infty}\left\{\frac{(-1)^k}{k!}\sum_{j=0}^{\left\lfloor|\alpha_r-\beta_r|-\frac{1}{2}\right\rfloor}\left[\frac{\left(j+|\alpha_r-\beta_r|-\frac{1}{2}\right)!}{j!\left(-j+|\alpha_r-\beta_r|-\frac{1}{2}\right)!}2^{k-2j-\frac{1}{2}}(\alpha_r\beta_r)^{\left(\frac{2k-2j-1}{4}\right)}\left(\frac{1}{\gamma_{avg}}\right)^{\left(\frac{2k-2j-1}{8}\right)}\right.\right.$$
$$\left.\left.\times\gamma_{Th}^{\left(\frac{4\alpha_r+4\beta_r+2k-2j-1}{8}\right)}\right.\right.$$
$$\left.\left.\times G_{3,7}^{4,3}\left[\left(\frac{2\alpha_r\beta_r}{\sqrt{\gamma_{avg}}}\right)^2\gamma_{Th}^4\middle|\begin{matrix}\frac{9-4\alpha_r-4\beta_r-2k+2j}{8},\frac{2-\alpha_r-\beta_r}{4},\frac{4-\alpha_r-\beta_r}{4}\\ \frac{\alpha_r-\beta_r}{4},\frac{\alpha_r-\beta_r+2}{4},\frac{\beta_r-\alpha_r}{4},\frac{\beta_r-\alpha_r+2}{4},-\frac{\alpha_r+\beta_r}{4},-\frac{\alpha_r+\beta_r-2}{4},\frac{1-4\alpha_r-4\beta_r-2k+2j}{8}\end{matrix}\right]\right]\right\}$$

(2.31)

### 2.4.6 Channel capacity

We assume perfect channel information with no power adaptation at the transmitter. The average capacity of the system under consideration is given by

$$C_{avg} = \int_0^{\infty} \log_2\left(1+\gamma_{avg} I_{r,\max}^2\right) f_{I_{r,\max}}\left(I_{r,\max}\right) dI_{r,\max} . \quad (2.32)$$

Solving Equation (23), the closed-form expression can readily be obtained as

$$C_{avg} = \frac{\ln(4)\left[\left(\alpha_v\beta_v\right)\left(\alpha_r\beta_r\right)^{\left(\frac{\alpha_r+\beta_r}{2}\right)}\right]^2}{\left[\Gamma\left(\alpha_v\right)\Gamma\left(\beta_v\right)\Gamma\left(\alpha_r\right)\Gamma\left(\beta_r\right)\right]^2}$$
$$\times\sum_{k=0}^{\infty}\left\{\frac{\left(-1\right)^k \gamma_{avg}^{k+1}}{k!\Gamma\left(k+2\right)}\left(\alpha_r\beta_r\right)^{-\left(\alpha_r+\beta_r+2k\right)}\right.$$
$$\left.\times G_{3,3}^{2,3}\left[1\left|\begin{matrix}\frac{2-\alpha_r-\beta_r}{2}, \frac{2-4k-3\alpha_r-\beta_r}{2}, \frac{2-4k-\alpha_r-3\beta_r}{2} \\ \frac{\alpha_r-\beta_r}{2}, -\frac{\alpha_r-\beta_r}{2}, -\frac{\alpha_r+\beta_r}{2}\end{matrix}\right.\right]\right\}$$

(2.33)

### 2.4.7 Results and Discussions

The simulation parameters are illustrated in Table 2.3.

Table 2.3 Simulation Parameters.

| Parameter | Value |
|---|---|
| UV frequency | 1.07 Petahertz |
| Modulation bandwidth | 20 MHz |
| Rayleigh scattering coefficient [31] | $0.49\ \mathrm{km}^{-1}$ |
| Extinction coefficient | $0.74\ \mathrm{km}^{-1}$ |
| Scattering phase function $q_s$ | 1 |
| $\{\phi_t, \phi_r, \psi_t, \psi_r\}$ | $\left\{\frac{\pi}{180}, \frac{\pi}{3}, \frac{\pi}{4}, \frac{\pi}{4}\right\}$ |
| Outage threshold $\gamma_{Th}$ | 5 dB |
| Active detector area [32] | $6.25\ \mathrm{mm}^2$ |
| Quantum efficiency | 0.29 A/W |

Figure 2.10 shows the distribution of the received irradiance over the NLOS link with a single scattering assumption for different turbulence strengths and baseline distances. As shown, a higher value of $C_n^2$ results in a Fresnel zone becoming larger than the coherence spatial radius, thereby increasing the channel impairment.

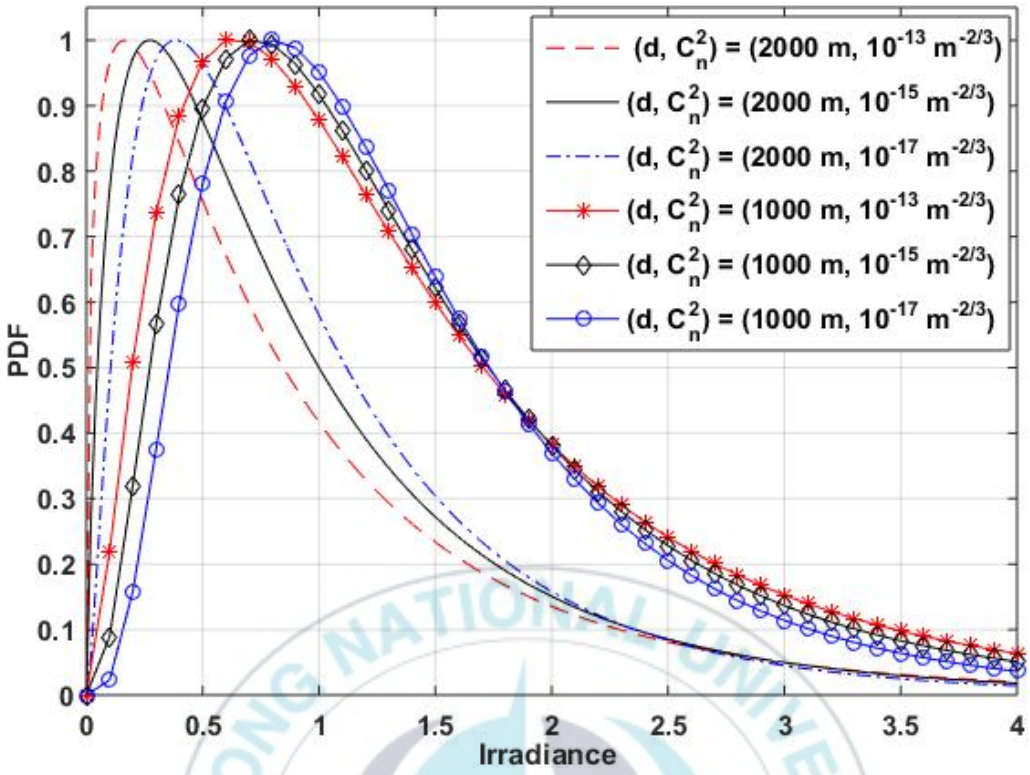


Figure 2.11 Distribution of the received irradiance over NLOS single scattered link.

Utilizing Equation (2.27), the average BER performance of the proposed system is illustrated in Figure 2.12. The curves are obtained for different turbulence strengths and diversity branches. The results demonstrate that the proposed system is useful in combating the turbulence-induced fading in applications where strict power constraint is imposed or it is impractical to increase the power budget. A similar analysis can be inferred for the outage analysis shown in Figure 2.13.

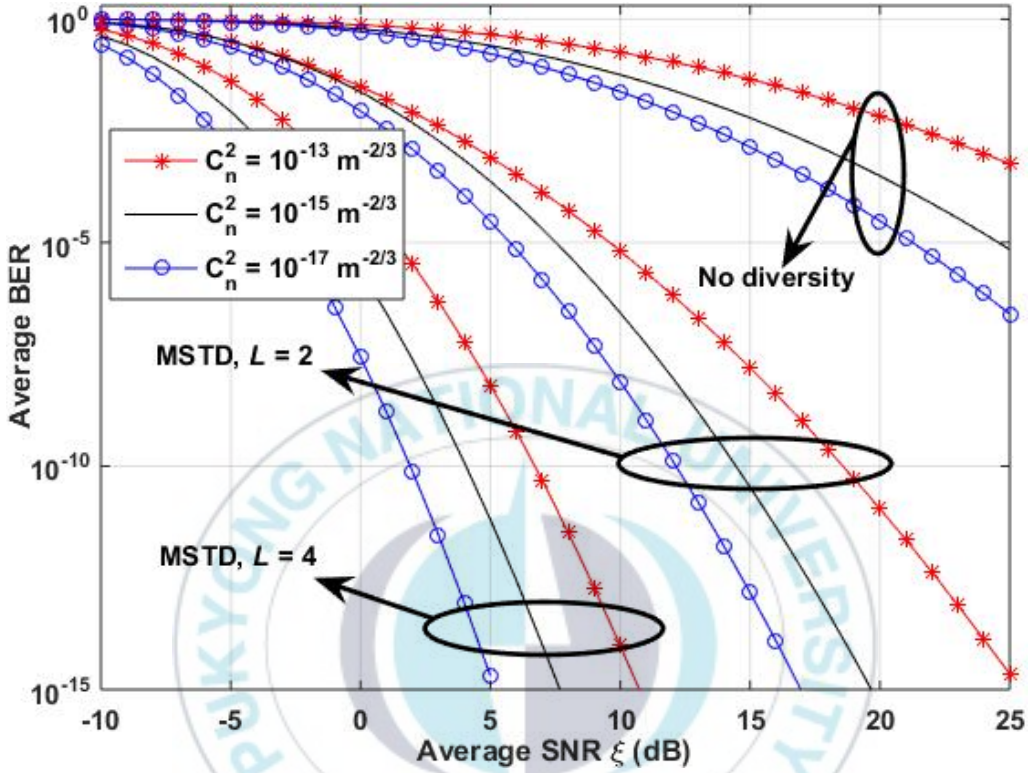


Figure 2.12 Average BER relative to the average received SNR for different turbulence strength and diversity branches.

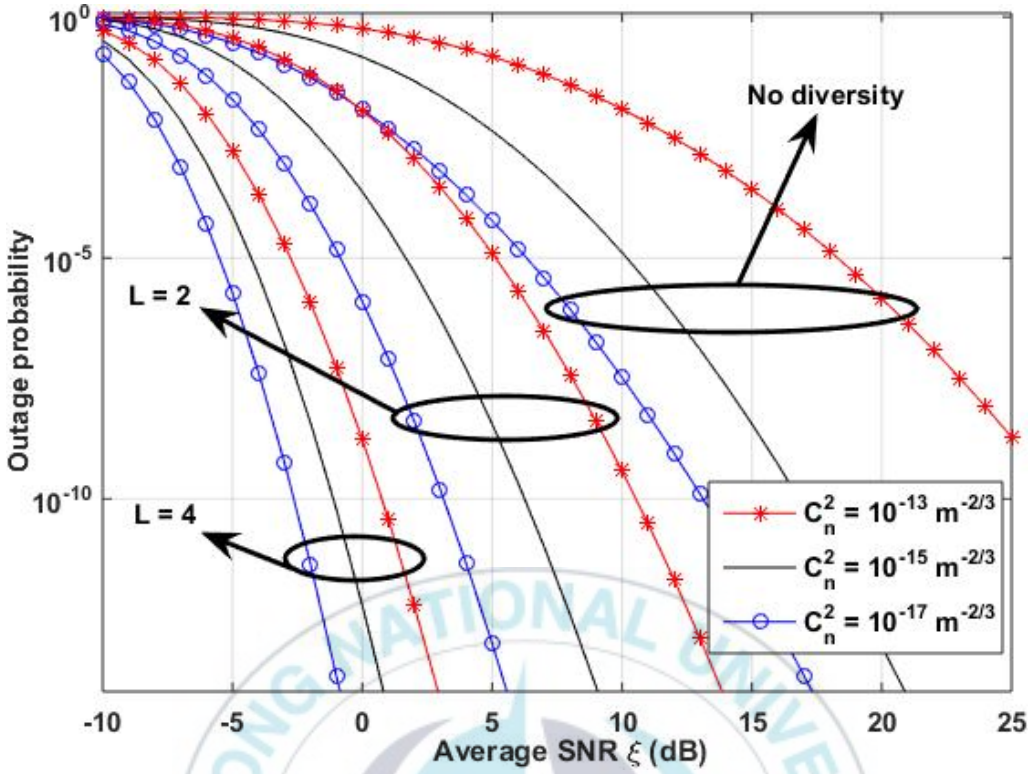


Figure 2.13 Outage probability relative to the average received SNR for different turbulence strength and diversity branches.

The achievable capacity per unit bandwidth for the underlying system is depicted in Figure 2.13. We assume that perfect channel state information is available on the transmitter side. It is to be noted that as the number of diversity branches increases, the degree of the turbulence strength becomes less relevant, as the curves corresponding to different turbulence strengths come closer.

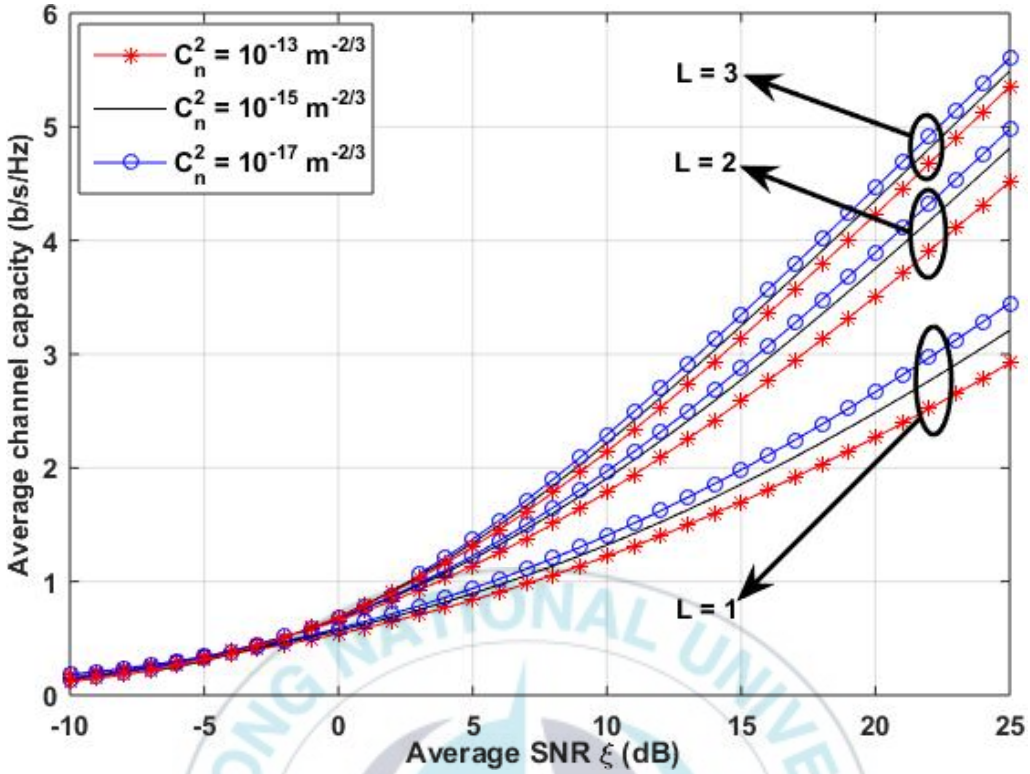


Figure 2.14 Achievable channel capacity relative to the average received SNR for different diversity branches.

To demonstrate the superiority of the MSTD scheme, we compare the performance with the repetition codes and orthogonal space-time block codes. It is shown that MSTD extracts full diversity and provides robust performance compared to repetition code and orthogonal space-time block codes. For example, at an average SNR of 20 dB and $C_n^2 = 5 \times 10^{-14}$ m$^{-\frac{2}{3}}$, the average error probability observed in the MSTD scheme with $L = 2$ is approximately

equal to $1 \times 10^{-11}$, whereas it is approximately $5 \times 10^{-6}$ for orthogonal space-time block codes and $1 \times 10^{-7}$ for the repetition codes.

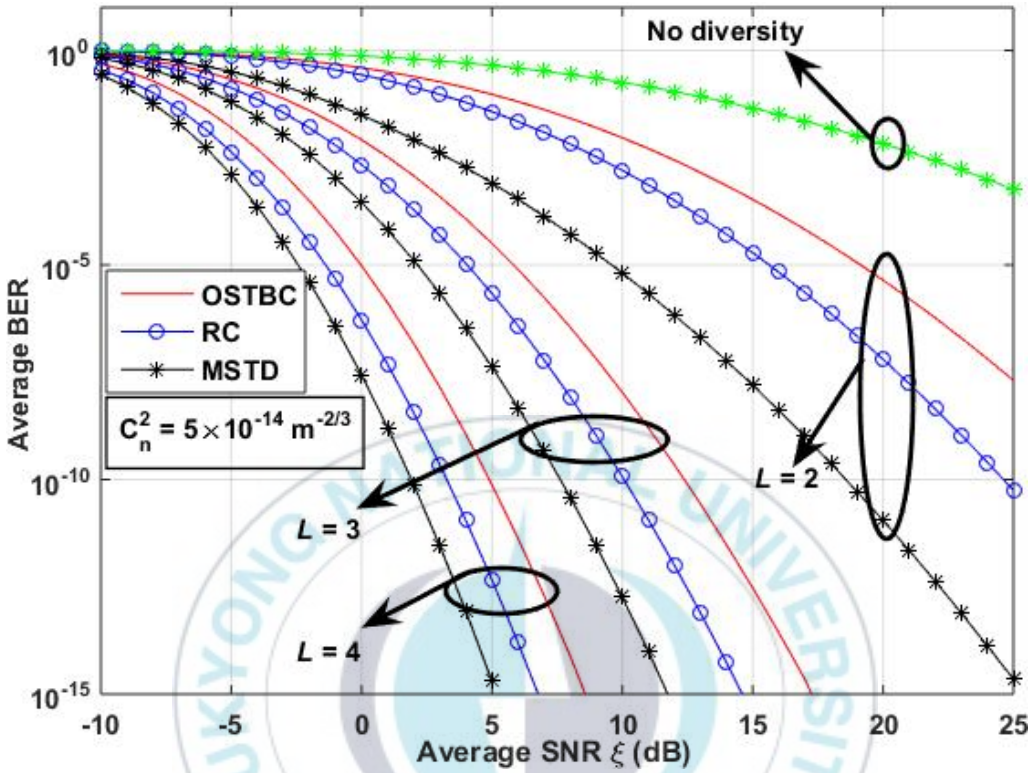


Figure 2.15 Performance comparison of the MSTD with the OSTBC and RC.

## 2.5 Amplify-and-Forward Multihop NLOS UV Communications

In this section, we investigate multihop NLOS optical scattering communications [17]. Each scattered path is assumed to follow the Gamma-Gamma distributed turbulence fading. We formulate a new problem and investigate the trade-off between the data rate and the number of relay nodes in the multihop NLOS optical scattering communications.

### 2.5.1 System Model

The system model is illustrated in Figure 2.15. We consider an M-PSK subcarrier intensity modulation. We assume an *N*-hop NLOS optical scattering communication system with the amplifying-and-forward transparent relaying protocol. $d$ is the total baseline distance between the transmitter and the receiver.

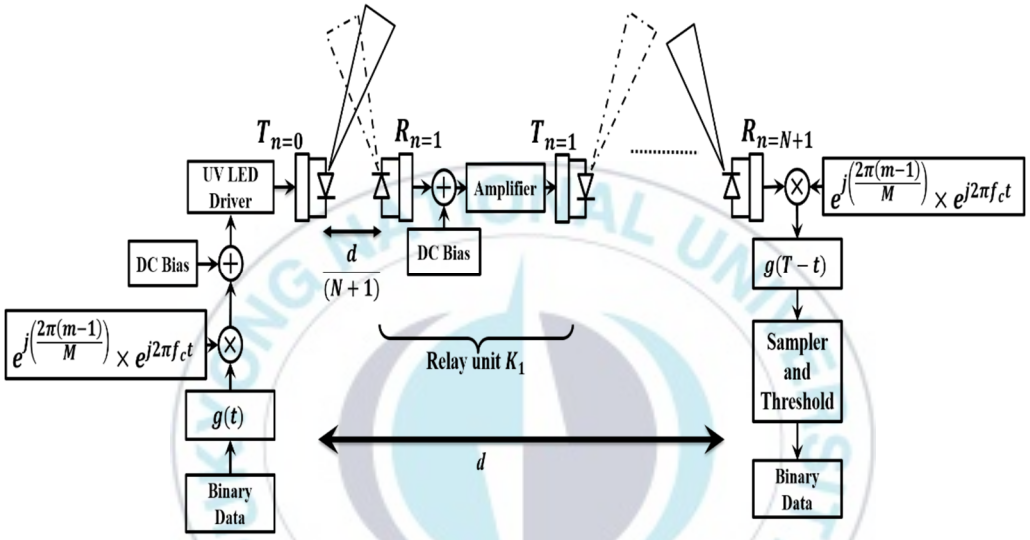


Figure 2.16 System model.

A harmonic signal of electric current modulation with phase $\frac{2\pi(m-1)}{M}$ and center carrier frequency $f_c$ is converted into a similar signal with optical power $P_t(t)$, given by [21]

$$P_t(t) = P\left\{1 + m_d g(t)\cos\left[2\pi f_c t - \frac{2\pi}{M}(m-1)\right]\right\}, \quad (2.34)$$

where $P$ is defined as

$$P = \frac{1}{T_s}\int_0^{T_s} P_t(t)\,dt = \frac{P_{Total}}{(N+1)}. \tag{2.35}$$

$P$ represents the average transmit optical power allocated to each relay. $T_s$ denotes the symbol duration and $P_{Total}$ represents the total power budget.

Following Equation (2.35), the instantaneous received signal at the receiver of the $n$th relay can be expressed as

$$y_n(t) = SI_nH_nP\left\{1 + m_d g(t)\cos\left[2\pi f_c t - \frac{2\pi}{M}(m-1)\right]\right\} + n_n(t) \tag{2.36}$$

where $S$ is the responsivity in A/W. $I_n$ represents the irradiance and is normalized to unity $E[I_n] = 1$, where $E[\cdot]$ is the expectation operation. $n_n(t)$ denotes the AWGN with zero mean and uniform power spectral density $N_0$. $H_n$ is the channel gain for the link $(n-1) \to n$ and is normalized with respect to the gain of the direct link, that is, $H_n = \frac{h_n}{h_{0,N+1}}$, where $h_{0,N+1}$ is the gain of the direct link from the transmitter to the receiver and $h_n = h_n^t \times h_n^s$, where $h_n^t$ denotes the attenuation due to the turbulence and $h_n^s$ represents the attenuation due to the atmospheric scattering.

We define the average received SNR as [33]

$$\gamma_{avg} = \frac{\left(SH_n Pm_d\right)^2}{N_0} E\left[I_n^2\right]. \tag{2.37}$$

The end-to-end received SNR is given by

$$\gamma_{eq} = \left[\prod_{n=1}^{N+1}\left(1+\frac{1}{\gamma_n}\right)-1\right]^{-1}, \tag{2.38}$$

where $\gamma_n$ is the instantaneous received SNR at the $n$th node.

### 2.5.2 Derivation of the PDF of the Instantaneous End-to-end Received SNR

The random variable $\gamma_{eq}$ is transformed into a new random variable $\mu_{eq}$ as

$$\mu_{eq} = \sum_{n=1}^{N+1} \mu_n, \tag{2.39}$$

where $\mu_{eq} = \log_e\left(1+\frac{1}{\gamma_{eq}}\right)$ and $\mu_n = \log_e\left(1+\frac{1}{\gamma_n}\right)$.

Under the assumption that all the relay nodes are subject to independent fading, the transformed random variable $\mu_n$ is also independent. It yields

$$\varphi_{\mu_{eq}}(w) = \prod_{n=1}^{N+1} \varphi_{\mu_n}(w), \tag{2.40}$$

where $\varphi_{\mu_n}$ is the Fourier transform of the PDF of $\mu_n$ as

$$\varphi_{\mu_n}(w) = \int_0^{\infty} f_{\mu_n}(\mu_n) \exp(jw\mu_n) d\mu_n , \tag{2.41}$$

To compute the characteristic function $\varphi_{\mu_n}(w)$, we need the PDF of the transformed random variable $\mu_n$. By applying the Jacobean transformation, the marginal PDF of the transformed random variable $\mu_n$ is obtained as

$$f_{\mu_n}(\mu_n) = \frac{(p_n q_n)^{\left(\frac{p_n+q_n}{2}\right)}}{2\Gamma(p_n)\Gamma(q_n)} \left(\frac{1}{\gamma_{avg}}\right)^{\left(\frac{p_n+q_n}{4}\right)} e^{\mu_n} \left(e^{\mu_n}-1\right)^{-\left(\frac{p_n+q_n+4}{4}\right)}$$
$$\times G_{0,2}^{2,0}\left[ p_n q_n \sqrt{\frac{1}{\left(e^{\mu_n}-1\right)\gamma_{avg}}} \middle| \begin{matrix} \frac{p_n-q_n}{2}, -\frac{p_n-q_n}{2} \end{matrix} \right] \tag{2.42}$$

The numerical calculation of the transformed characteristic function $\varphi_{\mu_n}(w)$ involves a single-fold integral with a rapidly decaying function $f_{\mu_n}(\mu_n)$ as $\mu_n$ $\rightarrow \infty$. The closed-form expression for the transformed characteristic function $\varphi_{\mu_n}(w)$ is obtained as follows. Applying the Maclaurin series in Equation (2.42) yields

$$\varphi_{\mu_n}(w)=\frac{(p_n q_n)^{\left(\frac{p_n+q_n}{2}\right)}}{2\Gamma(p_n)\Gamma(q_n)}\left(\frac{1}{\gamma_{avg}}\right)^{\left(\frac{p_n+q_n}{4}\right)}$$
$$\times\int_0^{\infty}\mu_n^{-\left(\frac{p_n+q_n+4}{4}\right)}G_{2,0}^{0,2}\left[\frac{\sqrt{\gamma_{avg}\mu_n}}{p_n q_n}\middle|\begin{matrix}1-\frac{p_n-q_n}{2};1+\frac{p_n-q_n}{2}\\ -\end{matrix}\right]\exp(jw\mu_n)d\mu_n \tag{2.43}$$

Utilizing the Fourier transformation, the closed-form expression for the transformed characteristic function $\varphi_{\mu_n}(w)$ can be expressed as

$$\varphi_{\mu_n}(w)=$$
$$\frac{2^{-\left(\frac{p_n+q_n-10}{4}\right)}(p_n q_n)^{\left(\frac{p_n+q_n}{2}\right)}}{\pi^3\Gamma(p_n)\Gamma(q_n)}\left(\frac{1}{\gamma_{avg}}\right)^{\left(\frac{p_n+q_n}{4}\right)}w^{\left(\frac{p_n+q_n}{4}\right)}G_{10,0}^{0,9}\left[\left(\frac{2^9\gamma_{avg}}{wp_n^2q_n^2}\right)^2\middle|\begin{matrix}a_{10}\\ -\end{matrix}\right] \tag{2.44}$$

Substituting (2.44) into (2.40), the closed-form expression for $\varphi_{\mu_{eq}}(w)$ can readily be obtained. Using inverse transformation, the PDF of $\varphi_{\mu_{eq}}(w)$ is given by

$$f_{\mu_{eq}}(\mu_{eq})=\frac{1}{2\pi}\int_0^{\infty}\varphi_{\mu_{eq}}(w)\exp(-jw\mu_{eq})dw. \tag{2.45}$$

The PDF of $\gamma_{eq}$ is obtained as

$$f_{\gamma_{eq}}(\gamma_{eq})=\frac{1}{\gamma_{eq}(1+\gamma_{eq})}f_{\mu_{eq}}(\mu_{eq})\Big|_{\mu_{eq}=\log_e\left(1+\frac{1}{\gamma_{eq}}\right)} \tag{2.46}$$

Solving Equation (2.46) leads to the closed-form expression for the end-to-end received SNR as shown in Equation (2.47). S[· | · | ·] in Equation (2.47) denotes the BMGF.

$$f_{\gamma_{eq}}\left(\gamma_{eq}\right)=\frac{1}{\gamma_{eq}\left(1+\gamma_{eq}\right)} \times\prod_{n=1}^{N+1}\left\{\frac{\left(\sqrt{2}\right)^{7}\left(p_n q_n\right)^{\left(\frac{p_n+q_n}{2}\right)}}{\left(\sqrt{\pi}\right)^{5}\Gamma\left(p_n\right)\Gamma\left(q_n\right)}\left(-\frac{1}{\gamma_{avg}}\right)^{\left(\frac{p_n+q_n}{4}\right)}\left(\log_e\left(1+\frac{1}{\gamma_{eq}}\right)\right)^{-\left(\frac{p_n+q_n+4}{4}\right)} \times S\left[\begin{bmatrix}-2 & 0\\ 0 & 0\end{bmatrix}\middle|\begin{matrix}-;-\\ 0;0\\ a_{10};-\end{matrix}\middle|\begin{matrix}0\\ \begin{pmatrix}1 & 1\\ 0 & 0\end{pmatrix}\\ \begin{pmatrix}9 & 0\\ 1 & 0\end{pmatrix}\end{matrix}\middle|\left(\frac{16\sqrt{\gamma_{avg}}}{p_n q_n}\right)^{4}\left(\log_e\left(1+\frac{1}{\gamma_{eq}}\right)\right)^{2}\right]\right\} \tag{2.47}$$

### 2.5.3 Algorithm to Obtain the Optimal Number of Relay Nodes

**Input:** Data rate R

**Initialization:** $E_{r,max}=0$ and $N_{optimal}=1$

1: **for** $N = 1$ to $N_{max}$ **do**

2: **for** $\rho = 0$ to 1 **do**

3: For a given $R, N$, and $\rho$, **compute** $E_r(R,N,\rho)$

4: **if** $\left(E_{r,max} < E_r(R,N,\rho)\right)$ **then**

5: $E_{r,max} = E_r(R,N,\rho)$

6: $N_{optimal} = N$

7: **end if**

8: **end for**

9: **end for**

10: **return** $N_{optimal}$

### 2.5.4 Results and Discussions

To validate the algorithm, we assume an isotropic scattering. The simulation parameters are illustrated in Table 2.4.

Table 2.4 Simulation Parameters.

| Parameter | Value |
|---|---|
| UV wavelength | 280 nm |
| Modulation bandwidth | 20 MHz |
| Attenuation coefficient [34] | 0.802 $\text{km}^{-1}$ |
| Visibility $v$ | 21 km |
| Scattering phase function $q_s$ | 1 |
| $\{\phi_t, \phi_r, \psi_t, \psi_r\}$ | $\left\{\frac{\pi}{180}, \frac{\pi}{3}, \frac{\pi}{6}, \frac{\pi}{4}\right\}$ |
| $C_n^2$ | $5 \times 10^{-14}$ $\text{m}^{-2/3}$ |
| Active detector area | 1.77 $\text{cm}^2$ |
| Depolarization ratio $\rho_u$ [19] | $3.501 \times 10^{-2}$ |

| | |
|---|---|
| Modulatin index | 0.5 |
| Baseline distance $d$ | 2 km |

For the given coding error exponent, we analyze the maximum optimal number of hops that a multihop NLOS UV communication system can support to achieve the desired data rate. As illustrated in Figure 2.16, an important observation can be inferred that when a higher data rate is required, a multihop system with small $N$ is preferable. We like to point out that, for a given data rate, there is an optimal number of relay nodes $N_{optimal}$ that achieves optimal performance in terms of random coding error exponent.

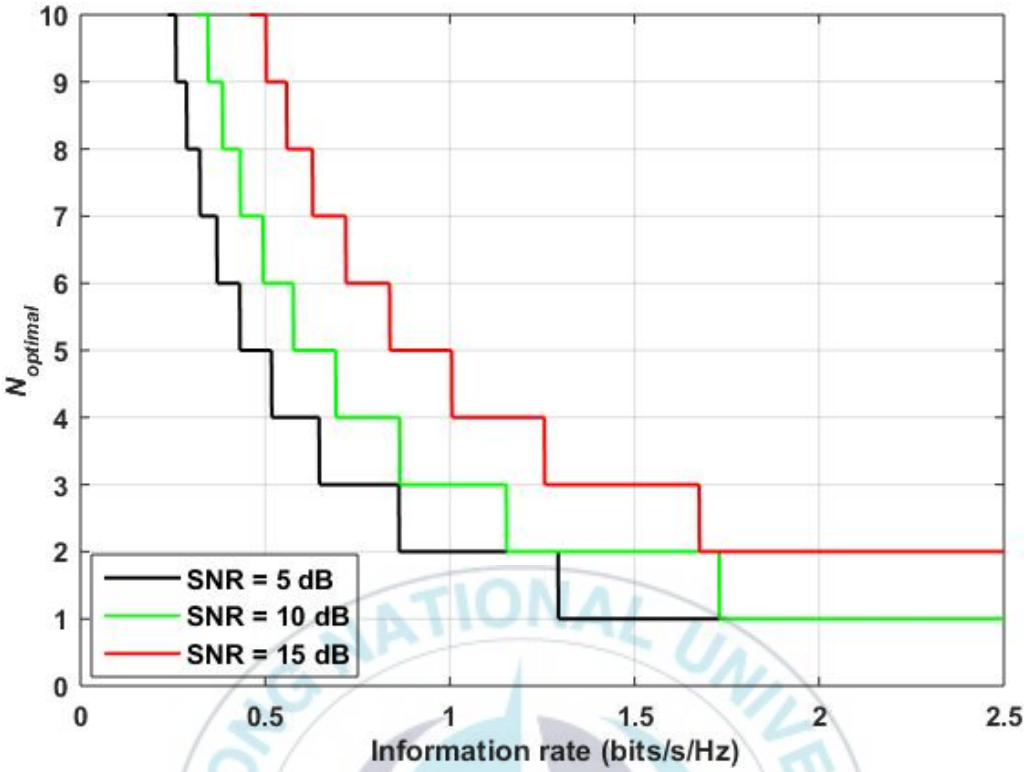


Figure 2.17 Optimal number of relay nodes as a function of the data rate.

# 3 Spectrum Sensing Techniques for Optical Scattering Communication Networks

In an NLOS optical scattering communication network, the user (detector) needs to periodically sense the available spectrum to avoid interference from other potential active transceivers. If the user detects the signal impinging on its FOV, it sends feedback to the transmit unit to acknowledge the establishment of the communication link. The optical spectrum sensing enables the user to periodically monitor the propagation channel and obtain access when it is available.

Recently, few optical spectrum sensing techniques for UV communications have been proposed. A technique based on the generalized likelihood ratio test (GLRT) was reported [35]. Compared to the sum-counting test, the GLRT based optical spectrum sensing technique was found to be optimal. However, it comes with the drawback of having higher computational complexity. A less complex spectrum sensing technique for optical scattering communication was proposed based on the sequential detection method [36]. To lower the computational complexity, a one-term approximation of the log-likelihood ratio test was obtained. In another work, however, for non-scattered LOS optical links, an optical spectrum sensing technique was presented [37]. It

utilized the statistics of the photoelectron count of p-i-n photodiode to sense the IM/DD optical signal over log-normal distributed atmospheric scintillations.

## 3.1 Optical Spectrum Sensing over FSO in Strong Turbulence Channel

We present a comprehensive analysis of energy detection-based optical spectrum sensing over a strong turbulence channel [38]. Our technique does not require any information of the optical signal to be detected and is shown to be robust against the unknown dispersive channel. Moreover, we quantify the performance improvement of the proposed energy detection-based spectrum sensing with a low-complex square-law selection diversity technique.

### 3.1.1 System Model

Figure 3.1 illustrates the energy detection-based optical spectrum sensing technique. The bandwidth of the filter is selected such that it matches the frequency spread of the incoming signal power envelope. The square-law selection diversity technique with $M$ branches employed. In the proposed technique, there is no necessity of optical channel tracking, as in the case with the pre-detection spatial diversity techniques such as equal gain combining and maximal ratio combining.

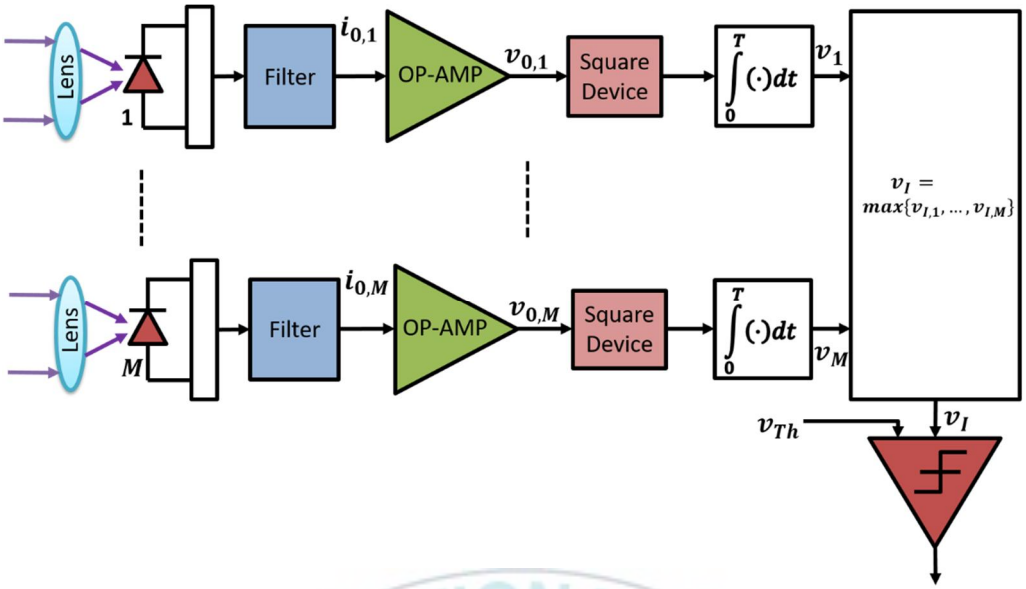


Figure 3.1 Energy detection-based optical spectrum sensing over strong turbulence channel.

We denote the presence and absence of the optical signal by hypotheses $H_1$ and $H_0$, respectively. Following this, the component of the electric current generated at the output of the filter of the $m$th branch can be expressed as

$$i_{o,m}(t) = \begin{cases} i_{s,m}(t) + i_{n,m}(t), & H_1 \\ = i_{n,m}(t), & H_0 \end{cases}, \tag{3.1}$$

where $m \in \{1, \cdots, M\}$. $i_{n,m}(t)$ is the output current due to the noise component and $i_{s,m}(t)$ represents the current due to the signal component and is modeled as $i_{s,l}(t) = SP_r(t)I_m$. $S$ is the detector responsivity in A/W and $I_m$ denotes the atmospheric scintillation at the $m$th branch. The noise is modeled as the shot

noise with zero mean and variance $\sigma_n^2 = E\left[i_{n,m}^2(t)\right]$. The average received SNR at any $m$th branch can then be defined as [39]

$$\gamma_{avg} = \frac{SP_r E\left[I_m\right]}{\sigma_n}, \quad m \in \left\{1, \cdots, M\right\}, \tag{3.2}$$

where $E[\cdot]$ denotes the expectation operation.

In optical communication where the propagation distance spans a few kilometers, the number of independent scattering becomes large and therefore, yields strong atmospheric scintillations [40]. Under such conditions, the fluctuations in the amplitude are generally believed and experimentally verified to follow the Rayleigh distribution [41]. With amplitude fluctuations following the Rayleigh distribution, the intensity fluctuations obey the negative exponential distribution. Therefore, the PDF of $I_m, \forall\, m \in \{1, \cdots, M\}$, can be written as

$$f_{I_m}\left(I_m\right) = \frac{1}{E\left[I_m\right]} \exp\left(-\frac{I_m}{E\left[I_m\right]}\right), \quad E\left[I_m\right] > 0 \tag{3.3}$$

### 3.1.2 Probability of False Alarm

The probability of a false alarm is defined as the probability of the detector deciding that the optical band is occupied by another user when the band

is actually unoccupied. The lesser $P_f$ is, the more likely the optical channel can be reused when it is unoccupied. Mathematically, we define $P_f$ as

$$\begin{aligned} P_f &= P_r\left(v_I > v_{Th} \middle| H_0\right) \\ &= 1 - F_{v_I,SLS}\left(v_I \middle| H_0\right) \end{aligned}, \tag{3.4}$$

where $v_I = \frac{1}{N}\sum_{n=1}^{N}\left|v_{0,m}(n)\right|^2$ is the test statistics for signal detection and $i_{0,m} \triangleq v_{0,m}$. $F_{v_I,SLS}(v_{Th})$ is the CDF of $v_I$ for square-law selection diversity technique. The closed-form expression of $P_f$ is derived as

$$P_f = 1 - \left[1 - \exp\left(-\frac{v_{Th}}{2\sigma_n^2}\right)\sum_{j=0}^{\frac{N}{2}-1}\frac{1}{j!}\left(\frac{v_{Th}}{2\sigma_n^2}\right)^j\right]^M. \tag{3.5}$$

### 3.1.3 Probability of Detection

It is defined as the probability of a detector, deciding that the optical spectrum is not free (occupied by another transceiver pair) when the optical spectrum is indeed not free. Mathematically, we define $P_d$ as

$$\begin{aligned} P_d &= P_r\left(v_I > v_{Th} \middle| H_1\right) \\ &= 1 - F_{v_I,SLS}\left(v_I \middle| H_1\right) \end{aligned}. \tag{3.6}$$

We derive the closed-form expression of $P_d$ as

$$
\begin{aligned}
P_d = 1 - & \left( \frac{1}{\gamma_{avg}} \right)^M \left( \sqrt{\frac{2\pi\sigma_n^2}{a}} \right)^M \\
& \times \prod_{j=1}^{M} \left\{ \exp\left( \frac{2\sigma_n^2}{a\gamma_{avg}^2} + \frac{3v_{Th}}{2\sigma_n^2} - \frac{4\sqrt{v_{Th}}}{\gamma_{avg}\sqrt{a}} \right) \right. \\
& \left. \times \left[ 1 - erf\left( \sqrt{\frac{2\sigma_n^2}{a\gamma_{avg}^2}} - \frac{\sqrt{2v_{Th}}}{\sigma_n^2} \right) \right] \right\} \\
& + \left( \frac{\pi}{\gamma_{avg}} \sqrt{\frac{v_{Th}}{a}} \exp\left( -\frac{v_{Th}}{2\sigma_n^2} \right) \right)^M \\
& \times \prod_{j=1}^{M} \left\{ \sum_{j=0}^{\frac{N}{2}-1} \frac{1}{j!} \left( \frac{\sqrt{v_{Th}a}}{\sigma_n^2} \right)^j \frac{\gamma_{avg}^j}{\sqrt{4\pi}} \right. \\
& \left. \times G_{3,3}^{1,2} \left[ \frac{4av_{Th}\gamma_{avg}^2}{\sigma_n^4} \middle| \begin{matrix} \frac{1}{2}, \frac{1-j}{2}, \frac{2-j}{2} \\ 0, -j, \frac{1}{2} \end{matrix} \right] \right\}
\end{aligned}
\tag{3.7}
$$

### 3.1.4 Results and Discussions

The optical spectrum sensing performance of the proposed system is quantified by illustrating the receiver operating characteristic (ROC) curves

$(P_d$ versus $P_f)$. $a$ is equal to 2. $\sigma_n^2 = 1$ and $N$ is equal to 500. Unless otherwise stated, $M$ is equal to 2.

The ROC curves obtained utilizing the proposed energy detection-based optical spectrum technique are illustrated in Figure 3.2. The curves are plotted for different SNR values over negative exponentially distributed turbulence-induced fading.

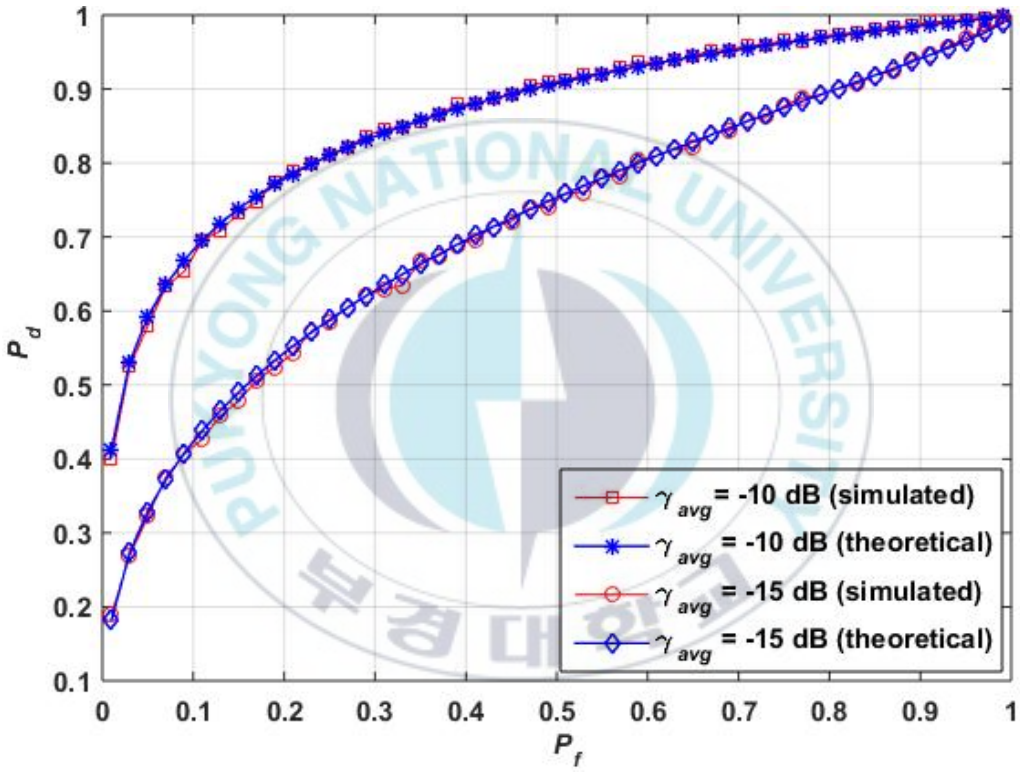


Figure 3.2 $P_d$ versus $P_f$ curves for different SNR values.

The impact of the square-law selection diversity technique on the performance of the energy detection-based optical spectrum sensing is illustrated

in Figure 3.3. As can be readily seen, the sensing capability of the proposed energy detection-based spectrum sensing technique can be boosted significantly by utilizing the square-law selection diversity technique.

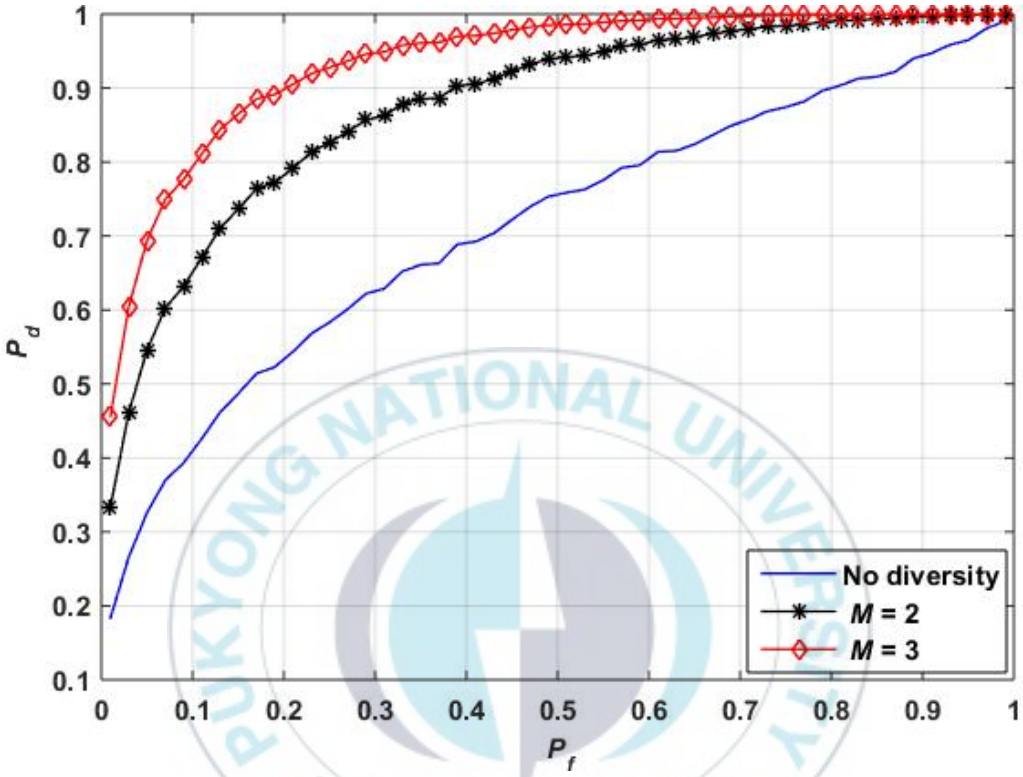


Figure 3.3 $P_d$ versus $P_f$ curves for different diversity orders over negative exponentially distributed turbulence channel.

The probability of false alarm against the number of samples is depicted in Figure 3.4. The curves are obtained with the target probability of detection is set to 0.9. As can be seen, for the given SNR and $P_d$, $P_f$ can be significantly reduced by increasing the number of samples.

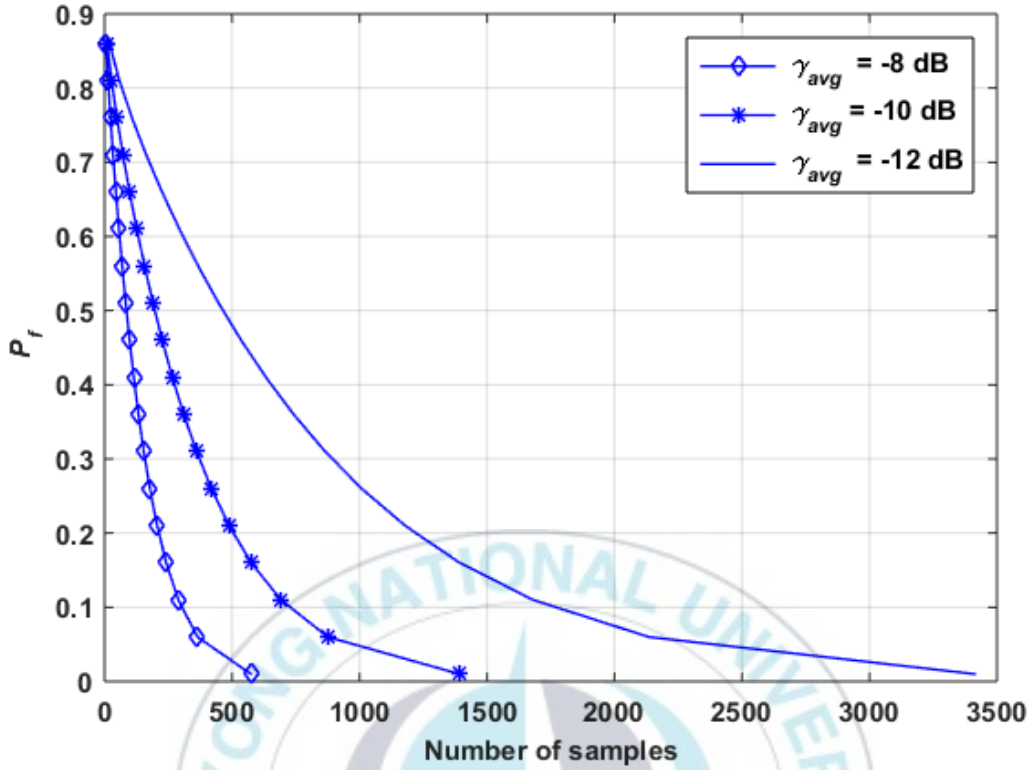


Figure 3.4 Probability of false alarm relative to the number of samples.

The importance of selecting an optimal value of detection threshold $v_{Th}$ on minimizing the probability of false alarm is shown in Figure 3.5. From the curves obtained, an important observation can be made that the detection threshold must be set slightly larger than $\sigma_n^2$ for the minimum probability of false alarm.

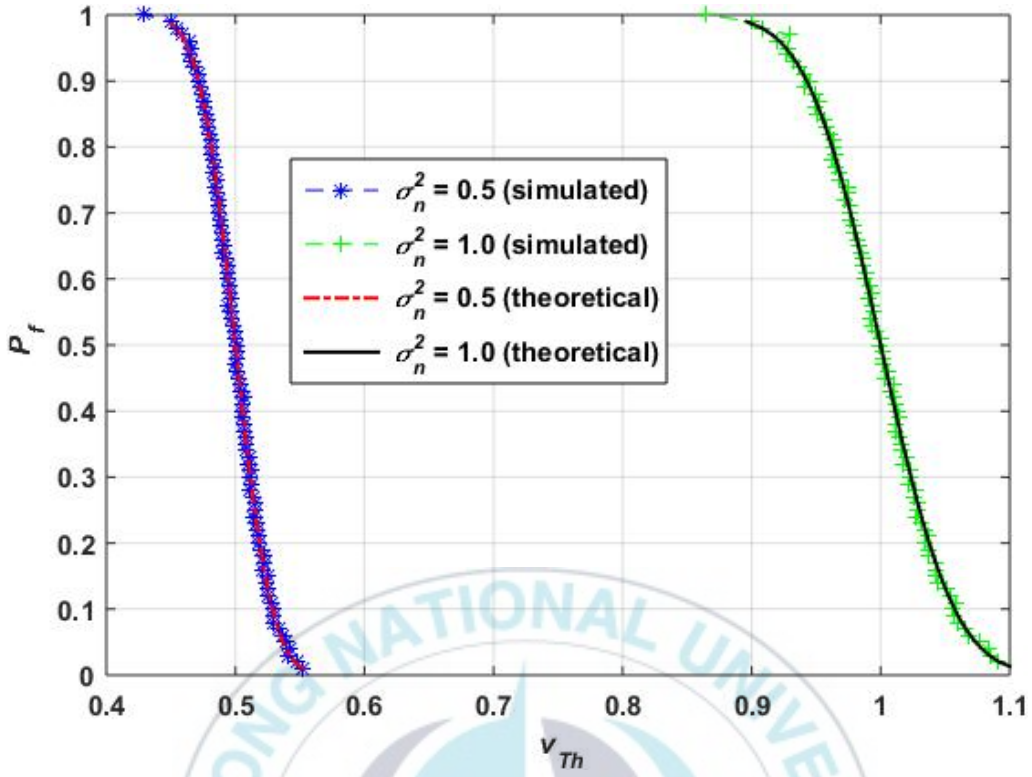


Figure 3.5 Impact of detection threshold on the probability of false alarm.

As a comparative analysis, the performance of the proposed energy detection-based optical spectrum sensing, compared with the conventional energy detection and the Eigen value-based spectrum sensing techniques, is illustrated in Figure 3.6. The average SNR $\gamma_{avg}$ is set to 15 dB. With zero noise uncertainty, the proposed technique with $L = 2$ outperforms the conventional energy detection-based spectrum sensing over the entire ROC region. It is to be noted that the conventional energy detection-based sensing involves measuring the energy of the received signal over a given bandwidth and time duration. It

consists of a square-law device followed by a summation block. For a target of $P_f < 0.1$, the proposed technique outperforms the conventional technique with performance margin can be as high as 25 %. When compared with the Eigen value-based technique, the proposed technique outperforms for $P_f > 0.2$, whereas, when the target is $P_f < 0.2$, the Eigen value-based technique shows better performance.

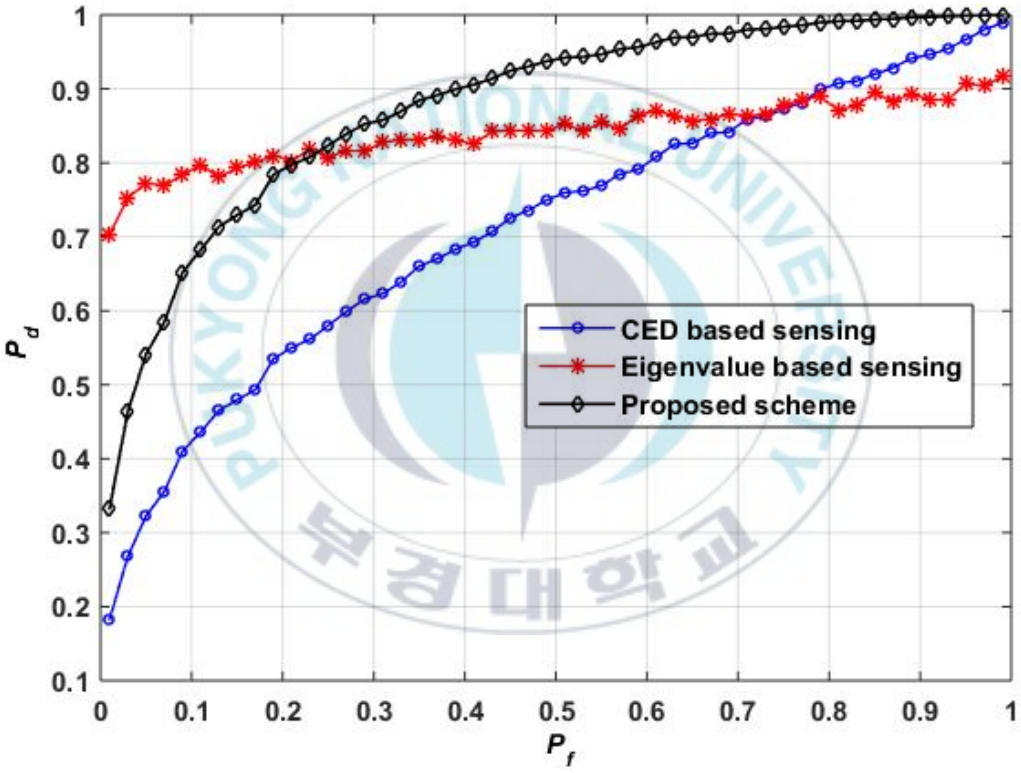


Figure 3.6 Comparative analysis of the proposed energy detection-based optical spectrum sensing with other techniques.

## 3.2 Generic Blind Spectrum Sensing Technique for all Optical Wavelength Multiuser Communications

Next, we present a novel blind optical spectrum sensing technique for all optical-wavelength multiuser communications operating in the Gamma-Gamma distributed atmospheric turbulence channel [42, 43]. The proposed scheme is based on the estimation of the received SNR and the noise power. The estimation is based on a statistical ratio of the received data when the optical channel undergoes turbulence-induced fading. The proposed scheme is significantly different from the conventional energy detection-based spectrum sensing technique as illustrated in Table 3.1.

Table 3.1 Comparison of the proposed technique with the energy detection-based spectrum sensing.

| **Features** | **Proposed technique based on a statistical ratio of the received signal** | **Energy detection based spectrum sensing** |
|---|---|---|
| Detection mechanism | It is based on a statistical ratio of the received signal. The decision is taken on | The decision is made based on the energy level of the received signal. |

| | | |
|---|---|---|
| | based on the estimates of SNR and noise power. | |
| Prior signal and noise information | No prior knowledge of the signal and noise is required. The proposed scheme is blind. | Prior information on noise power is required. Energy detection is not blind detection. |
| False alarm rate | Low | High |
| System model blocks | Only squaring device. No integrator (see Figure 3.7). | Squaring device and integrator (see Figure 3.7). |
| Reliability | Reliable at low SNR values | Unreliable at low SNR values |
| Sensing time | Less | Large sensing time to achieve a good performance. (It is because the energy detection technique measures the energy associated with the received signal over specified time duration.) |

**Proposed technique:**

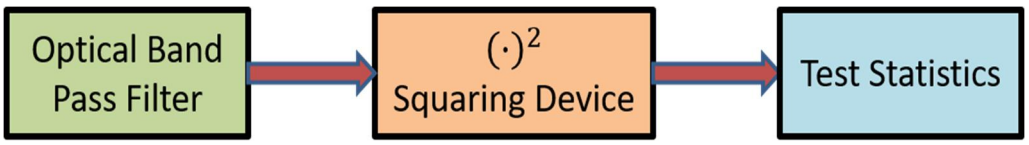


**Energy detection based technique:**

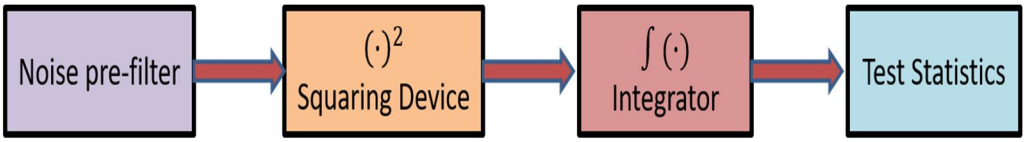


Figure 3.7 Comparative analysis of the proposed technique with the energy detection-based spectrum sensing.

### 3.2.1 System Model

The system model of the proposed blind spectrum sensing technique is illustrated in Figure 3.8. $d$ represents the baseline distance between the transmitter and the receiver. $R_{x_1}$ and $R_{x_2}$ are the two branches of the SSC receiver. The comparator block compares the estimated SNR $\hat{\gamma}$ with the predefined threshold. If the estimated SNR falls below the switching threshold $\gamma_{S_{Th}}$, the SSC receiver is switched to another branch. To decide the availability of the spectrum, the SNR is compared with the detection threshold $\chi_{D_{Th}}$.

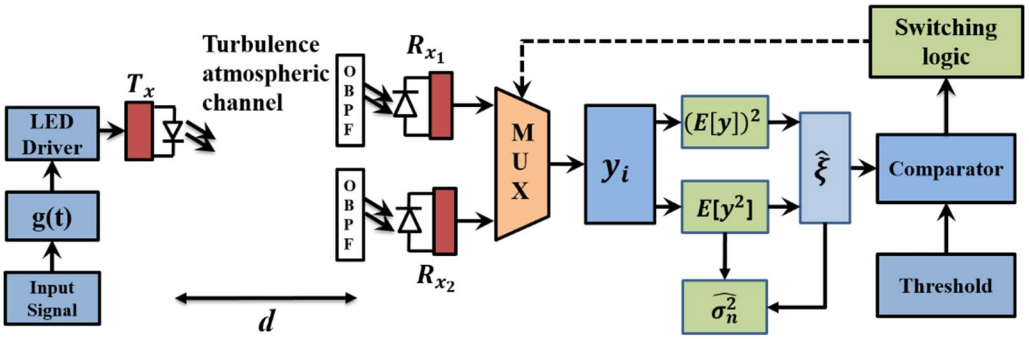


Figure 3.8 System model: Blind spectrum sensing

We denote the presence and absence of the optical signal by hypotheses $H_1$ and $H_0$, respectively. We model the received signal under different hypotheses as

$$y_i = \begin{matrix} SP_r I_i + n_i, & H_1 \\ = n_i, & H_0 \end{matrix}, \tag{3.8}$$

where $S$ is the responsivity, $P_r$ is the received power, and $I_i, i \in \{1, 2\}$ is the irradiance at the $i$th branch. $n_i$ is the noise observed at the $i$th branch. $n_i$ is the AWGN with zero mean and variance $\sigma_n^2$. The second moment of $I_i$ is normalized to unity, that is, $E[I_i^2] = 1$.

### 3.2.2 Blind SNR Estimation

$E\left[y^2\right]$ can be obtained as

$$E\left[y^2\right] = E\left[\left(SP_r I + n\right)^2\right] = S^2 P_r^2 + \sigma_n^2 \quad (3.9)$$

We first find the expected value of $y$. We average $y$ over a random variable $P_r$, then average over $n$ conditioned on $I$, and finally averaged over $I$.

$$E[y_i | n_i, I_i] = \frac{1}{2} E[SP_L P_t I_i + n_i] + \frac{1}{2} E[n_i] = \frac{1}{2} E[SP_L P_t I_i + n_i] \quad (3.10)$$

Averaging over the Gaussian noise $n_i$ conditioned on $I_i$, we obtain

$$E[y_i | I_i = I] = \frac{1}{2\sqrt{2\pi\sigma_n^2}} \int_{-\infty}^{\infty} \left(SP_L P_t I_i + n\right) e^{-\frac{n^2}{2\sigma_n^2}} dn \quad (3.11)$$

$$E[y_i | I_i = I] = \frac{1}{2\sqrt{2\pi\sigma_n^2}} \int_{-\infty}^{\infty} SP_L P_t I_i e^{-\frac{n^2}{2\sigma_n^2}} dn + \frac{1}{2\sqrt{2\pi\sigma_n^2}} \int_{-\infty}^{\infty} n e^{-\frac{n^2}{2\sigma_n^2}} dn \quad (3.12)$$

The first term in Equation (3.12) can be solved by using the identity (Equation 3.323.2) [44]

$$\int_{-\infty}^{\infty} \exp\left(-p^2 x^2 \pm qx\right) dx = \exp\left(\frac{q^2}{4p^2}\right)\left(\frac{\sqrt{\pi}}{|p|}\right). \quad (3.13)$$

It yields

$$\frac{1}{2\sqrt{2\pi\sigma_n^2}} \int_{-\infty}^{\infty} SP_L P_t I_i e^{-\frac{n^2}{2\sigma_n^2}} dw = \frac{SP_L P_t I_i}{2}. \quad (3.14)$$

The second term in Equation (3.12) is the expected value of the random variable whose mean is zero. We define a variable $\beta$ as

$$\beta = \frac{E[y^2]}{\left(E[y]\right)^2} \tag{3.15}$$

where

$$\begin{aligned} E\left[y^2\right] &= E\left[\left(SP_r I + n\right)^2\right] \\ &= S^2 P_r^2 + \sigma_n^2 \end{aligned}. \tag{3.16}$$

$E[y]$ in Equation (3.15) is obtained as

$$E[y] = \frac{SP_L P_t}{\Gamma(a)\Gamma(b)}\left(\frac{1}{a} + \frac{1}{b} + 1\right), \tag{3.17}$$

where the variables $a$ and $b$ are the model parameters of Gamma-Gamma distribution. Utilizing Equations (3.15), (3.16), and (3.17), the relation between $\beta$ and the estimated SNR is obtained as

$$\beta = \frac{\left(2\hat{\xi} + 1\right)\left[\Gamma(a)\Gamma(b)\right]^2}{2\hat{\xi}\left(\frac{1}{a} + \frac{1}{b} + 1\right)^2}. \tag{3.18}$$

### 3.2.3 Estimate of the Noise Power

Under the hypothesis $H_0$, the variable $\beta$ will diverge to infinity. However, in the proposed estimation algorithm, even if $\beta$ tends towards infinity, the value of $\sigma_n^2$ converges to a finite value. Following a series of Equations (3.19), (3.20), (3.21), and (3.22), the noise power can be estimated as

$$\hat{\sigma}_n^2 = \lim_{\beta\to\infty} \frac{E[y^2]}{\left\{\left[\frac{\beta\left(\frac{1}{a}+\frac{1}{b}+1\right)^2}{\left[\Gamma(a)\Gamma(b)\right]^2}-1\right]^{-1}+1\right\}} \tag{3.19}$$

$$\hat{\sigma}_n^2 = \lim_{\beta\to\infty} \frac{E[y^2]}{\left\{\left[\frac{\beta\left(\frac{1}{a}+\frac{1}{b}+1\right)^2-\left[\Gamma(a)\Gamma(b)\right]^2}{\left[\Gamma(a)\Gamma(b)\right]^2}\right]^{-1}+1\right\}} \tag{3.20}$$

$$\hat{\sigma}_n^2 = \lim_{\beta\to\infty} \frac{E[y^2]}{\left\{\frac{\left[\Gamma(a)\Gamma(b)\right]^2}{\beta\left(\frac{1}{a}+\frac{1}{b}+1\right)^2-\left[\Gamma(a)\Gamma(b)\right]^2}+1\right\}} \tag{3.21}$$

$$\hat{\sigma}_n^2 = \frac{E[y^2]}{\left\{\frac{\left[\Gamma(a)\Gamma(b)\right]^2}{\infty}+1\right\}} \tag{3.22}$$

Equation (3.22) yields

$$\hat{\sigma}_n^2 = \frac{E[y^2]}{\{0+1\}} = E[y^2] \tag{3.23}$$

### 3.2.4 Results and Discussions

To quantify the performance of the proposed technique, we obtain the ROC curves under different conditions. The parameters used to obtain the results are given in Table 3.2.

Table 3.2 Simulation parameters.

| Parameters | Values |
|---|---|
| $C_n^2$ | $5 \times 10^{-15}\ m^{-\frac{2}{3}}$ |
| Noise threshold $\sigma_{n,Th}^2$ | 1 |
| Switching threshold $\gamma_{S_{Th}}$ | 4 dB |
| Detection threshold $\gamma_{D_{Th}}$ | 5 dB |

Figure 3.8 illustrates the relationship between the probability of false alarm and the error in the noise power estimation. As can be seen, as the absolute estimation error increases beyond 15%, the probability of false alarm reaches 1. Therefore, an optimal noise threshold value is essential for accurate spectrum sensing.

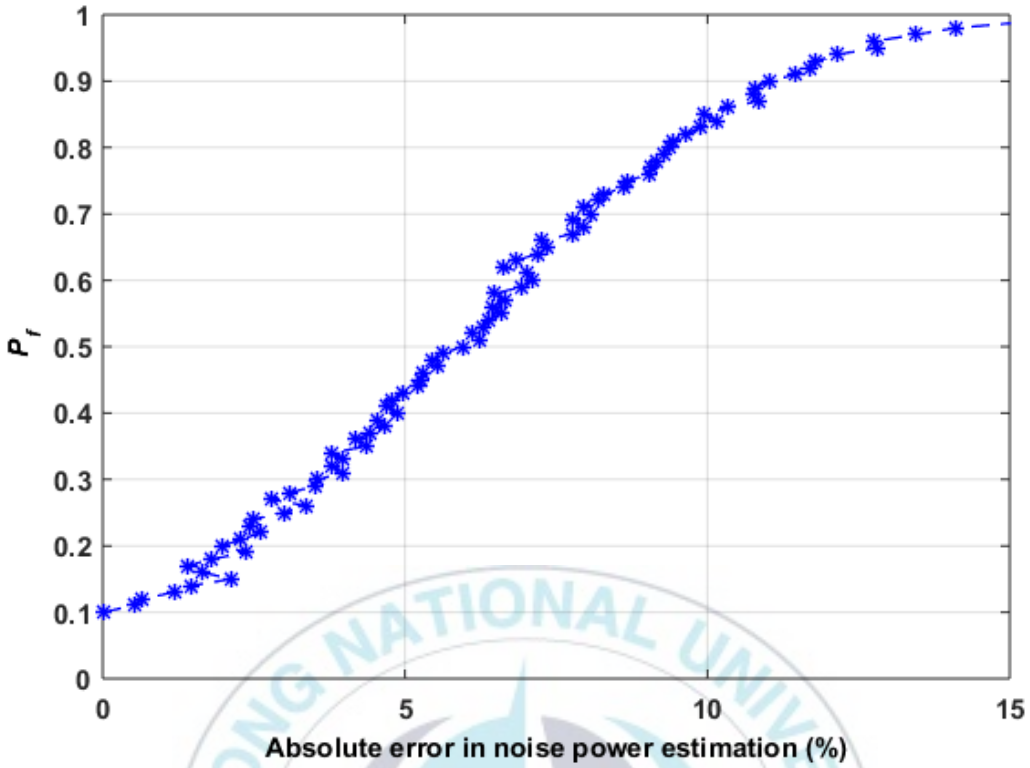


Figure 3.9 Impact of the error in the noise power estimation on the probability of false alarm.

### 3.3 Cooperative Spectrum Sensing for Optical Wireless Multi-Scattering Communications over Málaga Fading

This work formulate a system model to imitate a realistic scenario [45]. We consider a more realistic channel by incorporating multiple scattering trajectories for the photon migrating from the transmitter to the $i$th user. We consider a multiple-scattering correlated fading channel to reflect a practical scenario. The marginal distribution of the fading statistics with arbitrary

correlation is derived. To this end, we propose a novel method based on the Mellin transform to obtain the distribution of the received irradiance in a multiple-scattering correlated fading channel. Considering a more realistic and practical approach, we relax the restriction that the users know the pointing direction and location of the transmitter. That is, we assume that all the users are pointing in arbitrary random directions and are unaware of the transmitter's pointing direction and location.

In this section, we present two novel spectrum sensing techniques in an optical scattering network with an arbitrary number of collaborative users. We first analyze the centralized technique where all the raw data (in the form of statistically dependent random variables) available at the collaborative users are combined using AND rule for the detection of the spectrum. Next, we develop the decentralized spectrum sensing where, instead of sending all the raw data received at the secondary user, only one-bit information is required to be sent to the fusion center to decide the presence of the spectrum.

### 3.3.1 System Model

In this subsection, we formulate a system model to represent a realistic scenario. We consider an optical network as illustrated in Figure 3.9. As depicted, $N_u$ randomly distributed secondary users are deployed in a region within the coverage of the transmitter. We consider non-coplanar link geometry where the

location and pointing direction of each user are selected randomly. The information about the pointing direction and location of the transmitter is not available to the users. Each user makes an independent attempt to sense the transmitted signal by pointing arbitrarily in a random direction. The pointing direction of each user is chosen randomly and is independent of the orientation of other users. However, during a given sensing period, the orientation of each user is fixed. Based on the random location and pointing direction, the sensing capability of each user may vary. Each user experiences turbulence-induced fading with arbitrary correlation, and therefore, the channel condition seen by each user varies with correlated fading. Moreover, for a more accurate estimation of the received power at the user end, we consider multiple scattering channels.

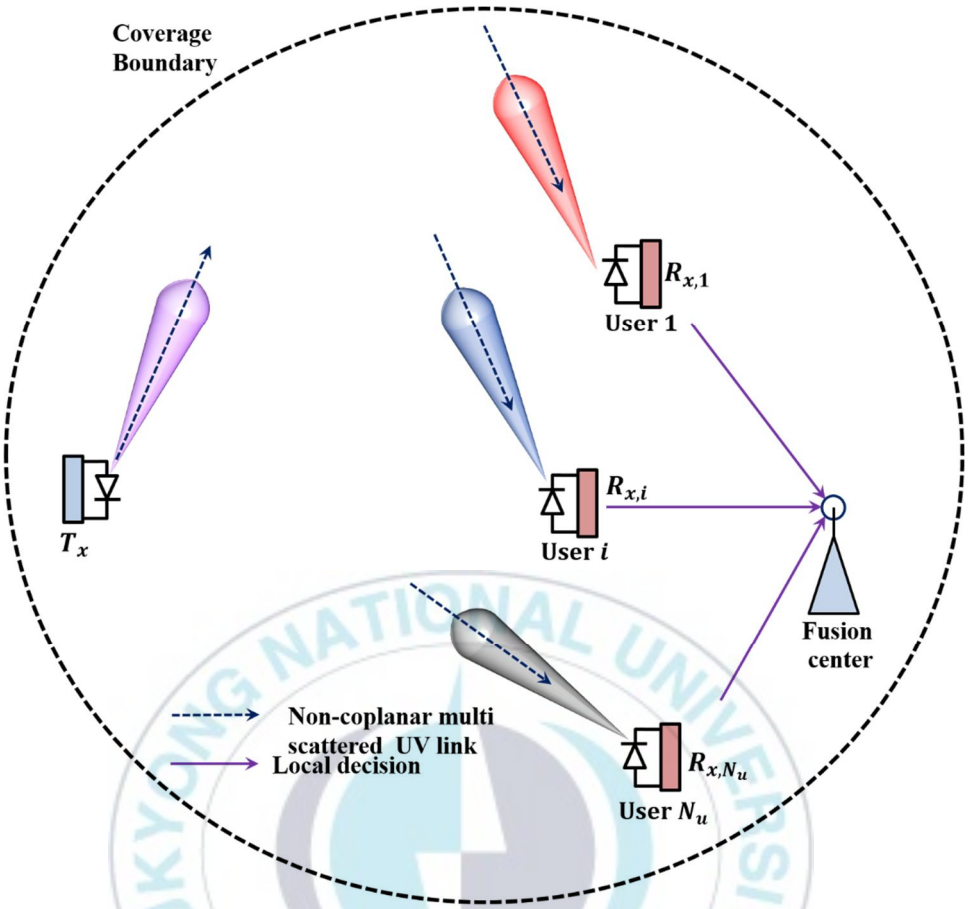


Figure 3.10 Cooperative optical spectrum sensing for non-coplanar NLOS UV communications: Randomly distributed collaborative users with arbitrary random locations and pointing directions.

The important features and the main ideas behind the formulation of the proposed novel system model are summarized as follows.

1. **Randomly Distributed Secondary Users**.

2. **Random Pointing Direction of Individual Users**. In the proposed system, each user makes an independent attempt to sense the transmitter by pointing arbitrarily in a random direction. The pointing direction and location of each user are independent of the pointing directions and locations of other users. Based on the random location and pointing direction, the sensing capability of each user may vary.
3. **Correlated Turbulence Fading.**
4. **Cooperative Diversity.** By leveraging the location flexibility of randomly distributed secondary users, we utilize cooperative diversity.
5. **Non-Coplanar Link Geometry.** As illustrated in Figure 3.10, we consider a non-coplanar link geometry which arises from the fact that the pointing directions of the transmitter and secondary users are chosen randomly.
6. **Multiple Scattering Channels.** A transmission at ultraviolet (UV) wavelength undergoes rich scattering and strong absorption by atmospheric particulates. The single scattering assumption does not always lead to an accurate link performance analysis, especially as the communication range increases. When the

particle density is large or the propagation distance is long, the multiple scattering model provides a more accurate estimation of the received power. The multi-scattered photon trajectory from the transmitter to the receiver is illustrated in Figure 3.11.

7. **Centralized and Decentralized Cooperative Sensing.** We first develop a novel *centralized* cooperative spectrum sensing where all the raw data available at the secondary users are combined by the dedicated link to the fusion center for signal detection. Next, we present a novel *decentralized* cooperative spectrum sensing. The decentralized-based technique overcomes the network overhead problem of the centralized-based technique. In addition, it is shown that the decentralized-based technique outperforms the centralized-based spectrum sensing, particularly at low SNR values.

### 3.3.2 Non-Coplanar NLOS UV Link Geometry

Figure 3.10 illustrates the non-coplanar link geometry. Assuming the transmitter is located at the origin, we take the baseline distance from the transmitter to the $i$th user as the positive $Y$ axis denoted as $Y_i$ $(i \in \{1,\cdots,N_u\})$. The positive $Z$ axis points in the upward direction. Corresponding to $Z$ and $Y_i$ axes, the $X_i$ $(i \in \{1,\cdots,N_u\})$ axis is defined according to the right-handed

coordinate system. $\widehat{z_n}$ and $\widehat{x_{n,i}}$ are the unit vectors perpendicular to the $X_iY_i-$ and $ZY_i-$planes, respectively. The pointing directions of the transmitter and the receiver $R_{x,i}$, corresponding to the $i$th user, are given by the pairs of angles $(\psi_t, \beta_{t,i})$ and $(\psi_r,\ \beta_{r,i})$, respectively. $\psi_t$ is the inclination angle measured between the positive $Z$ axis and the transmit beam axis. $\beta_{t,i}$ represents the azimuth angle measured between the positive $X_i$ axis and the projection of the transmit axis onto the $X_iY_i-$plane. Similarly, the orientation $(\psi_r,\ \beta_{r,i})$ of the $i$th user can be defined. $\phi_t$ and $\phi_r$ are the transmit beam width and the user's FOV, respectively. $d_i$, $1 \le i \le N_u$, denotes the baseline distance between the transmitter and the $i$th receiver.

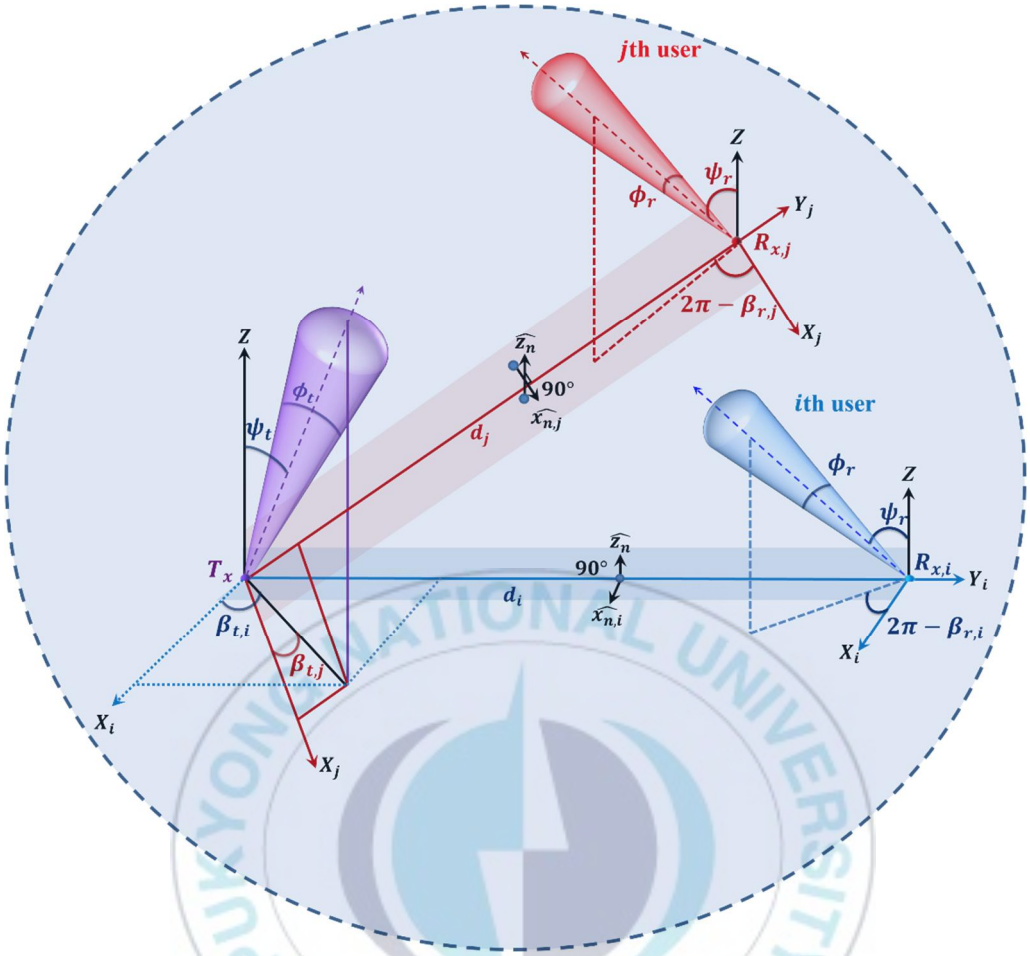


Figure 3.11 Non-coplanar NLOS UV link geometry, illustrating the randomly distributed collaborative users and the transmitter.

For any particular user (say, $i$th user), any of the following cases may occur randomly:

**Case I:** Non-coplanar link geometry with arbitrary pointing directions. Both the transmitter and the $i$th user are oriented in different directions.

$$\begin{cases} \boldsymbol{\beta_{t,i}} \neq \mathbf{90°} \\ \mathbf{2\pi - \boldsymbol{\beta_{R,i}}} \neq \mathbf{90°} \end{cases}$$

**Case II:** Non-coplanar link geometry with the receiver is pointing towards the transmitter.

$$\begin{cases} \boldsymbol{\beta_{t,i}} \neq \mathbf{90°} \\ \mathbf{2\pi - \boldsymbol{\beta_{R,i}}} = \mathbf{90°} \end{cases}$$

**Case III:** Non-coplanar link geometry with the transmitter is pointing towards the $i$th receiver.

$$\begin{cases} \boldsymbol{\beta_{t,i}} = \mathbf{90°} \\ \mathbf{2\pi - \boldsymbol{\beta_{R,i}}} \neq \mathbf{90°} \end{cases}$$

**Case IV:** Coplanar link geometry with both the transmitter and the $i$th receiver are pointing towards each other.

$$\begin{cases} \boldsymbol{\beta_{t,i}} = \mathbf{90°} \\ \mathbf{2\pi - \boldsymbol{\beta_{R,i}}} = \mathbf{90°} \end{cases}$$

### 3.3.3 Multi-Scattered Photon Trajectory

Figure 3.11 illustrates the photon migration from the transmitter to the $i$th user after undergoing multiple scattering events. For the random path between the transmitter and the $i$th user, let the initial direction of the transmitted photon be defined by a pair of angles $(\theta_{0,i}, \zeta_{0,i})$, where $\theta_{0,i}$, $0 \leq \theta_{0,i} \leq \pi$, is the angle measured between the photon's initial direction and the transmit beam axis,

and $\zeta_{0,i}$, $\zeta_{0,i} \in [0, 2\pi)$, represents the angle measured between the orthogonal projection of the emitted photon's trajectory onto the plane perpendicular to the transmit beam axis and a suitable reference in that plane. $I_{l,i}$ represents the marginal distribution of the correlated fading with an arbitrary correlation that a photon experiences over the $l$th scattered path while migrating from the transmitter to the $i$th user.

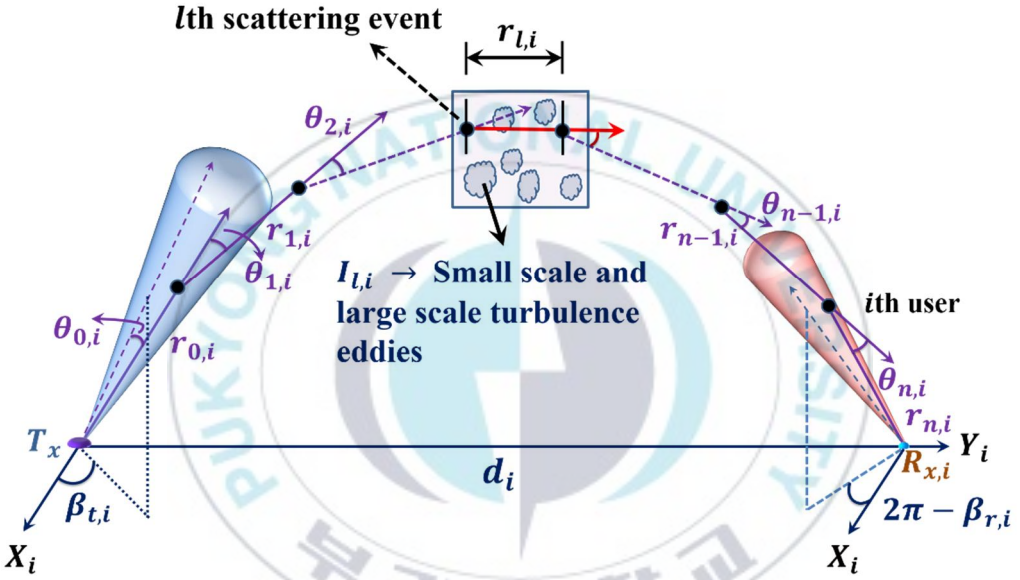


Figure 3.12 UV photon falling into the FOV of the $i$th user after undergoing $n$th order scattering.

The emitted UV ray is decomposed into a set of infinitesimal rays, namely, flows of UV photons [46]. The interaction of the photons with the atmosphere can be modeled as a combined function of absorption and scattering

events. After each interaction between the emitted photon and a scattering center, the photon's trajectory is assumed to follow a law of single scattering until it reaches the next scattering center where it is scattered again or falls into the receiver FOV [47]. Let $r_{l,i}$ denote the distance that a photon traverses between the $l$th and $(l+1)$ th scattering events. The PDF of the distance $r_{l,i} \geq 0$ $(l \in \{0,\dots,n\},\ i \in \{1,\dots,N_u\})$ before being scattered or absorbed, can be modeled as

$$f_{r_{l,i}}\left(r_{l,i}\right) = k_e \exp\left(-k_e r_{l,i}\right), \tag{3.24}$$

where $k_e = k_s + k_a$ is the extinction coefficient. $k_s$ is the total scattering coefficient defined as $k_s = k_s^R + k_s^M$. $k_s^R$ denotes the Rayleigh scattering coefficient, whereas $k_s^M$ is the Mie scattering coefficient. $k_a$ represents the absorption coefficient.

The likelihood that the emitted UV photon undergoes $n$ scattering events before being detected by the receiver is obtained as

$$\begin{aligned} &f_D\left(P_n\right) = \\ &f_{\left(\theta_{0,i},\zeta_{0,i}\right)}\left(\theta_{0,i},\zeta_{0,i}\right)\left[\prod_{l=1}^{n}\frac{k_s}{k_e} f_{r_{l-1,i}}\left(r_{l-1,i}\right) f_{\left(\theta_{l,i},\zeta_{l,i}\right)}\left(\theta_{l,i},\zeta_{l,i}\right)\right], \\ &\times \exp\left(-k_e r_{n,i}\right) P_{FOV}\left(\theta_{R,i},\zeta_{R,i}\right) \end{aligned} \tag{3.25}$$

where $f_{(\theta_{l,i},\zeta_{l,i})}\left(\theta_{l,i},\zeta_{l,i}\right)$ represents the PDF of the scattering angles and $P_{FOV}\left(\theta_{R,i},\zeta_{R,i}\right)$ is the probability of detecting a UV photon that falls onto the receiver [48].

### 3.3.4 Distribution of Received Irradiance

Let $I_{l,i}$ be the irradiance experienced by the UV photon on the $l$th scattered path before falling onto the $i$th detector (user). The final received irradiance at the detector of the $i$th user after experiencing $n$ independent scattering events is given by

$$\begin{aligned} I_{R_i} &= \prod_{l=0}^{n} L_{\alpha_{l,i}} I_{l,i} \\ &= 10^{\left(-\sum_{l=0}^{n}\left(\frac{\alpha_{l,i}}{10}\right)\right)} \prod_{l=0}^{n} I_{l,i} = 10^{\left(-\sum_{l=0}^{n}\left(\frac{\alpha_{l,i}}{10}\right)\right)} I_i^{(n+1)} \end{aligned}, \tag{3.26}$$

where $L_{\alpha_{l,i}}$ represents the attenuation due to the turbulence-induced fading over $l$th scattered path. $I_i^{(n+1)} = \prod_{l=0}^{n} I_{l,i}$. $I_{l,i},\ l \in \{0,\cdots,n\}$, is normalized to unity such that $E\left[I_{l,i}\right] = 1\ \forall\ l \in \{0,\cdots,n\}$. We like to point out that in obtaining Equation (3.26), we assume that the two successive scattering events, $l$th and $(l+1)$th, are independent [46, 49, 50]. Utilizing the fact that $I_{l,i} \geq 0\ \forall\ l \in \{0,\cdots$

$\cdot, n\}$, we apply the Mellin transform to obtain the PDF of $I_{R_i}$. The Mellin transform of any function $f_{I_{l,i}}(I_{l,i}), I_{l,i} \geq 0$, is defined as [51]

$$M\left[f_{I_{l,i}}\left(I_{l,i}\right);s\right]=\int_0^\infty f_{I_{l,i}}\left(I_{l,i}\right)I_{l,i}^{s-1}dI_{l,i} \quad . \tag{3.27}$$

$f_{I_{l,i}}(I_{l,i})$ is the marginal distribution of the irradiance at the $l$th scattered path with arbitrary correlation and is derived as

$$\begin{aligned}
&f_{I_{l,i}}\left(I_{l,i}\right)\\
&=\frac{|\mathbf{W}|^{\alpha}}{\Gamma(\alpha)}\left(\frac{\alpha+1}{\alpha^2}\right)^{-\alpha N_u-2}(2)^{1-N_u}\left[\frac{1}{\gamma}\left(\frac{\gamma\beta}{\gamma\beta+\Omega'}\right)^{\beta}\right]^{N_u}\\
&\times\sum_{q_1,\cdots,q_{N_u-1}=0}^{\infty}\left\{\left(\sum_{j=1}^{N_u-1}q_j\right)\left(\prod_{z=1}^{N_u-1}\frac{\left|w_{z,z+1}\right|^{2q_z}}{\Gamma(\alpha+q_z)q_z!}\right)\right.\\
&\times\prod_{\substack{p=1\\p\neq i}}^{N_u}\left[\sum_{k=1}^{\beta}\frac{(-1)^{k-1}}{(k-1)!}\binom{\beta-1}{k-1}\left(\frac{-\Omega'}{\gamma(\gamma\beta+\Omega')}\right)^{k-1}\Gamma(\alpha+Q_P)\Gamma(k)\left(\frac{\beta\alpha^2w_{p,p}}{(\gamma\beta+\Omega')(\alpha+1)}\right)^{-\frac{\alpha+Q_p+k}{2}}\right]\\
&\times\left[\sum_{k=1}^{\beta}\frac{(-1)^{k-1}}{(k-1)!}\binom{\beta-1}{k-1}\left(\frac{-\Omega'}{\gamma(\gamma\beta+\Omega')}I_{l,i}\right)^{k-1}\right.\\
&\times\left(\frac{2\beta(\alpha+1)}{\alpha^2(\gamma\beta+\Omega')w_{i,i}}I_{l,i}\right)^{\left(\frac{\alpha+Q_i-k}{2}\right)}\\
&\left.\left.\times K_{\alpha+Q_i-k}\left(2\sqrt{\frac{\beta\alpha^2w_{i,i}}{(\gamma\beta+\Omega')(\alpha+1)}I_{l,i}}\right)\right]\right\}
\end{aligned} \tag{3.28}$$

where $\boldsymbol{W}$ denotes the inverse of the correlation matrix. $0 \leq w_{i,j} < 1$ is the correlation coefficient, with $1 \leq i,j \leq N_u$. We derive the Mellin transform of $f_{I_{l,i}}\left(I_{l,i}\right)$ as

$$M\left[f_{I_{l,i}}\left(I_{l,i}\right);s\right]=\frac{|\mathbf{W}|^{\alpha}}{\Gamma(\alpha)}\left(\frac{\alpha+1}{\alpha^2}\right)^{-\alpha N_u-2}\left[\frac{1}{2\gamma}\left(\frac{\gamma\beta}{\gamma\beta+\Omega'}\right)^{\beta}\right]^{N_u}$$
$$\times\sum_{q_1,\cdots,q_{N_u-1}=0}^{\infty}\left\{\binom{N_u-1}{\sum_{j=1}^{N_u-1}q_j}\left(\prod_{z=1}^{N_u-1}\frac{\left|w_{z,z+1}\right|^{2q_z}}{\Gamma(\alpha+q_z)q_z!}\right)\right.$$
$$\times\prod_{\substack{p=1\\p\neq i}}^{N_u}\left[\sum_{k=1}^{\beta}\frac{(-1)^{k-1}}{(k-1)!}\binom{\beta-1}{k-1}\left(\frac{-\Omega'}{\gamma(\gamma\beta+\Omega')}\right)^{k-1}\Gamma(\alpha+Q_P)\Gamma(k)\left(\frac{\beta\alpha^2 w_{p,p}}{(\gamma\beta+\Omega')(\alpha+1)}\right)^{-\frac{\alpha+Q_p+k}{2}}\right]$$
$$\times\left[\sum_{k=1}^{\beta}\frac{(-1)^{k-1}}{(k-1)!}\binom{\beta-1}{k-1}\left(\frac{-\Omega'}{\gamma(\gamma\beta+\Omega')}\right)^{k-1}\left(\frac{2\beta(\alpha+1)}{\alpha^2(\gamma\beta+\Omega')w_{i,i}}\right)^{\left(\frac{\alpha+Q_i-k}{2}\right)}\right.$$
$$\left.\left.\times\Gamma(\alpha+Q_i+s-1)\Gamma(k+s-1)\left(\frac{\beta\alpha^2 w_{i,i}}{(\gamma\beta+\Omega')(\alpha+1)}\right)^{1-s-\left(\frac{\alpha+Q_i+k}{2}\right)}\right]\right\} \tag{3.29}$$

### 3.3.5 Distribution of Photons Arrival Rate

The photons arrival rate corresponding to the $i$th user is given by $\lambda_s^i = \frac{\eta E_{n,R_i} I_{R_i}}{h\nu}$, where $\eta$ represents the optical-to-electrical conversion efficiency and $E_{n,R_i}$ is the total received energy at the $i$th user after $n$ scattering events. $h$

denotes Planck's constant and $v$ is the center frequency of the transmitted UV signal. $I_{R_i}$ is defined in Equation (3.26). Conditioned on $E_{n,R_i}$, the photon arrival rate $\lambda_s^i$ follows the distribution of $I_{R_i}$ [52]. Following this, the PDF of $\lambda_s^i$ can be obtained as

$$f_{\lambda_s^i}\left(\lambda_s^i\right) = \frac{hv}{\eta E_{n,R_i}} f_{R_i}\left(\frac{hv\lambda_s^i}{\eta E_{n,R_i}}\right). \tag{3.30}$$

We define the average received SNR as the ratio of the square of the expected mean of the signal component that corresponds to the transmitted information to the total variance of the received signal [53]. It yields

$$\gamma_{i,avg} = \frac{\left(\eta E_{n,R_i} E\left[I_{R_i}\right]\right)^2}{2\eta E_{n,R_i} E\left[I_{R_i}\right] hv + 4\lambda_b h^2 v^2}. \tag{3.31}$$

### 3.3.6 Cooperative Spectrum Sensing with Centralized Technique

We develop the centralized spectrum sensing where all the raw data, that is, the number of received photons ($N_{p,j}^i$) received at collaborative secondary users, are transferred to the fusion center to make the final decision. In this technique, it is assumed that the decision-making capability is only available at the fusion center. Therefore, in the centralized technique, the collaborative users

periodically send the information about the number of received photons to the fusion center that utilizes this information and decides the spectrum.

Let $N_{p,j}^{S}$ be the sum of $N_u$ statistically dependent random variables $N_{p,j}^{i}$ for $1 \le i \le N_u$, such that

$$N_{p,j}^{S} \equiv \sum_{i=1}^{N_u} N_{p,j}^{i} . \tag{3.32}$$

Utilizing the chain rule of the probability theory, the joint PMF of the received photoelectrons can be expressed by

$$\begin{aligned} & P_{\Lambda_1,\cdots,\Lambda_i\cdots,\Lambda_{N_u}}\left(N_{p,j}^{1},\cdots,N_{p,j}^{i}\cdots,N_{p,j}^{N_u}\right) \\ & = P_r\left\{\Lambda_1 = N_{p,j}^{1}\right\} P_r\left\{\Lambda_2 = N_{p,j}^{2} \middle| \Lambda_1 = N_{p,j}^{1}\right\} \\ & \times P_r\left\{\Lambda_3 = N_{p,j}^{3} \middle| \Lambda_1 = N_{p,j}^{1}, \Lambda_2 = N_{p,j}^{2}\right\} \\ & \cdots \\ & \times P_r\left\{\Lambda_{N_u} = N_{p,j}^{N_u} \middle| \Lambda_1 = N_{p,j}^{1},\cdots,\Lambda_i = N_{p,j}^{i},\cdots,\Lambda_{N_u} = N_{p,j}^{N_u}\right\} \end{aligned} , \tag{3.33}$$

such that

$$\sum_{N_{p,j}^{1}}\cdots\sum_{N_{p,j}^{i}}\cdots\sum_{N_{p,j}^{Nu}} P_{\Lambda_1,\cdots,\Lambda_i\cdots,\Lambda_{N_u}}\left(N_{p,j}^{1},\cdots,N_{p,j}^{i}\cdots,N_{p,j}^{N_u}\right) = 1. \tag{3.34}$$

The distribution of the number of detected photoelectrons at the fusion center, contributed by the $i$th collaborative user, can be formulated as

$$P_r\left\{\Lambda_i = N_{p,j}^i\right\} =$$

$$\int_0^\infty \sum_{k=1}^{Z} P_r\left\{\lambda_s^i = \varepsilon_k\right\} P_r\left\{\Lambda_i = N_{p,j}^i \middle| \lambda_s^i = \varepsilon_k\right\} f_{\lambda_s^i}\left(\lambda_s^i\right) d\lambda_s^i$$

$$= \int_0^\infty \sum_{k=1}^{Z} P_r\left\{\lambda_s^i = \varepsilon_k\right\} \frac{\left(\varepsilon_k + \lambda_b\right)^{N_{p,j}^i}}{N_{p,j}^i\,!} \exp\left[-\left(\varepsilon_k + \lambda_b\right)\right] f_{\lambda_s^i}\left(\lambda_s^i\right) d\lambda_s^i \tag{3.35}$$

At the fusion center, the mean of the sum of the received UV photon counts is then given by

$$< N_{p,j}^S > \; = E\left[N_{p,j}^S\right] =$$

$$\int_0^\infty \sum_{i=1}^{N_u} N_{p,j}^i P_{\Lambda_1,\cdots,\Lambda_i\cdots,\Lambda_{N_u}}\left(N_{p,j}^1,\cdots,N_{p,j}^i\cdots,N_{p,j}^{N_u}\right) dN_{p,j}^1 \cdots dN_{p,j}^{N_u} \tag{3.36}$$

Convolving Equation (3.35) for $1 \le i \le N_u$, the distribution of $N_{p,j}^S$ can readily be evaluated as

$$P_r\left\{\Lambda_S = N_{p,j}^S\right\} =$$
$$P_r\left\{\Lambda_1 = N_{p,j}^1\right\} * P_r\left\{\Lambda_2 = N_{p,j}^2\right\} * \cdots * P_r\left\{\Lambda_{N_u} = N_{p,j}^{N_u}\right\} . \tag{3.37}$$

Utilizing Equations (3.36) and (3.37), the probability of detection and the probability of false alarm can then be obtained as

$$P_{d,CSS}^{C} = P_r\left\{E\left[N_{p,j}^{S}\right] > N_u N_{Th} \middle| H_1\right\}, \tag{3.38}$$

and

$$P_{f,CSS}^{C} = P_r\left\{E\left[N_{p,j}^{S}\right] > N_u N_{Th} \middle| H_0\right\}. \tag{3.39}$$

The decision rule at the fusion center can then be formulated as

$$\frac{P_r\left\{\Lambda_S = N_{p,j}^{S} \middle| \Delta_C = 1\right\}}{P_r\left\{\Lambda_S = N_{p,j}^{S} \middle| \Delta_C = 0\right\}} \begin{matrix} \hat{\Delta}_C = 1 \\ > \\ < \\ \hat{\Delta}_C = 0 \end{matrix} 1 \quad . \tag{3.40}$$

***Remark 3.1:*** *As can be seen from Equation* (3.35)*, the distribution of the number of photoelectrons detected* $N_{p,j}^{i}$ *contributed by the* $i$*th user is characterized by the mixed Poisson distribution. However, the distribution of the total number of received photons contributed by all the collaborative users at the fusion center* $N_{p,j}^{S} \equiv \sum_{i=1}^{N_u} N_{p,j}^{i}$ *does not necessarily obey the Poisson distribution, as can be readily seen in Equation* (3.37).

### 3.3.7 Results and Discussions

Algorithm 3.1 Procedure to Capture the Turbulence Effect in Multi-Scattered UV Channel and to Estimate the Total Received Energy of the Received Photon after Undergoing $n$ Scattering Events.

**Input:** $\phi_t, \phi_r, \psi_t, \psi_r, N_u$

**Input:** Turbulence and scattering model parameters:
$\gamma_R, g_M, f_M, \alpha, \beta, \Omega, b_0, \rho, \boldsymbol{W}$

**Input:** Transmitter coordinates: $(X, Y, Z) = (0, 0, 0)$

1. **Compute** $A$, and $a_k$
2. **Randomly generate $N_u$ uniformly distributed users** → To get randomly distributed collaborative users pointing in arbitrary random directions over the domain, generate $N_u$ pairs of independent random variables $(d_i, \beta_{t,i}, \beta_{r,i})$ for $1 \leq i \leq N_u$, as follows:
3. $d_i$ is uniformly distributed in the interval $[5, 50]$
4. $\beta_{t,i}$ is uniform in the interval $\left[0, \frac{\pi}{6}\right]$
5. $\beta_{r,i}$ is uniformly distributed between the interval $\left[-\frac{2\pi}{3}, -\frac{\pi}{3}\right]$
6. **for** $i = 1$ to $N_u$ **do**
7. Randomly define the initial trajectory of the emitted photons $(\theta_{0,i}, \zeta_{0,i})$, such as:
8. $\theta_{0,i}$ is distributed in the interval $[0, \pi]$
9. $\zeta_{0,i}$ is distributed in the interval $[0, 2\pi]$
10. **for** $l = 1$ to $n$ **do**

11. **Capture the Effect of Multiple Scattering →**

12. Randomly generate a variable $r_{l,i}$ with PDF given by Equation (3.24)

13. For each scattering center generate a new trajectory defined by $(\theta_{l,i}, \zeta_{l,i})$, such as:

14. $\theta_{l,i}$ is distributed in the interval $[0, \pi]$ with joint PDF given by (6)

15. $\zeta_{l,i}$ is distributed in the interval $[0, 2\pi]$ with joint PDF given by (6)

16. Record all the scattered paths from the sampled beam

17. **Capture the Effect of Turbulence →**

18. **Compute:** Attenuation due to atmospheric turbulence $L_{\alpha_{l,i}}$

19. Randomly generate a variable $I_{l,i}$ following the distribution given by Equation (3.28)

20. Obtain the Mellin transform of $f_{I_{l,i}}(I_{l,i})$ using Equation (3.29)

21. **Compute:** $P_{FOV}(\theta_{R,i}, \zeta_{R,i})$ using (7)

22. **Compute:** The distribution of the received irradiance $f_{I_{R,i}}(I_{R,i})$ using (31)

23. **Compute:** $P_{n,i}$ such that the intensity of the received irradiance should obey the PDF in (31)

24. **Compute:** $E_{n,R_i}$

The probability of detection relative to the target probability of false alarm is depicted in Figure 3.12. For comparative analysis, we plot both centralized and decentralized cooperative spectrum sensing. The number of collaborative users $N_u$ is set to $20$. For brevity, the fading is assumed to be uncorrelated. At a low background radiation rate, that is, $\lambda_b = 1 \times 10^4$ per second, the decentralized technique outperforms the centralized-based cooperative spectrum sensing by $5.81\%$ when the probability of false alarm is set to $0.5$. However, when the background radiation increases by $5$ times, the performance gap increases to $42\%$ for the same target probability of false alarm. This performance behavior is due to the fact that in a centralized-based cooperative spectrum sensing, the fusion center makes a binary decision based

on the possibly less accurate and statistically dependent raw data received from the cooperative users.

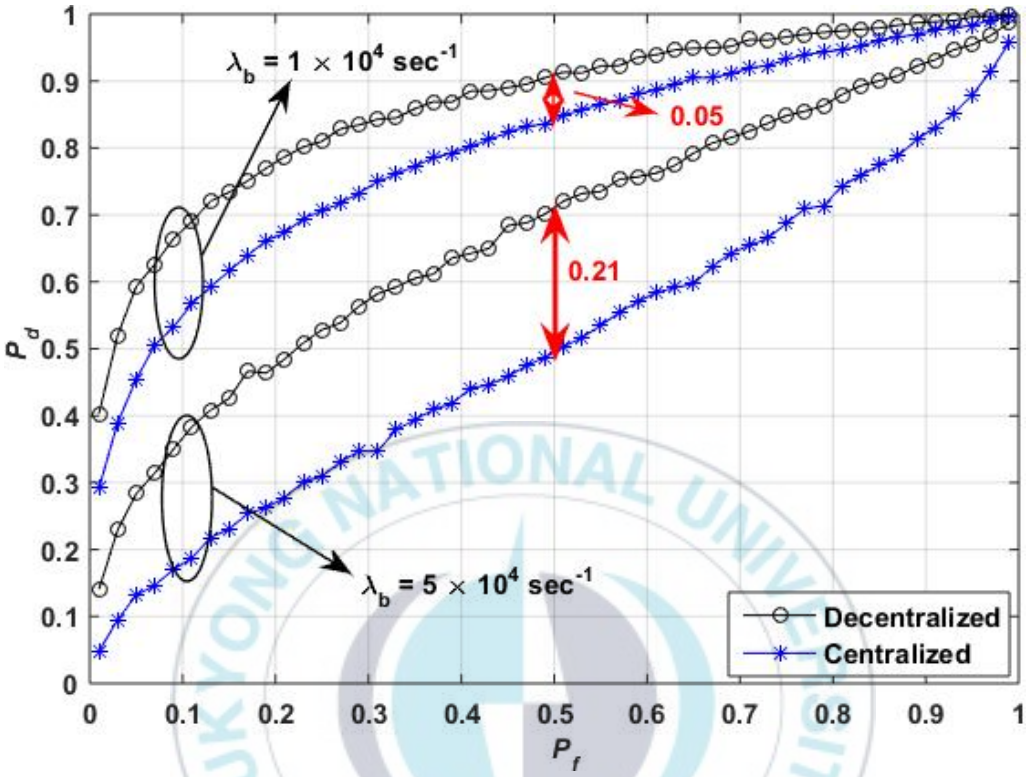


Figure 3.13 ROC curves illustrating the centralized and decentralized cooperative spectrum sensing.

The impact of the number of collaborative users participating in the spectrum sensing is illustrated in Figure 3.12. We consider correlated fading with the correlation coefficient set to 0.2. From the results, we like to point out that utilizing the raw data from the collaborative users does not always result in

optimum performance when the received signal is weak. For instance, at $N_u = 10$, from the context of the probability of detection, the difference between the two proposed techniques increases from 0.02 to 0.15, when the average received SNR decreases from 15 dB to 0 dB. Another important observation can be inferred that at low SNR values, the performance gap between the centralized and dencentralized based spectrum sensing techniques increases with the number of collaborative users.

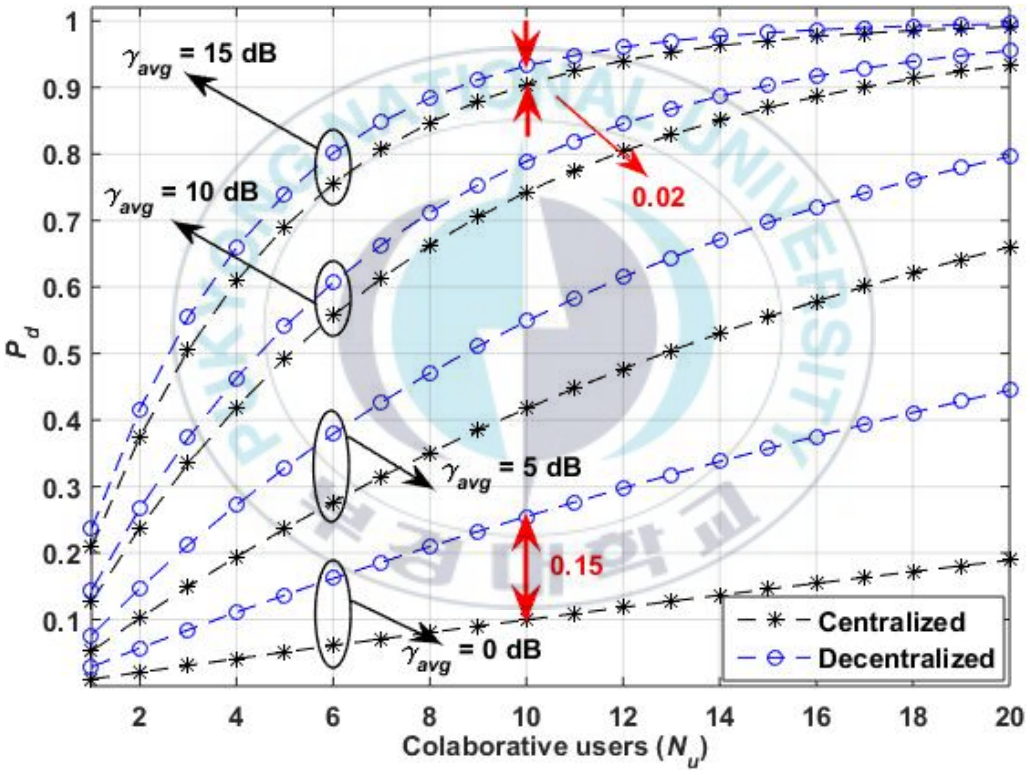


Figure 3.14 Average probability of detection against the number of collaborative users.

Figure 3.14 shows the average error rate $P_{error}$ relative to the number of collaborative users $N_u$ for the two proposed techniques. The fading is assumed to be correlated with fading coefficient set to 0.2. Similar to the results obtained in Figure 3.13, an important observation can be inferred that as the received SNR reduces, the difference between the error rates obtained in the two techniques increases. It is also interesting to note that, at higher SNR values, for instance $\gamma_{avg} = 15$ dB, the difference between error rates shrinks, irrespective of the number of collaborative users.

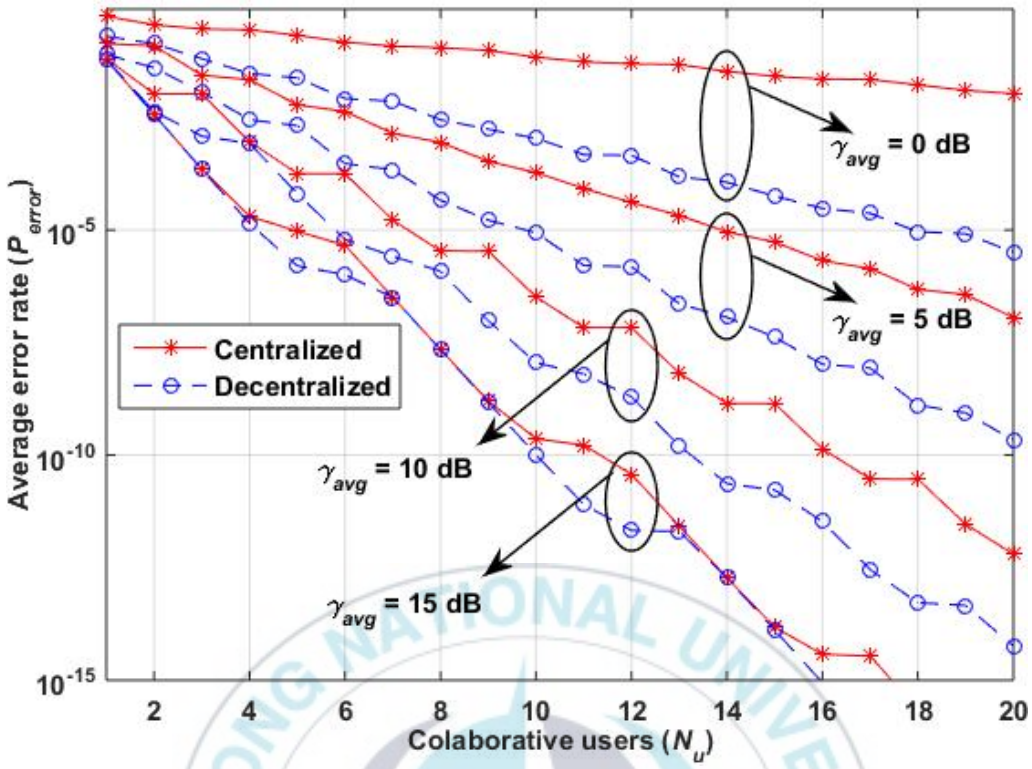


Figure 3.15 Average error rate analysis in centralized and decentralized based optical spectrum sensing.

## 3.4 Artificial Bee Colony Based Heuristic Algorithm for Optical Spectrum Sensing

The major shortcomings in optical spectrum sensing are the uncertainty in the noise power and correlated optical signal. These shortcomings can potentially lead to a performance impairment in signal detection. Therefore, the motivation of this work is to develop an optical detection technique that is

optimal in the sense of the detection threshold and is also robust against the performance impairment in the multiuser correlated optical turbulence fading channel. To this end, we develop an artificial bee colony (ABC) based optimal spectrum sensing technique using an eigenvalue based detection (EVD) for multiuser OWC systems. However, it should be noted that the conventional EVD [54] is not directly applicable to the present optical channel; therefore, a modified EVD is developed for the present study. The EVD can mitigate these shortcomings, but it has a limitation on determining an optimal threshold value. To overcome the limitations of the EVD, we develop a novel ABC-based optimization framework using the EVD in the optical wireless channel. ABC is a heuristic optimization algorithm inspired by the intelligent behavior of foraging honeybees. It exhibits good exploration capability and easy implementation.

### 3.4.1 System Model and Methodology

The ABC algorithm is a swarm intelligence optimization algorithm. It simulates the intelligent behavior of foraging honeybees. Inspired by this, the ABC algorithm gets the optimal solution by searching the neighborhood of the present solution in the search process. The advantages include good exploration capability and easy implementation.

It uses a colony of artificial honeybees. The honeybees in the colony are grouped into three types: employed, onlooker, and scout honeybees. The aim of bees in the ABC algorithm is to find the best optimal solution. Each employed honeybee is connected with a food source, that is, the effective number of food sources is equal to the employed honeybees. The first half of the colony consists of the employed honeybees. The second half of the colony includes onlooker honeybees. Analogously, in the context of the optimization problem, the position of a food source denotes a promising solution to the optimization problem. The number of employed honeybees is equivalent to the number of solutions. The amount of nectar present in each food source is equivalent to the fitness of the corresponding solution, that is, the quality of the particular solution.

In the ABC, the task of the employed honeybees is to perform global searching and to find new food sources (a possible solution to the optimization problem). The information of the nectar (quality of the particular solution) present in the food source is then passed onto the onlooker honeybees. The onlooker honeybees select one employed honeybee using a roulette wheel selection process and perform a local search for a new food source in the vicinity of the chosen one. If the quality of the food source is not improved after a given number of trials, then that food source (solution) will be abandoned and the scout

honeybee will randomly generate a new food source, thereby avoiding the local optima.

The proposed system model is illustrated in Figure 3.16.

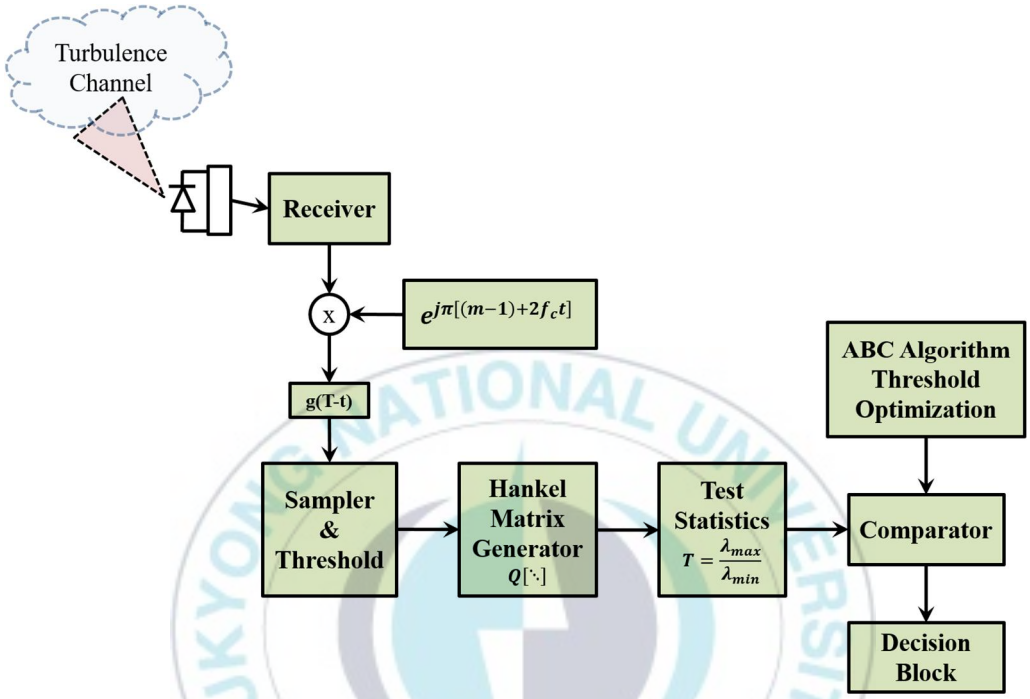


Figure 3.16 Methodology: ABC-based optical spectrum sensing.

The optimization problem can be formulated as

$$\begin{aligned} &\text{minimize:} && \Omega_i, i \in \{1, \cdots, N_p\} \\ &\text{subject to:} && P_f = P_{f,\text{Target}} \text{ and } L_{\min} \le L_i \le L_{\max} \end{aligned} \tag{3.26}$$

where $\Omega_i$ is the objective function defined as $\Omega_i = P_{d,Target} - P_{d,i}$. $P_{d,Target}$ is the target probability of detection. $P_{d,i}$ is the probability of detection at the $i$th

solution and $N_p$ represents the total number of possible solutions. In this optimization problem, the probability of false alarm $P_f$ is the equality constraint and the smoothing factor $L_i$ is the inequality constraint. The fitness value of the possible solution to the quantization problem is formulated as

$$f_i = \begin{cases} \dfrac{1}{1+\Omega_i}, & \Omega_i \geq 0 \\ 1+\mathrm{abs}(\Omega_i), & \Omega_i < 0 \end{cases} \tag{3.27}$$

where $\mathrm{abs}(\cdot)$ denotes the absolute value. A higher fitness value represents a minimum objective function value and the better possible solution to the optimization problem.

Algorithm 3.2 simulates the behavior of honeybees foraging for food sources with the maximum nectar amount. A food source foraged by honeybees represents a possible solution to the optimization problem.

**Algorithm 3.2 Optimization of the detection threshold using ABC.**

**Input:** Upper bound $L_{\max}$, Lower bound $L_{\min}$

*Initialization:* Stagnation limit $K$

1. Randomly generate $N_p$ number of initial solutions $L_i$ given by
2. **for** $i = 1$ to $N_p$ **do**

3. $L_i = L_{\min} + rand(0,1)(L_{\max} - L_{\min})$

4. **end for**

*Initialization:* Employed honeybee trial counter, $T(L_i) = 0$

5. **Evaluate:** Objective function values for the initial solutions

***The employed honeybees phase:***

6. **for** $i = 1$ to $N_p$ **do**

7. Choose an index $j$ such that $j \in \{1, 2, \cdots, N_p\}$ and $j \neq i$

8. Generate new solutions (food source positions) $V_i$ in the neighborhood of $L_i$ through $V_i = L_i + \psi_i(L_i - L_j)$

9. Apply the greedy selection process between $L_i$ and $V_i$ and save the better one

10. **if** $\Omega(V_i) < \Omega(L_i)$ **then**

11. $L_i \leftarrow V_i$ and $T(L_i) \leftarrow 0$

12. **else**

13. $T(L_i) \leftarrow T(L_i) + 1$

14. **end if**

15. **Calculate:** The fitness function $f_i$ for each solution:

$$f_i = \begin{cases} \dfrac{1}{1+\Omega_i}, & \Omega_i \geq 0 \\ 1+\mathrm{abs}(\Omega_i), & \Omega_i < 0 \end{cases}$$

16. **Compute:** The probability values $p_i$ of choosing the solution using $p_i = \frac{f_i}{\sum_{i=1}^{N_p} f_i}$

***The onlooker honeybees phase:***

17. Produce the new optimal solutions $V_i$ depending on $p_i$ and evaluate $f(V_i)$

18. Run the greedy selection process for the onlooker honeybees

19. **if** $\Omega(V_i) < \Omega(L_i)$ **then**

20. $L_i \longleftarrow V_i$ and $T(L_i) \longleftarrow 0$

21. **else**

22. $T(L_i) \longleftarrow T(L_i) + 1$

23. **end if**

***The scout honeybees phase:***

24. **if** $T(L_i) > K$ **then**

Identify the abandoned solution for the scout honeybees and replace it with new randomly produced solutions $L_i$ using

$$L_i = L_{\min} + rand(0,1)(L_{\max} - L_{\min})$$

25. $T(L_i) \leftarrow 0$

26. **else**

27. Record the best optimal solution

28. **end if**

29. **end for**

30. **return** $L_{opt}$

Algorithm 3.3 depicts the ABC-based optical spectrum sensing using EVD.

**Algorithm 3.3 ABC-based optical spectrum sensing.**

**Given:** Target probability of detection $P_{d,Target}$

**Input:** Number of samples $N_s$

**Input:** Number of iterations $I_{\max}$

**Input:** Probability of false alarm $P_f$

*Initialization:* $L$

*Initialziation:* Counter $C = 0$

1. **for** $i = 1$ to $I_{\max}$ **do**

2. Generate the Hankel matrix $Q$ of order $(N_s - L + 1) \times L$

3. **Compute:** $\lambda_{\max}$ and $\lambda_{\min}$ through SVD of Q

4. **Compute:** $\lambda_{Th}$

5. Generate the test statistics for the optical signal detection:

   $T = \frac{\lambda_{\max}}{\lambda_{\min}}$

6. **if** $(T > \lambda_{Th})$ **then**

7. $C = C + 1$

8. **end if**

9. **end for**

10. **Compute:** $\boldsymbol{P_d = \frac{C}{I_{\max}}}$

11. **Compute:** $P_{d,error} = P_{d,Total} - P_d$

12. **Call:** Algorithm 3.2 for optimization of the smoothing factor $L$

    *Initialization:* Employed honeybee trial counter, $T(L_i) = 0$

13. Update $L$: $L = L_{opt}$

14. Go to step 1

15. **return** $P_d$

### 3.4.2 Flowchart: ABC-based Threshold Optimization

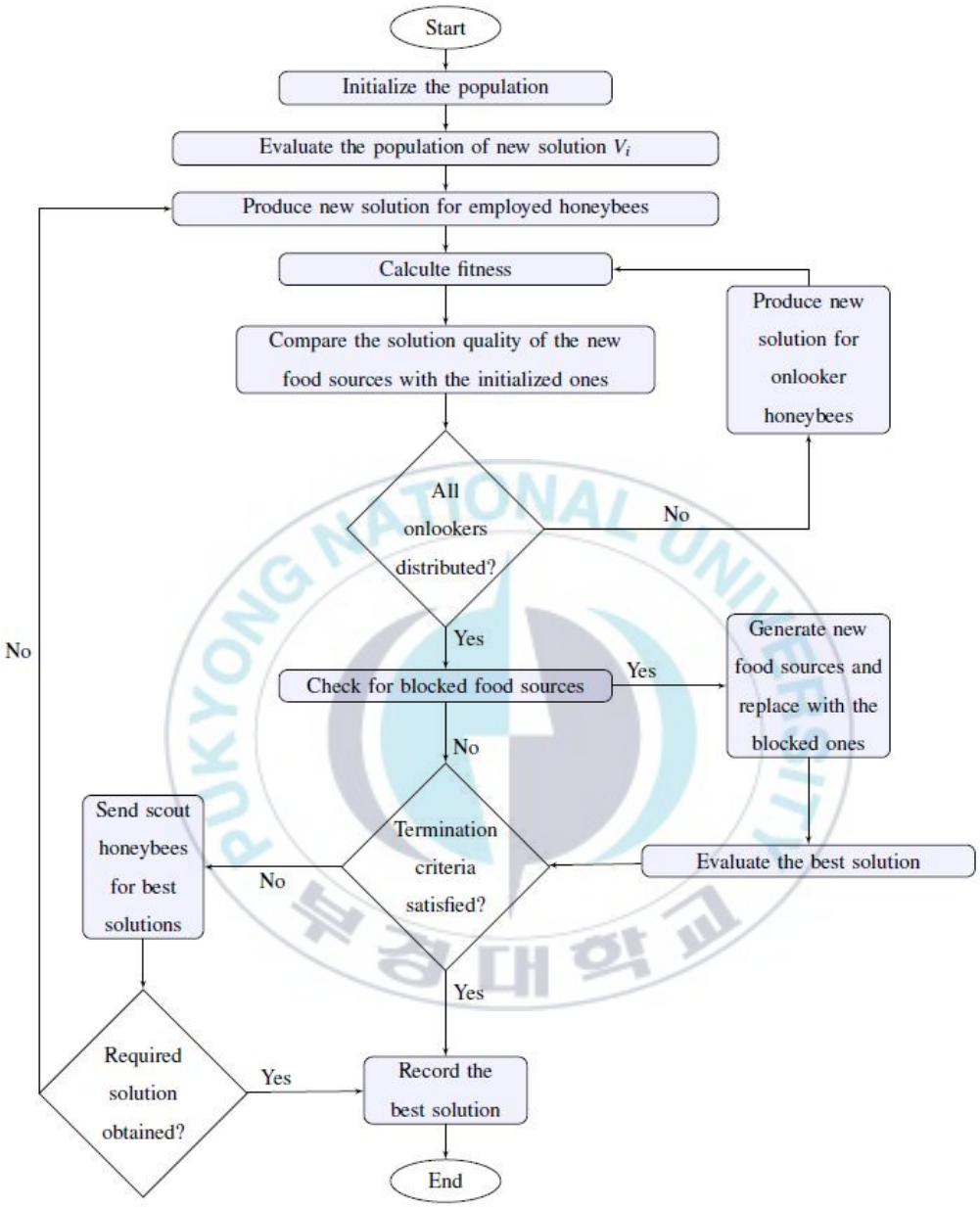

Figure 3.17 Flowchart depicting the steps for threshold optimization in ABC-based optical spectrum sensing.

### 3.4.3 Results and Discussions

The comparative ROC analysis of the proposed ABC-based optical spectrum sensing is presented in Figure 3.18. The colony size is set to 50. The number of samples $N_s$ is set to 7000 and the correlation coefficient is set to $\rho = 0.4$. This performance improvement in the proposed ABC-EVD based technique against the EVD based spectrum sensing can be attributed to the fact that the EVD based spectrum sensing has no optimal $L$ value. It can also be observed that the improvement is salient, particularly in a region of low SNR.

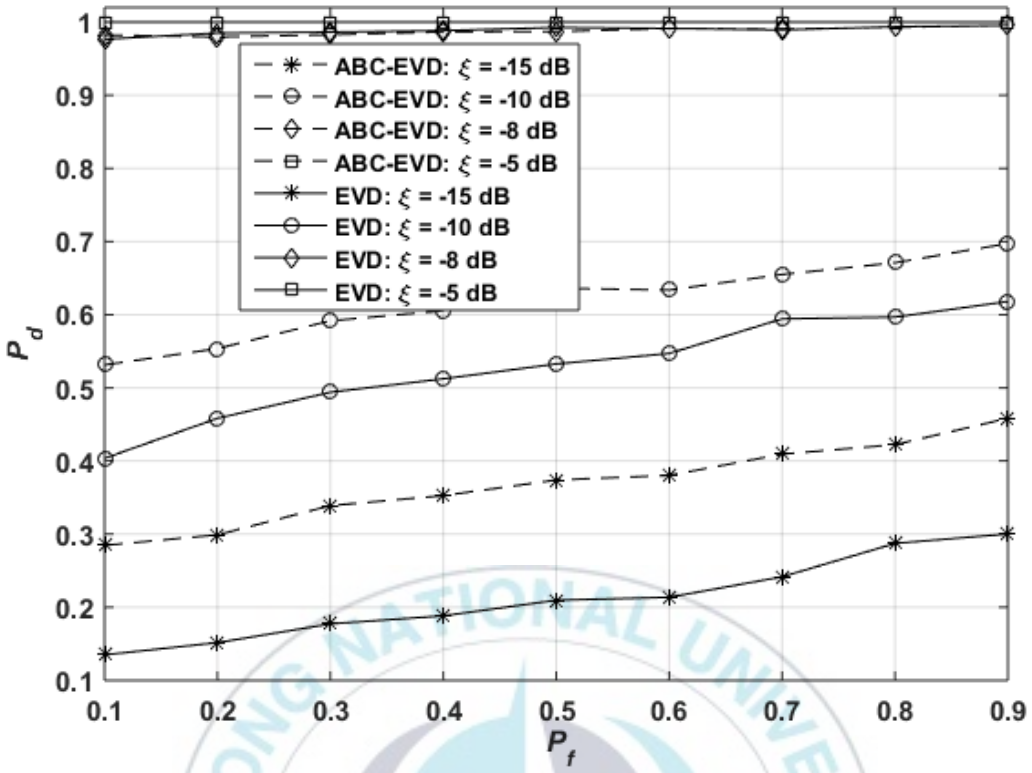


Figure 3.18 Comparative ROC analysis of the proposed ABC-EVD optical spectrum sensing.

Figure 3.19 shows the comparison of the proposed ABC-EVD with the EVD and ED-based optical spectrum sensing in terms of the noise uncertainty $\delta$. The number of samples $N_s$ is set to 7000. In the present simulations, we consider different levels of noise uncertainty. The results demonstrate that the proposed framework can work at any noise uncertainty level and can perform spectrum sensing better than all other techniques considered.

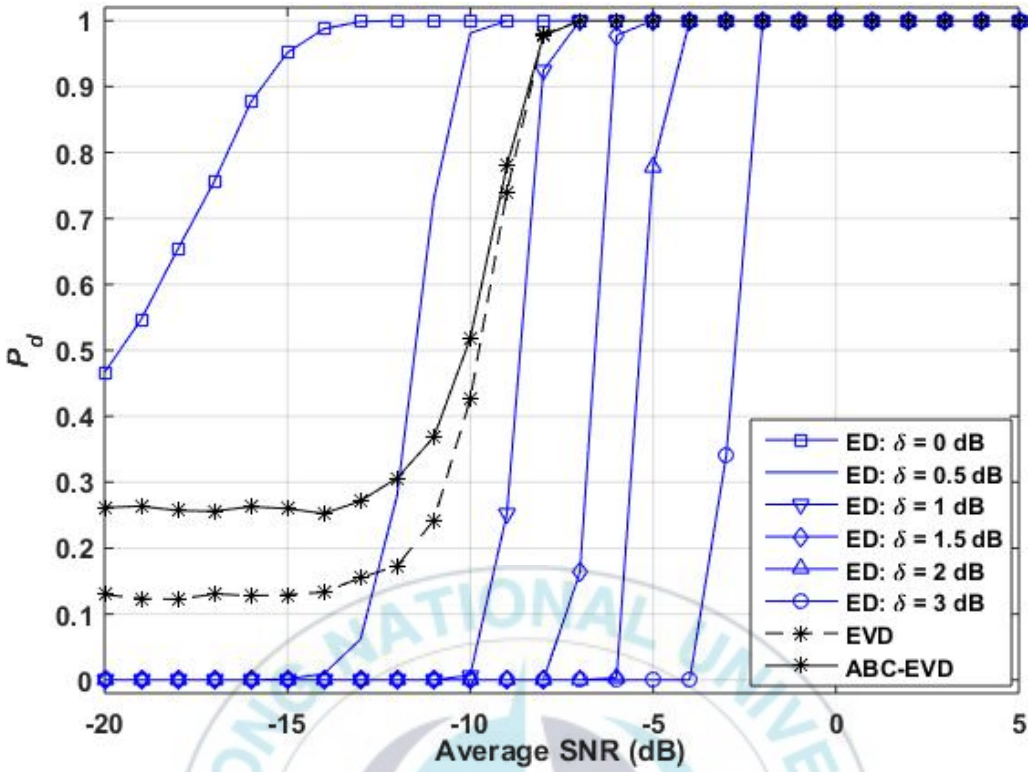


Figure 3.19 Performance comparison of the proposed ABC-EVD spectrum sensing with the EVD and ED-based spectrum sensing.

Taking into consideration different atmospheric turbulence strengths, i.e., $C_n^2 = 8.4 \times 10^{-15}\ \mathrm{m}^{-\frac{2}{3}}$, $C_n^2 = 1.7 \times 10^{-14}\ \mathrm{m}^{-\frac{2}{3}}$, and $C_n^2 = 5.0 \times 10^{-14}\ \mathrm{m}^{-\frac{2}{3}}$ for weak, moderate, and strong turbulence fadings, respectively, Figure 3.20 depicts the performance of the proposed technique. The number of samples $N_s$ is set to 7000. It can be observed that the turbulence strength affects the system's reliability.

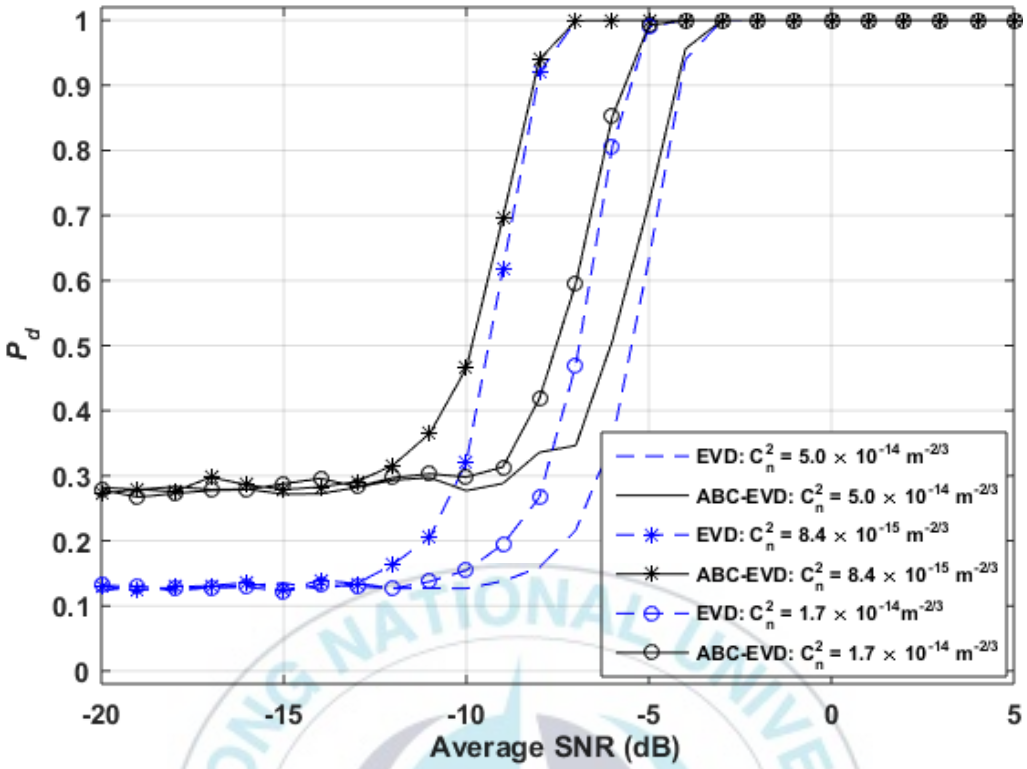


Figure 3.20 Probability of detection against the average received SNR for a different level of correlations.

# 4 Artificial Neural Network Assisted Optical Scattering Communications

Artificial neural network (ANN) and artificial intelligence (AI) are immense engineering disciplines that enable finding solutions to problems by imitating complex processes and systems as learning and decision-making with self rectification. In the recent past, there has been increasing research interest in exploiting AI and ANN tools in finding the solutions to the problems encountered in RF-based wireless communications. Recent examples of utilizing AI or ANN tools to RF communication systems include ANN-assisted automatic modulation classifications, tracking of the carrier phase, channel estimation, and mitigation of the nonlinearity. By utilizing support vector machine and ANN, an RF channel estimation technique based on one-bit relay clustering was reported [55]. A real-time deep-learning-based data detection technique was presented [56]. It avoids the requirement of the channel state information.

Recently, a deep learning framework for OWC was presented [57]. In this work, to overcome the channel impairments, a convolutional autoencoder structure, based on unsupervised learning, was proposed for image sensor communication systems. The transmitter section was constructed with spatially separated LED arrays, and the receiver unit was implemented with an optical image sensor. In another recent work with a similar approach, an autoencoder

with an unsupervised deep learning technique was proposed for a VLC link [58]. It was demonstrated that the transmission error was significantly reduced.

## 4.1 ANN Assisted Signal Classification Algorithm

### 4.1.1 Parameters Estimation for Log-normal Distributed Turbulence Channel

The marginal PDF of the received irradiance over log-normal distributed turbulence channel can be expressed as

$$f_{I_R}\left(I_R\right)=\exp\left\{-\frac{\left[\log\left(I_R\right)+\mu_{NLOS}\right]^2}{\sqrt{2\pi\sigma_{NLOS}^2}I_R}\right\}, \tag{4.1}$$

where $\sigma_{NLOS}^2=1.23C_n^2k^{7/6}\left(d_{tv}^{11/6}+d_{vr}^{11/6}\right)$ and $\mu_{NLOS}$ denotes the shape parameters of the log-normal distribution. Utilizing Equation (4.1), the PDF of the average signal count $y$ can be derived as

$$f_Y\left(y\right)=\frac{\exp\left\{-\frac{\left[\log y+\mu_{nlos}-\log\left(\frac{\hat{H}RP_sT_ss}{hf}\right)\right]}{2\sigma_{nlos}^2}\right\}}{\sqrt{2\pi\sigma_{nlos}^2}y}. \tag{4.2}$$

An important observation is inferred from Equation (4.2) that the PDF of the received count is also obeyed log-normal distribution. It yields

$$Y \sim \log-\text{normal}\left(\mu_{NLOS} - \log\left(\frac{\hat{H}RP_sT_ss}{hf}\right), \sigma^2_{NLOS}\right). \tag{4.3}$$

The $k$th moment of the received signal can then be written as

$$m_k = E\left[y^k\right] = \exp\left\{k\left[\mu_{nlos} - \log\left(\frac{\hat{H}RP_sT_ss}{hf}\right)\right] + k^2\frac{\sigma^2_{nlos}}{2}\right\}. \tag{4.4}$$

Successively solving for $k = 1$ and $k = 2$, the estimates of $\sigma^2_{NLOS}$ and $\mu_{NLOS}$, defined as $\widehat{\mu_{NLOS}}$ and $\widehat{\sigma^2_{NLOS}}$, respectively, are obtained as

$$\hat{\mu}_{nlos} = \log\left[\frac{\left(\sum_{j=1}^{N} y_j\right)^2 \hat{H}RP_sT_ss}{N^{3/2}hf\sqrt{\sum_{j=1}^{N} y_j^2}}\right], \tag{4.5}$$

and

$$\hat{\sigma}_{nlos} = \log\left[\frac{N\left(\sum_{j=1}^{N} y_j^2\right)}{\left(\sum_{j=1}^{N} y_j\right)^2}\right]. \tag{4.6}$$

### 4.1.2 Parameters Estimation for Gamma-Gamma Distributed Turbulence Channel

The Gamma-Gamma distributed optical turbulence channel is based on the modulation process where the fluctuations in the irradiance are derived from

the product of the large-scale and small-scale irradiance fluctuations, with each obeys the Gamma distribution. The Gamma-Gamma distributed turbulence model is valid across all turbulence regimes, that is, from weak-to-mid-to-strong turbulence regimes. The marginal PDF of the received irradiance over a single-scattered NLOS UV link is obtained as

$$f_{I_R}(I_R) = \frac{(\alpha_V \beta_V)(\alpha_R \beta_R)^{\left(\frac{\alpha_R+\beta_R}{2}\right)}}{\Gamma(\alpha_V)\Gamma(\beta_V)\Gamma(\alpha_R)\Gamma(\beta_R)} \times I_R^{\left(\frac{\alpha_R+\beta_R}{2}-1\right)} G_{0,2}^{2,0}\left[\alpha_R \beta_R I_R \middle| \begin{matrix} - \\ \frac{\alpha_R+\beta_R}{2}, -\frac{\alpha_R-\beta_R}{2} \end{matrix}\right] \tag{4.7}$$

where $\alpha_V$ and $\beta_V$ are the model parameters for the path from the transmitter to the common volume and the parameters $\alpha_R$ and $\beta_R$ correspond to the path from the common volume to the receiver. These model parameters are directly related to the underlying optical channel conditions and are given by

$$\alpha_{R(V)} = \left[\exp\left(\frac{0.49\delta_{R(V)}^2}{\left(1+1.11\delta_{R(V)}^{12/5}\right)^{7/6}}\right)-1\right]^{-1}, \tag{4.8}$$

and

$$\beta_{R(V)} = \left[\exp\left(\frac{0.51\delta_{R(V)}^2}{\left(1+0.69\delta_{R(V)}^{12/5}\right)^{5/6}}\right)-1\right]^{-1}, \tag{4.9}$$

where $\delta_{R(V)}^2 = 1.23C_n^2 k^{7/6} d_{vr(tv)}^{11/6}$ represents the log-irradiance variance.

Following Equation (4.7), the distribution of the received signal count can be derived as

$$f_Y(y) = \left(\frac{hf}{\hat{H}RP_sT_s s}\right)^{\left(\frac{\alpha_R+\beta_R}{2}\right)} \frac{(\alpha_V\beta_V)(\alpha_R\beta_R)^{\left(\frac{\alpha_R+\beta_R}{2}\right)}}{\Gamma(\alpha_V)\Gamma(\beta_V)\Gamma(\alpha_R)\Gamma(\beta_R)} \times y^{\left(\frac{\alpha_R+\beta_R}{2}-1\right)} G_{0,2}^{2,0}\left[\frac{hf\alpha_R\beta_R}{\hat{H}RP_sT_s s} y \middle| \begin{matrix} - \\ \frac{\alpha_R-\beta_R}{2}, -\frac{\alpha_R-\beta_R}{2} \end{matrix}\right] . \quad (4.10)$$

Using the definition of the *k*th moment,

$$m_k = E\left[y^k\right] = \int_0^\infty y^k f_Y(y)\,dy , \quad (4.11)$$

we derive the closed-form expression for $m_k$ as follows

$$m_k = \frac{(\alpha_V\beta_V)\Gamma(K+\alpha_R)\Gamma(K+\beta_R)}{\Gamma(\alpha_V)\Gamma(\beta_V)\Gamma(\alpha_R)\Gamma(\beta_R)} \left(\frac{RHP_sT_s s}{hf}\right)^k \left(\frac{1}{\alpha_R\beta_R}\right)^k . \quad (4.12)$$

Utilizing Equation (4.12), we form a nonlinear quadratic equation set with roots $\alpha_R$ and $\beta_R$ as follows

$$\begin{cases} \dfrac{1}{\alpha_R}+\dfrac{1}{\beta_R}=c_R\left(\dfrac{RHP_sT_ss}{hf}\right) \\ \dfrac{1}{\alpha_R\beta_R}=d_R\left(\dfrac{RHP_sT_ss}{hf}\right) \end{cases}, \tag{4.13}$$

where $c_R$ and $d_R$ are estimated from the samples of the noisy signal received at the detector

$$\hat{c}_R=\frac{k^2\dfrac{1}{N}\sum_{j=1}^{N}y_j^2-\dfrac{\sum_{j=1}^{N}y_j^{k+1}}{\sum_{j=1}^{N}y_j^k}-\left(k^2-1\right)}{k\left(k-1\right)}, \tag{4.14}$$

and

$$\hat{d}_R=\frac{k\dfrac{1}{N}\sum_{j=1}^{N}y_j^2-\dfrac{\sum_{j=1}^{N}y_j^{k+1}}{\sum_{j=1}^{N}y_j^k}-\left(k-1\right)}{k\left(1-k\right)}. \tag{4.15}$$

Solving Equations (4.13), (4.14), and (4.15), the estimates of the model parameters $\alpha_R$ and $\beta_R$ are obtained as

$$\hat{\alpha}_R=\frac{\hat{c}_R}{2\hat{d}_R}-\frac{1}{2}\sqrt{\frac{c_R^2}{d_R^2}-\frac{4hf}{\hat{d}_R\hat{H}RP_sT_ss}}, \tag{4.16}$$

and

$$\hat{\beta}_R = \frac{\hat{c}_R}{2\hat{d}_R} + \frac{1}{2}\sqrt{\frac{c_R^2}{d_R^2} - \frac{4hf}{d_R \hat{H} R P_s T_s s}}, \tag{4.17}$$

where $\hat{H}$ is the estimated DC channel gain.

### 4.1.3 System Model

The system model is illustrated in Figure 4.1.

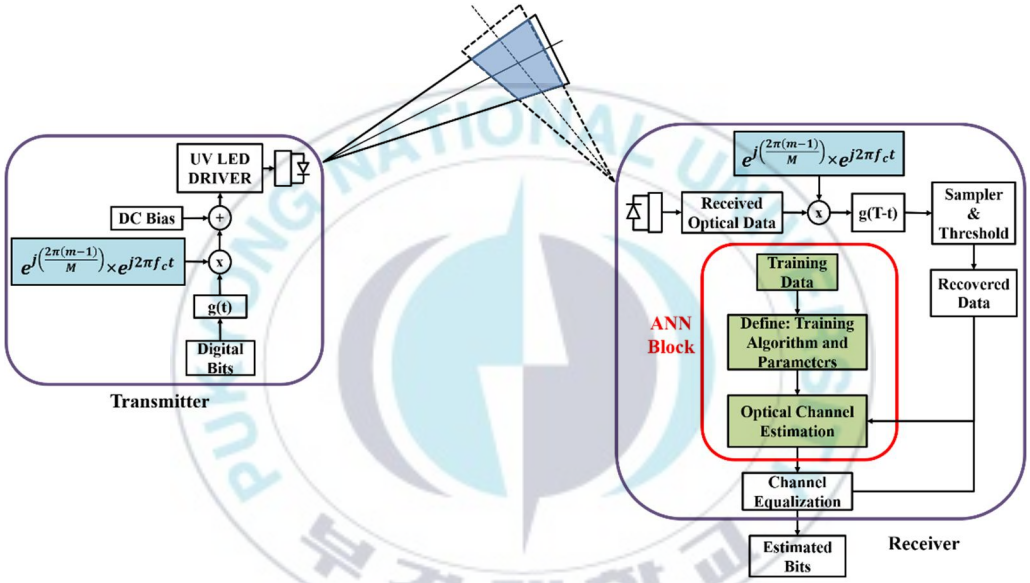


Figure 4.1 System model.

The artificial neural networks (ANNs) consist of neurons, which sum up incoming signals and apply an activation function, and connections, to amplify or inhibit passing signals. We use the nonlinear activation function, that is, the

hyperbolic tangent, to design an ANN-based noisy BPSK subcarrier intensity modulated signal estimator.

### 4.1.4 Results and Analysis

Figure 4.2 depicts the impact of turbulence strength on the classification performance of the proposed ANN-based algorithm. For analysis, we consider 400 noisy data samples transmitted over the Gamma-Gamma distributed turbulence-induced fading. For brevity, we set $\{\alpha_V, \beta_V\} = \{\alpha_R, \beta_R\}$. The transmit power budget is set to $1\ mW$. The green color circles signify the correct or true data classification. The symbol $X$ denotes the incorrect classification. It is interesting to note that, under weak and moderate turbulence fading, the correct classification is as high as 98%; however, as the turbulence strength increases, an error floor is formed with a true classification percentage reducing to 97%. This can be attributed to the fact that in the BPSK subcarrier intensity modulated system, there is an unavoidable synchronization problem, particularly in the presence of strong turbulence fading.

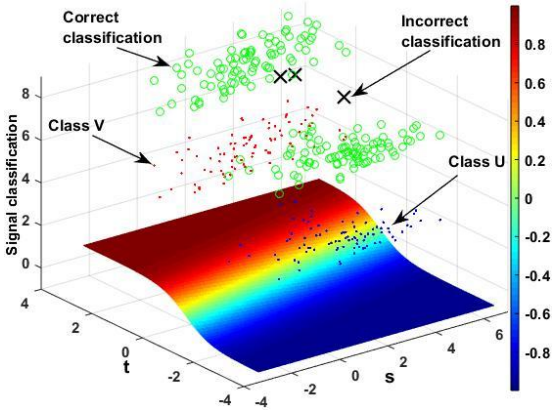


(a) Signal classification under weak turbulence

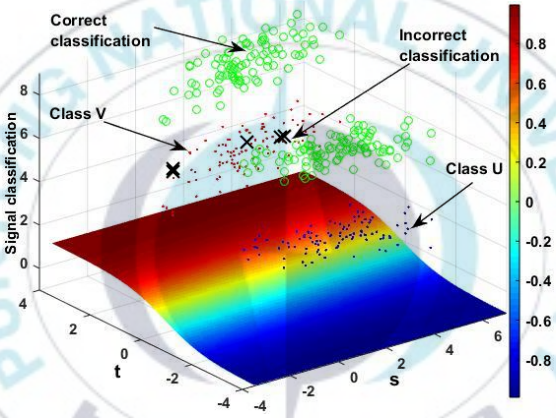


(b) Signal classification under strong turbulence

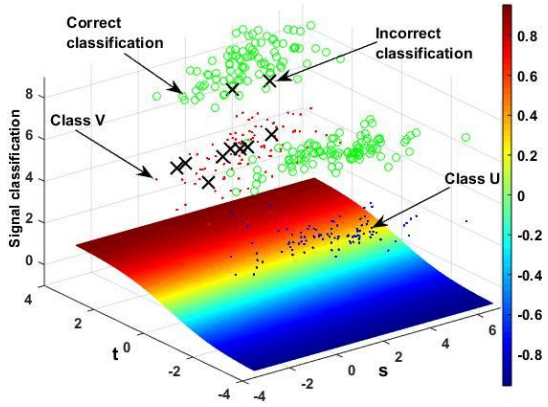


(c) Signal classification under strong turbulence

Figure 4.2 Classification of the noisy BPSK subcarrier intensity modulated received signal over Gamma-Gamma distributed turbulence channels.

Figure 4.3 illustrates the performance of the estimation algorithm for the model parameter of the log-normal fading over the NLOS UV link. As a representative of a typical optical wireless propagation over free-space, we consider the effect of the inner scale $L_0$ set equal to $0.5R_F$, where $R_F$ denotes the scale size of the Fresnel zone. The curves demonstrate an excellent estimation performance.

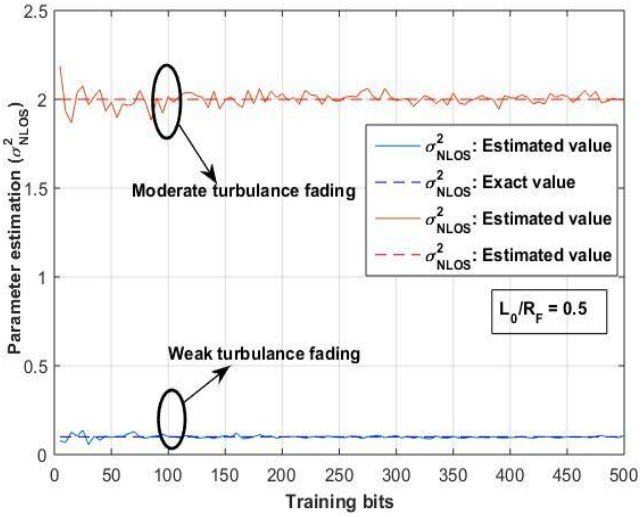


(a) Estimation of the parameter $\sigma_R^2$.

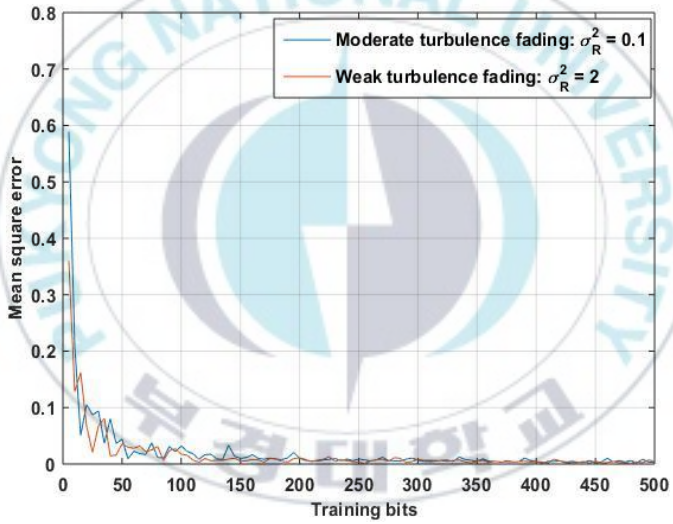


(b) MSE relative to the training size.

Figure 4.3 Estimation of the parameter of the log-normal distributed turbulence fading.

In Figure 4.4, we investigate the estimation performance of the proposed algorithm for Gamma-Gamma distributed fading over the NLOS UV link. For completeness, we consider all turbulence regimes. For brevity, we set $L_0 = 0.5R_F$. The Roytov variance is set to 0.1, 2, and 25, corresponding to the weak, moderate, and strong atmospheric scintillation, respectively. As illustrated in the results, the model parameters $\widehat{\alpha_R}$ and $\widehat{\beta_R}$ estimated by utilizing the proposed algorithm provide good estimates over a wide range of turbulence fading. However, from Figure 4.4(d), it can be seen that under strong fading conditions, the MSE can be as large as 1.5 for a sample size less than 50.

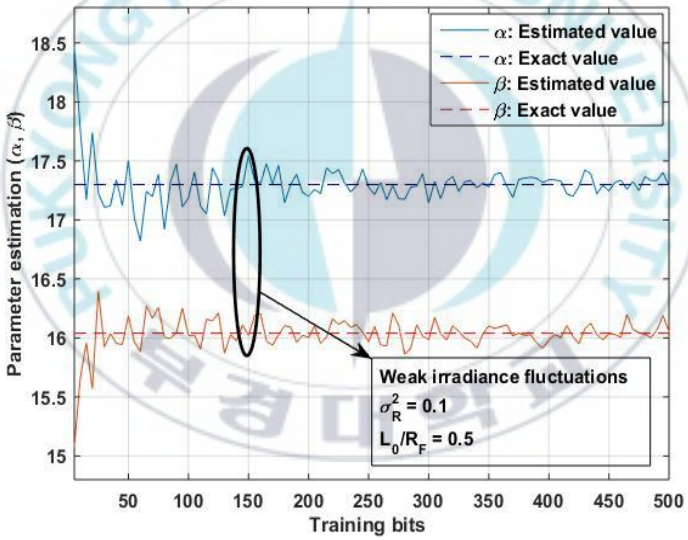


(a) Model parameters estimation: Gamma-Gamma distributed weak turbulence.

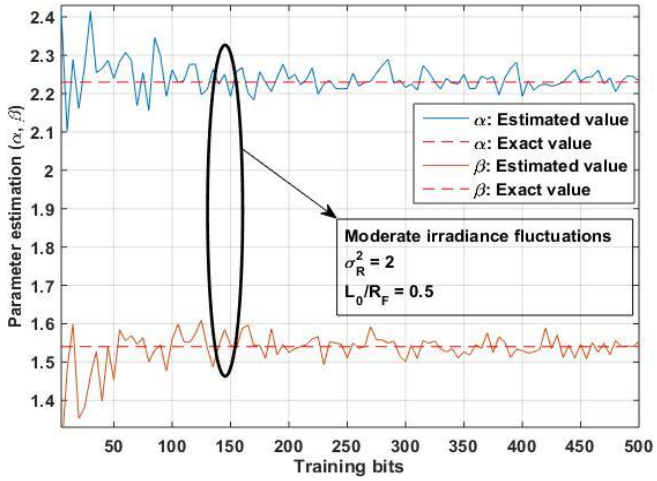


(b) Model parameters estimation: Gamma-Gamma distributed moderate turbulence.

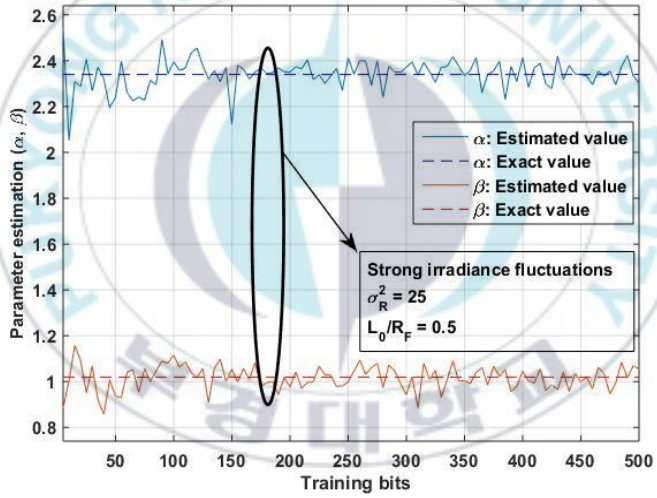


(c) Model parameters estimation: Gamma-Gamma distributed strong turbulence.

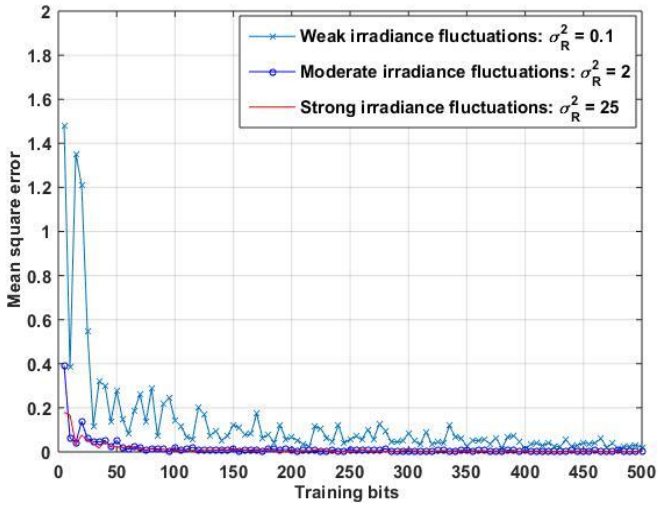


(d) MSE as a function of the training size.

Figure 4.4 Estimation of the model parameters of the Gamma-Gamma distributed turbulence fading

# 5 Indoor Optical Communications

## 5.1 Introduction and Motivation

As a new short-range indoor communication system, a UV-C-based communication system offers several important advantages over VLC and IR. VLC and IR are located near to each other in wavelength, thus exhibiting qualitatively similar behavior. Indoor VLC systems are built based on existing or desired lighting systems; therefore, illumination is an essential function for VLC. For a typical office room, the illumination level should be around 400 lux [59]. Therefore, non-flickering and dimming controllable systems are required. For VLC, the transmitted optical power is equal to the illumination level. Thus, the attempt of achieving a high signal power to interference plus noise ratio (SINR) is an important design criterion, as opposed to the low transmit power required in UV-based indoor systems. Besides, VLC based communication systems have the disadvantage of requiring high-power LEDs to meet the illumination requirement. On the contrary, as there is no requirement to provide illumination in UV-based indoor communication systems, a low-power UV LED can be used as the transmitter. Therefore, it makes the UV-based indoor system more power-efficient, when compared with VLC.

In many infrared-based indoor communication systems, there exist intense ambient infrared noise sources, which include IR from sunlight,

incandescent light source, and fluorescent light source. These are the primary sources of ambient noise at the infrared receiver. Like VLC, infrared systems also require relatively high transmit power. For a power-efficient system, a low power operation is another important factor in indoor communications. Optical power utilized to transmit the information bit decides the efficiency of the optical transmitter. Since the UV-C region is solar blind, the background noise is virtually zero [60], when compared with VLC and IR. Therefore, for UV-C-based indoor communication systems where the internal receiver noise is very low and the photon-counting receiver can be employed, the transmit power or the source power can be minimized for the target data rate [6]. Moreover, it is generally described that IR supports a lower data rate and a lower range of communication.

Motivated by the unique advantages of the UV-based communication systems, the primary purpose of this chapter is to present first of its kind UV-based indoor optical communication systems. First, we present the channel modeling for state-of-the-art UV-based indoor communication. In addition, the time delay statistics of indoor Poisson channels are also presented. Next, we present novel multiuser indoor communication over a power-constrained Poisson channel. We develop a minimum mean square error (MMSE) receiver to reject the interference caused by multiple users. Moreover, a solution to the

downlink beamforming optimization problem is presented based on the second-order cone programming. A more detailed treatment on UV-based indoor Poisson channel can be found in the related literature [59, 61, 62].

A few potential advantages of the proposed UV-based indoor optical communication system over VLC and IR-based systems are listed in Table 5.1.

Table 5.1 Potential Advantages of the Proposed UV-based Indoor Optical Communication Systems over VLC and IR-based Indoor Systems.

| | **UV** | **VLC** | **RF** |
|---|---|---|---|
| Illumination | Not required | An essential requirement | Not required |
| Non-flickering and dimming control systems | Not required | An essential requirement | Not required |
| Background noise | Virtually zero [60] | High | High |
| Transmit power requirement | Low | High because of illumination | Moderate |
| Data rate | Can support a high data rate for the given transmit power because of low background noise | High background noise is a limiting factor in achieving a high data rate for the given transmit power | High background noise is a limiting factor in achieving a high data rate for the given transmit power |

## 5.2 UV Safety Exposure Limit for Indoor Communications

The intensity of the radiations from the UV source is measured in the unit of milliwatts per square centimeter ($mW/cm^2$) or in the unit of millijoules per square centimeter ($mJ/cm^2$). The level of UV radiation a human can receive on their eyes and skin for a given time duration varies with the wavelength of the UV radiation.

The International Commission on Non-Ionizing Radiation Protection [9] and the International Electrotechnical Commission [10] govern UV radiation exposure power limits. In the UV-C band, the allowable continuous exposure limits at 200 nm, 270 nm, and 280 nm are 100, 3, and 3.4 mJ per $cm^2$ for an eight-hour exposure, respectively. Therefore, the minimum allowable continuous exposure occurs at 270 nm. In addition, as reported in [5, 11], for continuous UV exposure, the maximum allowable UV power limit is 0.1 $\mu W$ per $cm^2$, and for the UV exposure less than 7 hours, it is 0.5 $\mu W$ per $cm^2$. As defined by this standard, exposure below these limits is considered to be safe for humans. These are important safety considerations that a UV-based communication system design should follow.

## 5.3 Signal Model

Various possible UV link geometries are shown in Figures 5.1 and 5.2. We denote the length, breadth, and height of the room as *L, B,* and *H* respectively. As the receiver, we employ a photon-counting receiver. $\theta_s$ represents the scattering angle. $d$ is the baseline distance between the transmitter and the photon-counting receiver for the NLOS scattered link geometry. In order to satisfy the UV exposure limits, the transmitted signal is considered to be weak. Therefore, unlike the conventional outdoor UV link where there is no transmit power limitation, the week indoor UV signal cannot be detected or observed by the conventional continuous waveform detector, such as an avalanche photodiode. Instead, a photon-counting receiver must be employed.

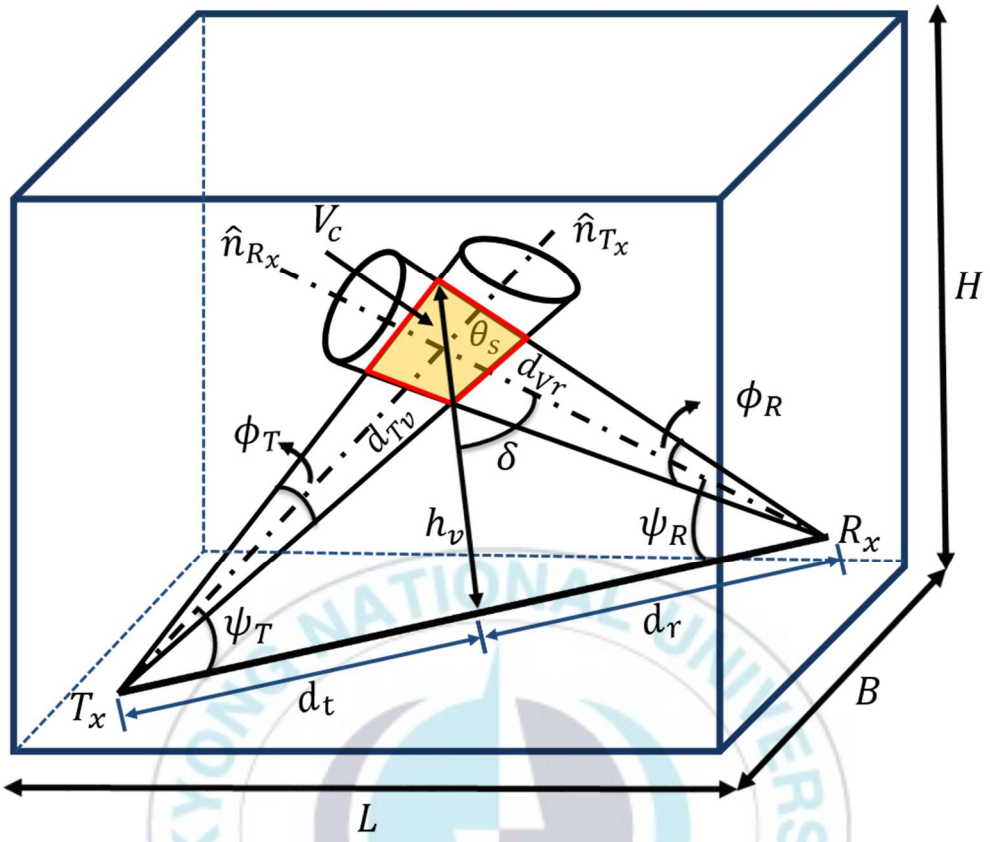


Figure 5.1 NLOS UV link geometry that corresponds to the received signal characterized by a single-scattering event.

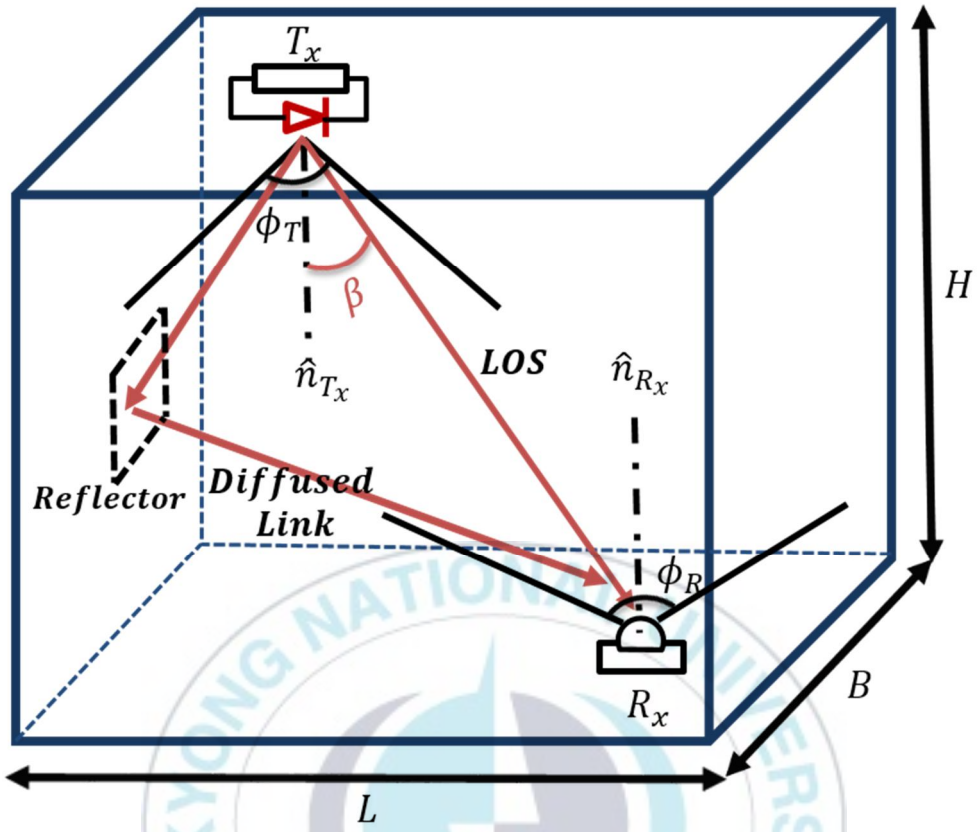


Figure 5.2 UV link geometry that corresponds to the LOS link and diffused component.

To obey the UV safety exposure limits and to maintain the UV radiation under allowable exposure limits, we consider a low-power transmit regime. We impose strict average and peak power constraints on the total transmit power budget.

**Constraint 1:** *The average power constraint:*

$$E[P_t] \leq P_{t,avg} \ , \tag{5.1}$$

where $E[\cdot]$ represents the expectation operation.

**Constraint 2:** *The peak power constraint:*

$$P_t \leq P_{t,max} \ , \tag{5.2}$$

where $P_{t,max}$ represents the maximum allowable transmit power.

Equations (5.1) and (5.2) are sufficient and necessary conditions to ensure that the UV radiation follows the allowable safety exposure limits. It yields

$$\begin{cases} \mathrm{P}_{\mathrm{rob}}\left(E\left[P_t\right] > P_{t,\mathrm{avg}}\right) = 0, & \text{and} \\ \mathrm{P}_{\mathrm{rob}}\left(P_t > P_{t,\mathrm{max}}\right) = 0 \end{cases}, \tag{5.3}$$

where $\mathrm{P}_{\mathrm{rob}}(\cdot)$ denotes the probability.

In order to characterize the proposed system model, we utilize the channel model developed in [59] to predict the received signal at the photodetector. We consider an on-off keying (OOK) modulation scheme. Let $x(t)$ denote the OOK modulated transmit symbol. The received signal can then be modeled as [36]

$$y(t) = \sqrt{P_t}\sum_{i=0}^{L} h_i x\left(t - iT_s\right) + w(t) \ , \tag{5.4}$$

where $T_s$ denotes the symbol duration and $w(t)$ represents the background radiation intensity. The energy of the received signal component within the symbol duration is given by

$$E_s = P_t \int_0^{T_s} \left| \sum_{i=0}^{L} h_i x\left(t - iT_s\right) \right|^2 dt \quad . \tag{5.5}$$

At the output of the photon-counting receiver, the received optical signal is represented by a number of photons. A practical model for the number of received photons, denoted as $N_p$, in a low-power regime of the optical communication, is the discrete-time Poisson distribution and is modeled as [34, 37]

$$\mathrm{P}_{\mathrm{rob}}\left(N_p = j \middle| \lambda_s\right) = \frac{\left(\lambda_s + \lambda_b\right)^j}{j!} e^{-(\lambda_s + \lambda_b)}, j \in \square_0^+, \tag{5.6}$$

where $\lambda_s$ denotes the photon arrival rate for the signal component and is given by the ratio $\frac{E_s}{E_p}$, where $E_p$ represents the energy per photon determined by the wavelength of the UV laser employed. $\lambda_b$ is the background radiation photon count rate [36].

Analogous to Constraints defined in Equations (5.1) and (5.2), it can readily be shown that

$$E[\lambda_s] \le \lambda_{s,\text{avg}} = \frac{\lambda \eta_{qe} P_{t,\text{avg}} H(0)}{R_b hc}, \tag{5.7}$$

and

$$\lambda_s \le \lambda_{s,\max} = \frac{\lambda \eta_{qe} P_{t,\max} H(0)}{R_b hc} \quad , \tag{5.8}$$

where $\eta_{qe}$ is the quantum efficiency of the photon-counting receiver, $h$ is the Plank's constant, and $c$ represents the speed of light. $\lambda$ is the UV wavelength and $R_b$ denotes the bit rate.

### 5.3.1 Necessary Conditions for the IM/DD OOK Modulated Signal

In this section, we derive the necessary condition for the IM/DD modulated scheme to satisfy Constraints 1 and 2. Consider a unipolar OOK modulation, the distribution of $\lambda_s$ can be written as

$$\lambda_s = \begin{cases} 0; & \text{with probability } (p) \\ \Upsilon; & \text{with probability } (1-p) \end{cases}, \tag{5.9}$$

where $\Upsilon = \frac{E_s}{E_p} > 0$ and $p \in (0,1)$. The parameters $\Upsilon$ and $p$ must be chosen such that the Constraints defined in Equation (5.1) and (5.2) should be satisfied. We consider a background radiation photon count rate proportional to $\lambda_{s,avg}$,

such that for any constant $A > 0$, $\lambda_b = A\,\lambda_{s,avg}$. With $\Upsilon \in (0, \lambda_{s,max}]$ and $p$ set to $1 - \frac{\lambda_{s,avg}}{\Upsilon}$, the distribution in Equation (5.3) satisfies Constraints 1 and 2.

### 5.3.2 Signal-to-Noise Ratio in Poisson Channel

In characterizing the indoor UV channel as a discrete-time Poisson channel, we define the signal-to-noise ratio (SNR) as the ratio of the square of the expected mean of the count parameter due to the information-bearing signal to the total variance of the received signal [38, 39] as

$$\chi = \frac{\left(E[\lambda_s]\right)^2}{2E[\lambda_s] + 4\lambda_b}, \tag{5.10}$$

which can readily be obtained as

$$\chi = \frac{\lambda \eta_{qe} T_s P_{t,\text{avg}}^2 H^2(0)}{2hc\left(P_{t,\text{avg}} H(0) + 2P_b\right)}. \tag{5.11}$$

### 5.3.3 Derivation of BER Satisfying the Constraints

Assuming the OOK modulation with threshold-based direct detection, the bit error rate is given by [40, 41]

$$P_e = \frac{1}{2}\sum_{j=0}^{\lambda_{Th}} \frac{\left(\lambda_s + \lambda_b\right)^j e^{-(\lambda_s+\lambda_b)}}{j!} + \frac{1}{2}\sum_{j=\lambda_{Th}+1}^{\infty} \frac{\left(\lambda_b\right)^j e^{-\lambda_b}}{j!}, \tag{5.12}$$

where $\lambda_{Th}$ denotes the optimal threshold value given by

$$\lambda_{Th} = \left\lfloor \frac{\lambda_s}{\ln\left(1+\frac{\lambda_s}{\lambda_b}\right)} \right\rfloor. \tag{5.13}$$

Considering the Constraints 1 and 2 on the transmit power, the lower bound on the bit error rate for equally likely OOK transmission can be represented as Equation (5.14).

$$P_{e,OOK} \geq \frac{1}{2}\sum_{j=0}^{\lambda_{Th}} \frac{\left(\lambda_{s,avg}\right)^j \left(2+A\right)^j e^{-\lambda_{s,avg}(2+A)}}{j!} + \frac{1}{2}\sum_{j=\lambda_{Th}+1}^{\infty} \frac{\left(A\lambda_{s,avg}\right)^j e^{-\lambda_{s,avg}A}}{j!}. \tag{5.14}$$

According to the threshold-based direct detection, the receiver makes the decision for the transmitted bit by comparing the measured number of the received photons $N_p$ with the threshold $\lambda_{Th}$ according to the rule:

$$\hat{x}_n = \begin{cases} 1, & \text{when } N_p > \lambda_{Th} \\ 0, & \text{when } N_p \leq \lambda_{Th} \end{cases}. \tag{5.15}$$

$N_p$ denotes the number of photons counted within the detection space; hence, it is an integer. Using Equation (5.15), the decoding bit probability of error can be formulated as

$$P_e = p\text{Prob}\left[ N_p \geq \lambda_{Th} \middle| x_n = 0 \right] + (1-p)\,\text{Prob}\left[ N_p < \lambda_{Th} \middle| x_n = 0 \right] \qquad (5.16)$$

where $p$, as defined in (27), is *a priori* probability of transmitting symbol zero. Utilizing the Poisson count probability expression obtained in (24) into (29), it yields

$$P_e = p\sum_{j=0}^{\lambda_{Th}} \frac{\left(\lambda_s + \lambda_b\right)^j}{j!} e^{-(\lambda_s+\lambda_b)} + (1-p)\sum_{j=\lambda_{Th}+1}^{\infty} \frac{{\lambda_b}^j}{j!} e^{-\lambda_b} . \qquad (5.17)$$

As can be seen, the error probability depends on the choice of the threshold $\lambda_{Th}$. The optimum value of the detection threshold for minimum $P_e$ can be obtained by utilizing $\frac{dP_e}{d\lambda_{Th}} = 0$. Differentiating Equation (5.17) with respect to $\lambda_{\text{Th}}$ and applying the rule for differentiating summations [24]

$$\frac{d}{d\text{K}}\left\{\sum_{j=0}^{K} f(j)\right\} = f(K) , \qquad (5.18)$$

the general expression for the optimum value of the detection threshold with the probability $p$ for symbol zero is derived as

$$\lambda_{Th} = \left\lfloor \frac{\lambda_s - \log_e\left(\frac{p}{1-p}\right)}{\log_e\left(1+\frac{\lambda_s}{\lambda_b}\right)} \right\rfloor, \tag{5.19}$$

where $\lfloor \cdot \rfloor$ represents the greatest integer floor function.

It should be noted that for an equally likely OOK transmission, i.e., for $p = 0.5$, the expressions obtained in Equations (5.17) and (5.19) will reduce to the expressions obtained in [36, 37].

### 5.3.4 BER Performance Enhancement

Because of the transmit power constraints imposed, the power-efficient pulse-position modulation (PPM) scheme seems to be a more attractive option than OOK modulation for UV-based indoor communications. The average number of the information-bearing photons incident on the detector per second for one PPM symbol is given by [41]

$$\lambda_s = \frac{\lambda \eta_{qe} P_t H(0) \log_2 M}{R_b hc}. \tag{5.20}$$

Let $x_i$ denote the *i*th information-bearing binary input to the discrete-time Poisson channel, corresponding to the *i*th slot of the PPM symbol. $x_i$ equal to 1

represents the transmission of a PPM pulse in the *i*th slot and $x_i$ equal to 0 represents no pulse. Let $y_i$ denote the corresponding output, that is, the number of photons received in the *i*th slot. The average number of information-bearing photons per PPM symbol, $N_s$, is equal to $MT_s\lambda_s$, where $T_s$ denotes the duration of each slot in a PPM symbol. Similarly, the average number of noise photons per PPM symbol, $N_b$, can be obtained as $MT_s\lambda_b$. For the power constraint to be satisfied, we must have

$$N_s \le \frac{\lambda \eta_{qe} P_{t,avg} H(0) M T_s \log_2 M}{R_b hc}. \tag{5.21}$$

We consider a conditionally independent discrete-time Poisson channel with the joint probability of the number of received photons over slots $i$ and $k$ given by

$$f_{Y_i Y_k | X_i X_k}(y_i, y_k | x_i, x_k) = f_{Y_i|X_i}(y_i|x_i) f_{Y_k|X_k}(y_k|x_k), \tag{5.22}$$

where $f_{Yi|X_i}(y_i|x_i)$ denotes the conditional density function of the number of received photons $y_i$, given the binary input $x_i$ over the *i*th slot. Following the discrete-time Poisson channel, $f_{Yi|X_i}(y_i|x_i)$ can then be formulated as

$$f_{Y_i|X_i}(y_i = j | x_i = 0) = \frac{N_b^j}{j!} e^{-N_b}, \tag{5.23}$$

and

$$f_{Y_i|X_i}\left(y_i = j \middle| x_i = 1\right) = \frac{\left(N_s + N_b\right)^j}{j!} e^{-\left(N_s+N_b\right)}. \quad (5.24)$$

Using Equations (5.23) and (5.24), and applying the maximum-likelihood symbol decision with the power constraint, the lower bound on the bit error rate can readily be obtained as given in Equation (5.25) [45]

$$P_{e,PPM} \geq 1 - \sum_{n=0}^{\infty} \left\{ \left(1 + \frac{N_s}{N_b}\right)^n \left[ \left( \sum_{m=0}^{n} \frac{N_b^m}{m!} e^{-N_b} \right)^M - \left( \sum_{m=0}^{n-1} \frac{N_b^m}{m!} e^{-N_b} \right)^M \right] \frac{e^{-N_s}}{M} \right\} \quad (5.25)$$

### 5.3.5 Link Gain Analysis

In this subsection, we investigate the link gain ratio to show the dominance of the directed LOS UV path and the diffused path over the NLOS single-scattered UV link. The transmitted optical power is primarily split into two components. The first component is the directed LOS component, which reaches the detector without reflection and is characterized by the channel impulse response $h^{(0)}(t)$. The second component reaches the detector after one or multiple bounces or reflections and is characterized by $h^{(k)}(t)$. For the considered link geometry, the transmitted signal reaches the photon-counting receiver after scattering and is characterized by the DC link gain $H_{Scat}(0)$. We

denote the link gain ratio $\Gamma$ as the ratio of the power received over two geometries. Mathematically, it can be expressed as

$$\Gamma = \frac{P_r^{\text{LOS}} + P_r^{\text{Diffused}}}{P_r^{\text{Scattered}}} \approx \frac{\int_{-\infty}^{\infty} h^{(0)}(t)dt + \int_{-\infty}^{\infty} \sum_{k=1}^{K} h^{(k)}(t)dt}{H_{\text{Scat}}(0)} . \quad (5.26)$$

In Equation (5.26), $P_r^{LOS}$ and $P_r^{Diffused}$ denote the received power from the directed LOS UV link and the UV link from the diffused reflection, respectively. $P_r^{Scattered}$ is the power of the optical signal that reaches the photon-counting receiver after undergoing a single-scattering event. Generally, the directed LOS UV link is always the strongest; therefore, $\Gamma > 1$. To estimate $P_r^{Diffused}$, we consider the first $K$ bounces only.

### 5.3.6 Results and Discussions

The simulation parameters are illustrated in Table 5.1.

Table 5.2 Simulation parameters.

| Parameter | Value |
|---|---|

| | |
|---|---|
| UV wavelength | 280 nm |
| Room dimensions ($L \times B \times H$) | 5 m × 5 m × 5 m |
| Modulation bandwidth | 20 MHz |
| Area of the PMT | $25 \times 10^{-4}$ cm^2 |
| Responsivity of the PMT | 0.6 A/W |
| Reflection coefficient | 0.7 |

In Figure 5.3, we investigate the link gain ratio as a function of the maximum reflection order *K*. It determines the strength of the directed LOS UV link plus diffused UV link over the NLOS scattered UV link. K = 0 corresponds to a scenario where only directed LOS path exists. It is important to note that as the reflection order K increaes, the more reflected paths reach the PMT and therefore tend to increase the received power from the reflected components significantly.

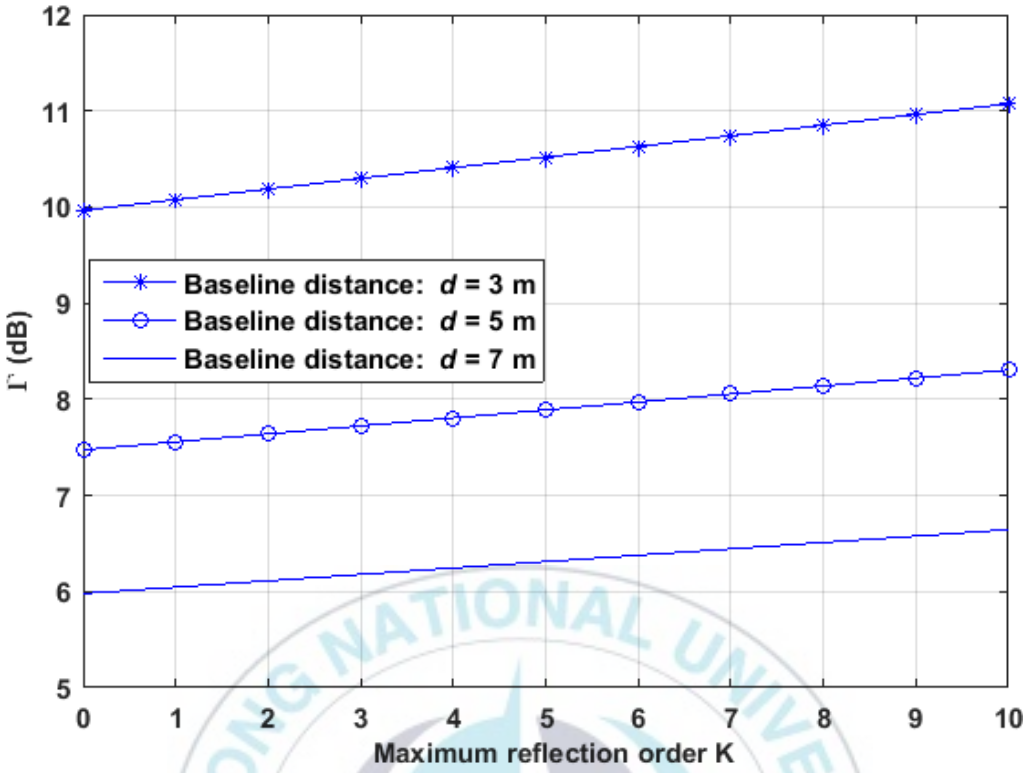


Figure 5.3 Link gain ratio against the maximum reflection order.

The magnitude and the impulse responses of different types of link are shown in Figures 5.4(a) and 5.4(b), respectively. As can be seen, the LOS component carries a significant strength, when compared to the diffused component and the NLOS single-scattered component. Another important observation can be inferred that the diffused component and the NLOS single-scattered component have a significant impact only at low frequencies. The high-frequency response is mainly characterized by the directed LOS component.

Moreover, as depicted, the first peak UV signal arrives from the direct LOS component. It is important to note that the diffused link with K = 2 reaches much earlier than the NLOS single-scattered component. The continuous distribution of the path delays leads to a decrease in the UV channel magnitude response at higher frequencies. From the results, it should be noted that, however, for all the possible components, the impulse response contains significant power for as long as 40 ns, after its first nonzero excursion.

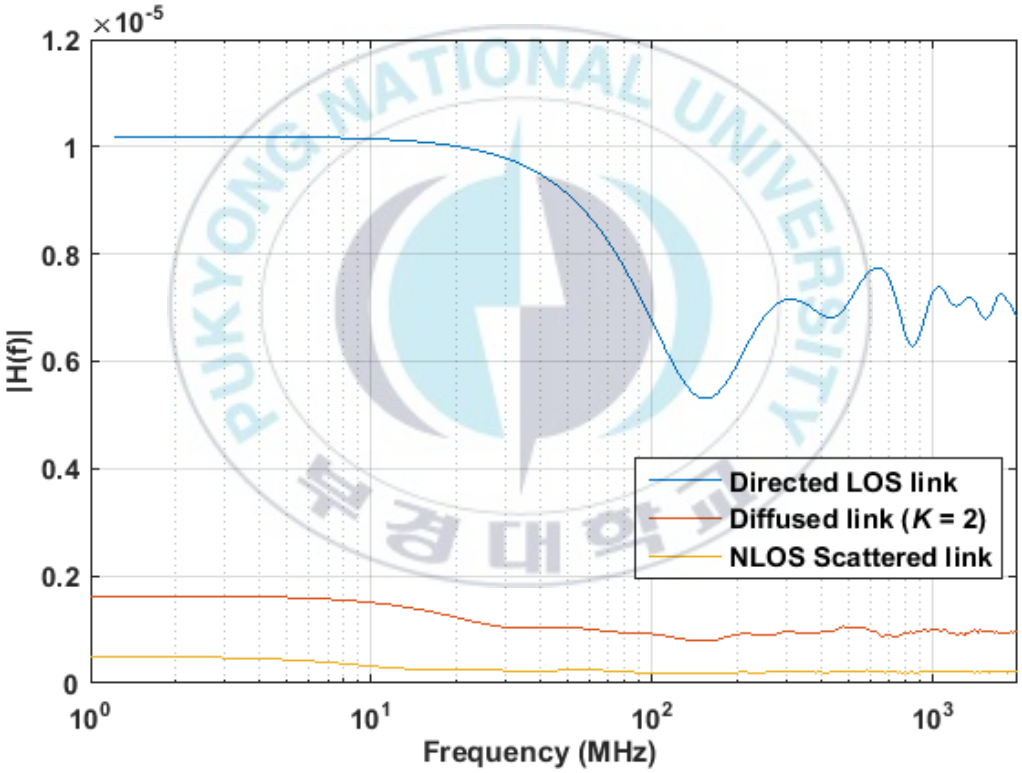

Figure 5.4(a) Magnitude response of the indoor UV channel for different propagation paths.

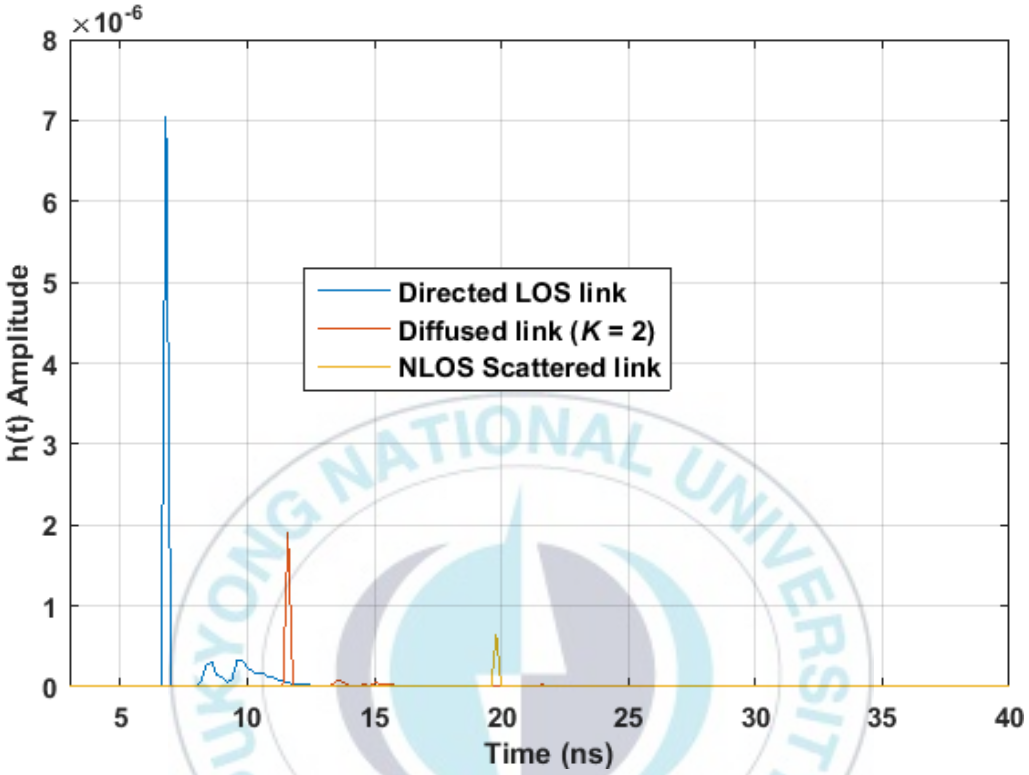


Figure 5.4(b) Impulse response for indoor UV channel for different propagation paths.

Figure 5.4 Magnitude and impulse responses for indoor UV channels for different propagation paths.

In Table 5.2, we list the time dispersion parameters and the received power for possible different types of components.

Table 5.2 Time Dispersion Analysis for Different UV Propagation Paths.

| **Time dispersion parameters (ns)** | **Directed LOS link** | **Diffused link** | **NLOS single-scattered link** |
|---|---|---|---|
| RMS delay spread ($\tau_{rms}$) (ns) | 0.43 | 0.72 | 1.24 |
| Mean excess delay ($\sigma_\tau$) (ns) | 9.23 | 17.81 | 19.1 |
| Received power (nW) ($P_t = 1$ mW) | 69.26 | 9.426 | 5.972 |

The time dispersion parameters including the RMS delay spread and the mean excess delay for different UV propagation paths measured with the truncation length $T_r$ calculated by $T_r = \int_0^{T_r} h(t)dt = 0.97 \int_0^{\infty} h(t)dt$, are listed in Table 5.2. It is shown that the directed LOS UV link whose impulse response is primarily dominated by a short initial pulse, results in the smallest delay spread. The diffused link results in the delay spread that is marginally larger than that of the directed LOS link, due to the finite temporal spread of the dominant reflection from the wall. The RMS delay spread and the mean excess delay of the NLOS single-scattered UV path are larger, when compared with the directed LOS and the diffused component. This can be inferred to the fact that

the UV signal following the NLOS scattered path travels a longer path to reach the photon-counting detector and therefore $\tau_{rms}$ and $\sigma_{\tau}$ increase. Moreover, an important observation is made that the directed LOS path carries 88.02 percent of the total received optical power from the directed LOS and the diffused components, whereas the power carried by the scattered component is 12 times weaker than that of the directed LOS link.

## 5.4 State-of-the-art Multiuser Indoor Communication over Power-Constrained Poisson Channel

This section presents novel UV-based multiuser indoor optical communication over the power-constrained Poisson channel. We develop the system model where the received signal at any user is characterized by a photon-counting receiver. The detector is characterized by MMSE to cancel the interference caused by multiple users. To keep the total transmit power to a minimum and under the allowable UV exposure limits, we develop the convex optimization problem for downlink beamforming using second-order cone programming. In addition, we develop the composite hypothesis based on the maximum likelihood sequence detection (MLSD) with unknown channel state information (CSI). With strict power constraints imposed, the lower bound on the UV channel capacity is obtained. Importantly, we realize the proposed

system experimentally. The impact of the control parameter (average-to-peak power ratio) on the BER is experimentally studied.

### 5.4.1 System Model

The block diagram of the proposed multiuser communication system is illustrated in Figure 5.5. The $i$th LED sends a linear combination of the data for $J$ number of users as

$$s_i(t) = \sum_{j=1}^{J}\left(\sum_{k=1}^{K} b_j c_j[k]\, g(t - kT_c)\right), \tag{5.27}$$

where $b_j$ is the data corresponding to the $j$th user. $\boldsymbol{c_j}$ represents the optical orthogonal code of length $K$ corresponding to the $j$th user. $T_c$ is the chip duration, whereas $g(t)$ represents the rectangular pulse shape.

The signal received at the $j$th user can be expressed as

$$y_j(t) = \sum_{i=1}^{I} h_{ij}\left(\sum_{j=1}^{J}\left(\sum_{k=1}^{K} b_j c_j[k]\, g(t - kT_c)\right)\right) + n_j(t), \tag{5.28}$$

where $h_{ij}$ is the channel impulse response from the $i$th transmitter to the $j$th user. $n_j(t)$ is the shot noise due to background illumination.

### 5.4.2 Receiver Characterization

In this section, we present an MMSE filter represented by $w_j = \left[w_j[1], w_j[2], \cdots, w_j[K]\right]$. The mean-squared error $e_j$ corresponding to the $j$th user is defined as

$$e_j = E_{\mathbf{b},\mathbf{n_j}}\left[\left(y_j - b_j\right)^2\right]. \tag{5.29}$$

Solving for $\frac{de_j}{dw_j} = 0$, the coefficient of the MMSE filter are obtained as shown in Equation (5.30).

$$\mathbf{w}_j = \frac{\left(E\left[\mathbf{n_j}\mathbf{b_j}^T\right] + E\left[\mathbf{b_j}\mathbf{n_j}^T\right] + 2\mathbf{C}^T\mathbf{H_j}^T E\left[\mathbf{b}.b_j\right] + 2\mathbf{C}^T\mathbf{H_j}^T E\left[\mathbf{b}\mathbf{n_j}^T\right] + 2E\left[\mathbf{n_j}^T\mathbf{b}\right]\mathbf{H_j}\mathbf{C}\right)}{\left(\mathbf{C}^T\mathbf{H_j}^T E\left[\mathbf{b}^T\mathbf{b}\right]\mathbf{H_j}\mathbf{C} + \sigma_n^2\mathbf{I}\right)}, \tag{5.30}$$

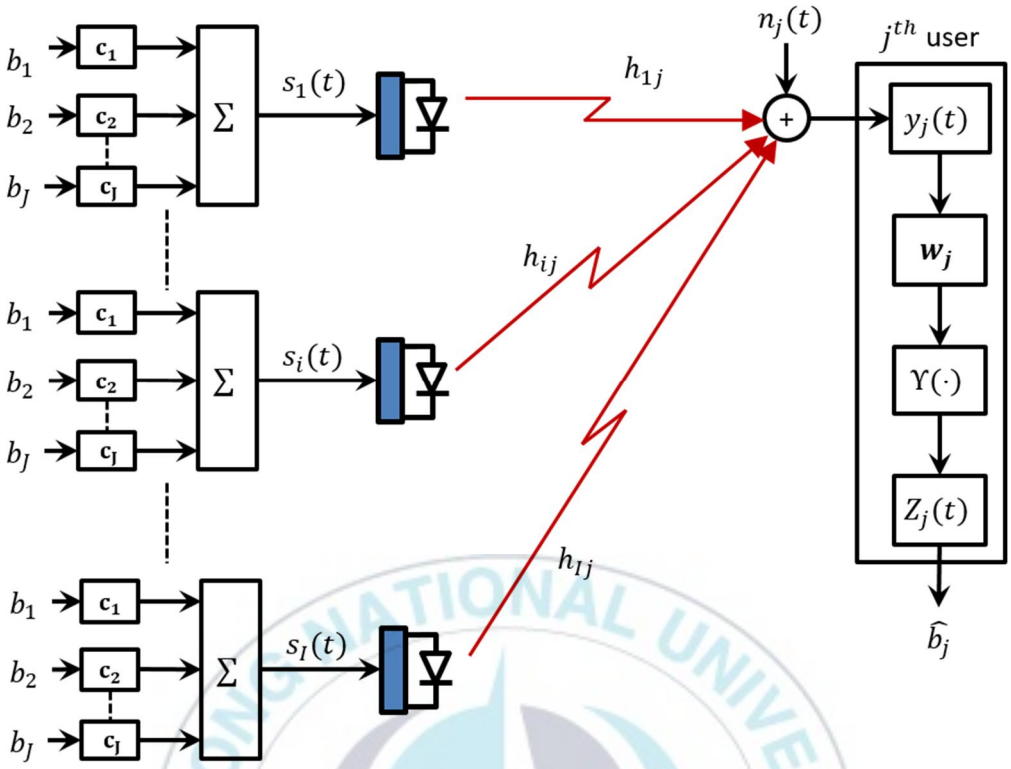


Figure 5.5 UV-based multiuser indoor communication over power-constrained Poisson channel.

### 5.4.3 Low-power Transmission Regime

The input-output relationship for the $j$th user can be formulated as

$$Z_j(t) = \Upsilon\left\{\sum_{i=1}^{I} h_{ij}\left(\sum_{j=1}^{J}\left(\sum_{k=1}^{K} b_j c_j[k] w_j[k]\right)\right) + \sum_{k=1}^{K} w_j[k] n_j[k]\right\}, j = 1,\ldots,J, \tag{5.31}$$

where $\Upsilon(\cdot)$ represents the non-linear transformation operation that converts the light intensity to the doubly-stochastic Poisson process and records the number of photon's arrivals and the corresponding time intervals. For the given time interval $\tau$, the probability of arriving $N_p$ number of photons at the detector of the $j$th user is given by

$$P_{rob}\left(Z_j\left(t+\tau\right)-Z_j\left(t\right)=N_p\right)=\frac{e^{-\Theta_j}\Theta_j}{N_p!}, \tag{5.32}$$

where $\Theta_j$ represents the total count rate at the receiver and is given by

$$\begin{aligned}\Theta_j &= \Theta_{j,s}+\Theta_{j,b}\\ &= \int_t^{t+\tau}\left(\sum_{i=1}^{I}h_{ij}\left(\sum_{j=1}^{J}\left(\sum_{k=1}^{K}b_j c_j[k]w_j[k]g\left(t-kT_c\right)\right)\right)+\sum_{k=1}^{K}w_j[k]n_j\left(t-kT_c\right)\right)dt\end{aligned} \tag{5.33}$$

$\theta_{j,s}$ and $\theta_{j,b}$ represent the photon count rate due to the signal and noise component, respectively.

### 5.4.4 Second-Order Cone Programming for Convex Optimization for Downlink Beamforming

To minimize the total transmit power while simultaneously satisfying Constraints 1 and 2, we construct a downlink beamforming problem expressed as

$$\textbf{minimize} \quad I\left(\sum_{j=1}^{J}\left(\sum_{k=1}^{K}\left\|b_j c_j[k]\right\|^2\right)\right)$$

$$\textbf{subject} \quad \frac{I\left(\sum_{j=1}^{J}\left(\sum_{k=1}^{K}\left\|h_{ij} b_j c_j[k] w_l[k]\right\|^2\right)\right)}{I\left(\sum_{\substack{j=1 \\ l\neq j}}^{J}\left(\sum_{k=1}^{K}\left\|h_{ij} b_l c_l[k] w_l[k]\right\|^2\right)\right)+\sum_{k=1}^{K}\left\|w_j[k] n_j[k]\right\|^2} \geq \gamma_{avg,Th}, \forall j \tag{5.34}$$

where $\gamma_{avg,Th}$ denotes the SINR threshold for the $j$th receiver. From Equation (5.34), it can be readily verified that the beamforming problem is not convex. We can now reformulate the problem as

$$\mathbf{X_j}=\mathbf{b}^{\mathbf{T}}\mathbf{C}\mathbf{C}^{\mathbf{T}}\mathbf{b}, \tag{5.35}$$

where $\mathbf{X_j}$ denotes the positive semidefinite matrix. The optimization problem defined in Equation (5.34) requires the optimal solution $\mathbf{X_j}$ to be rank-1.

The optimization problem can be then redefined as

$$\begin{aligned} &\textbf{minimize} \quad \Lambda \\ &\textbf{subject to} \quad \sqrt{\left(1+\frac{1}{\gamma_{avg,Th}}\right)}\,\mathbf{H}_j^T\mathbf{b}^T\mathbf{C} \geq \left\|\begin{matrix}\mathbf{H}_j^T\mathbf{b}^T\mathbf{B} \\ \sigma_n\end{matrix}\right\|, \forall j, \\ &\qquad\qquad \sum_{j=1}^{J}\left\|\mathbf{b}^T\mathbf{C}\right\| < \Lambda \end{aligned} \tag{5.36}$$

where $\mathbf{B} = \left[\mathbf{b}^T\mathbf{C}, \cdots, \mathbf{b}^T\mathbf{C}\right]_{1\times J}$ . The positive semidefinite matrix $\mathbf{X_j}$ relaxes the rank-1 constraint. The problem represented by Equation (5.36) is also guaranteed to have at least one optimal solution with rank one. It is to be noted that the problem defined in Equation (5.36) is constructed using a convex optimization problem with second-order cone programming as follows

$$\left(1+\frac{1}{\gamma_{avg,Th}}\right)\left|\mathbf{H}_j^T\mathbf{b}^T\mathbf{C}\right|^2 \geq \left\|\begin{matrix}\mathbf{H}_j^T\mathbf{b}^T\mathbf{B} \\ \sigma_n\end{matrix}\right\|^2, \forall j\,. \tag{5.37}$$

Taking the square root of Equation (5.37) yields a convex second-order cone constraint with the downlink beamforming optimization problem as defined in Equation (5.36).

### 5.4.5 Detection Techniques: Decision Rule with Perfect CSI

Provided the doubly-stochastic Poisson process, the detection rule for the *j*th user with perfect CSI can be formulated as

$$\frac{P_{rob}\left(Z_j(t+\tau)-Z_j(t)=N_p \middle| b_j=1\right)}{P_{rob}\left(Z_j(t+\tau)-Z_j(t)=N_p \middle| b_j=0\right)} \begin{matrix} \hat{b}_j=1 \\ >1 \\ <1 \\ \hat{b}_j=0 \end{matrix}. \tag{5.38}$$

Utilizing Equations (5.31), (5.32), and (5.38), the detection rule can readily be obtained as

$$e^{-\left\{\int_t^{t+\tau}\left(\sum_{i=1}^{I}h_{ij}\left(\sum_{j=1}^{J}\left(\sum_{k=1}^{K}b_j c_j[k]w_j[k]g(t-kT_c)\right)\right)\right)dt\right\}}$$

$$\times\left\{\frac{\int_t^{t+\tau}\left(\sum_{i=1}^{I}h_{ij}\left(\sum_{j=1}^{J}\left(\sum_{k=1}^{K}b_j c_j[k]w_j[k]g(t-kT_c)\right)\right)\right)dt}{\int_t^{t+\tau}w_j[k]n_j(t-kT_c)dt}+1\right\}^{\begin{matrix}N_p & \hat{b}_j=1\\ & >1\\ & <1\\ & \hat{b}_j=0\end{matrix}} \quad (5.39)$$

### 5.4.6 Detection Techniques: MLSD

Next, we develop MLSD of $N$ consecutive transmitted sequence $\mathbf{b}_j=\left\{b_j[n]\right\}_{n=1}^{N}$. Based on the Poisson channel defined by Equation (5.31), the detection rule can be written as [63]

$$\hat{\mathbf{b}}_j=\left\{b_j[n]_{n=1}^{N}\right\}=\arg\max_{b_j}\prod_{n=1}^{N}\mathrm{P}_{rob}\left(Z_j(t+\tau)-Z_j(t)\middle|b_j[n]\right). \quad (5.40)$$

Utilizing Equations (5.31), (5.32), and (5.40), the MLSD-based detection rule can be obtained as

$$\hat{b}_j = \left\{ b_j[n]_{n=1}^{N} \right\} = \arg\max_{b_j} \left\{ \left\{ \frac{\int_t^{t+\tau} \left( \sum_{i=1}^{I} h_{ij} \left( \sum_{j=1}^{J} \left( \sum_{k=1}^{K} b_j c_j[k] w_j[k] g(t - kT_c) \right) \right) \right) dt}{\int_t^{t+\tau} w_j[k] n_j(t - kT_c) dt} + 1 \right\}^{R_{on}} \times e^{-N_{on} \left\{ \int_t^{t+\tau} \left( \sum_{i=1}^{I} h_{ij} \left( \sum_{j=1}^{J} \left( \sum_{k=1}^{K} b_j c_j[k] w_j[k] g(t - kT_c) \right) \right) \right) dt \right\}} \right\}$$

(5.41)

where $N_0 \in \{0, 1, \cdots, N\}$ in Equation (5.41) denotes the number of ones in the hypothesis vector and $R_{on}$ is expressed as

$$R_{on} \triangleq \sum_{n_i \in B_{on}} N_p[n_i], \tag{5.42}$$

$R_{on}$ is the sum of the effective doubly-stochastic Poisson count variables. It accounts for the indices of the ones in the hypothesis vector. $B_{on}$ is a size-$N_{on}$ set of on-indices given by

$$B_{on} \triangleq \{ n_i \in \{1, 2, ..., N\} : b_j[n_i] = 1 \}. \tag{5.43}$$

### 5.4.7 Experimental Setup

In this subsection, we illustrate the experimental setup of the proposed multiuser system. The experimental setup is shown in Figure 5.6. The scenario illustrated in Figure 5.6 considers three users. The transmitter section consists of a UVTOP280 UV LED with a nominal center wavelength of 280 nm. The peak

transmits power is limited to 7 dB. The minimum pulse width is set to 20 ns. The receiver section is composed of the PMT R7154.

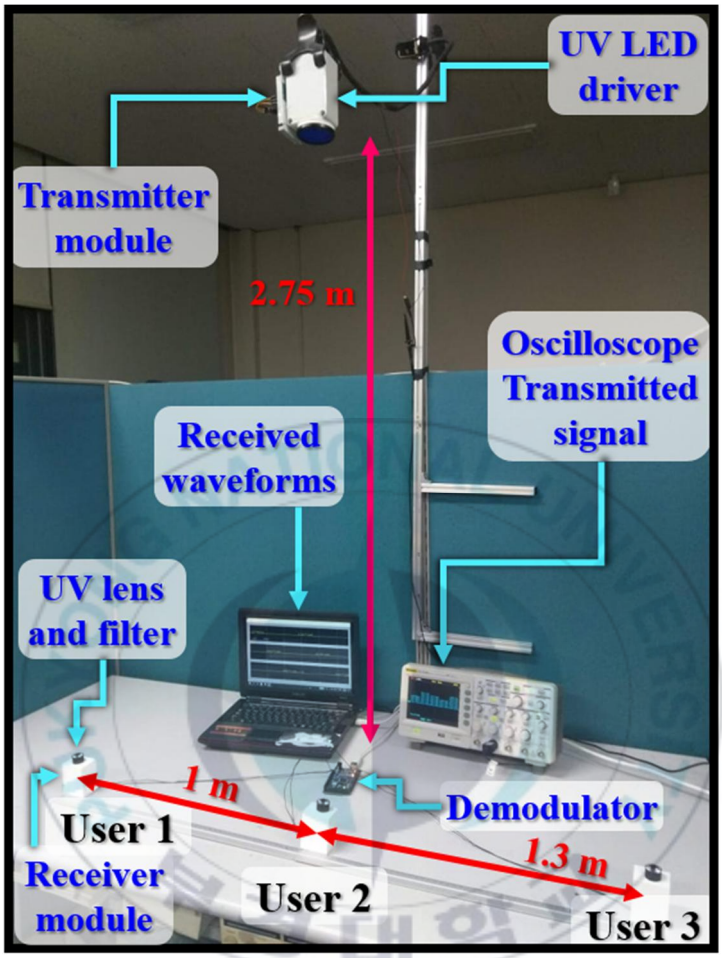


Figure 5.6 Experimental setup of the proposed indoor multiuser system.

Figure 5.7 shows the transmitted and received waveforms.

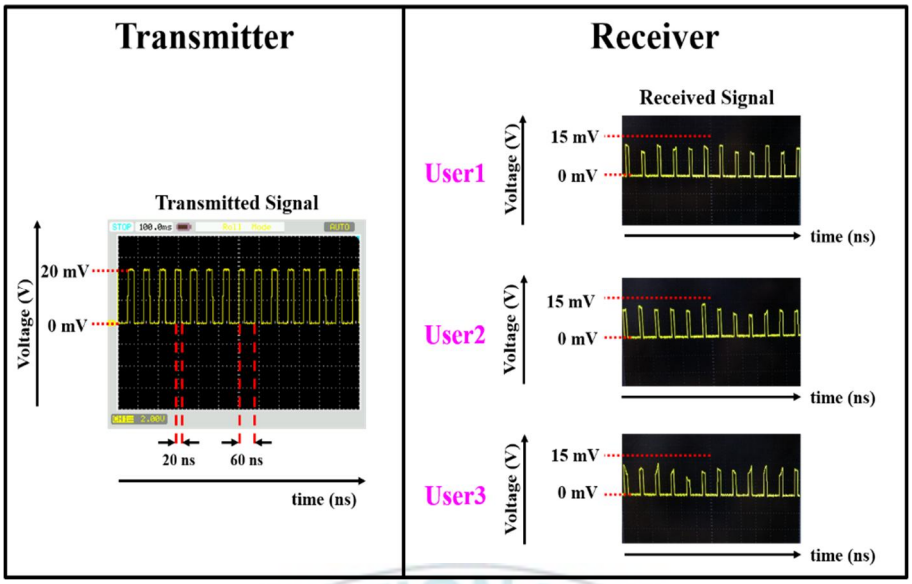


Figure 5.7 Transmitted and received waveforms.

The experimentally measured BER performance against the peak transmit power is depicted in Figure 5.8. The BER curves are obtained for different values of the control parameter $\delta$, that is, the average-to-peak power ratio. The number of users is set to three. As illustrated, the experimental results are in good agreement with the simulation results. The marginal difference between the performance obtained through the experiment and the simulation is because it is difficult to model the real noise in the simulation.

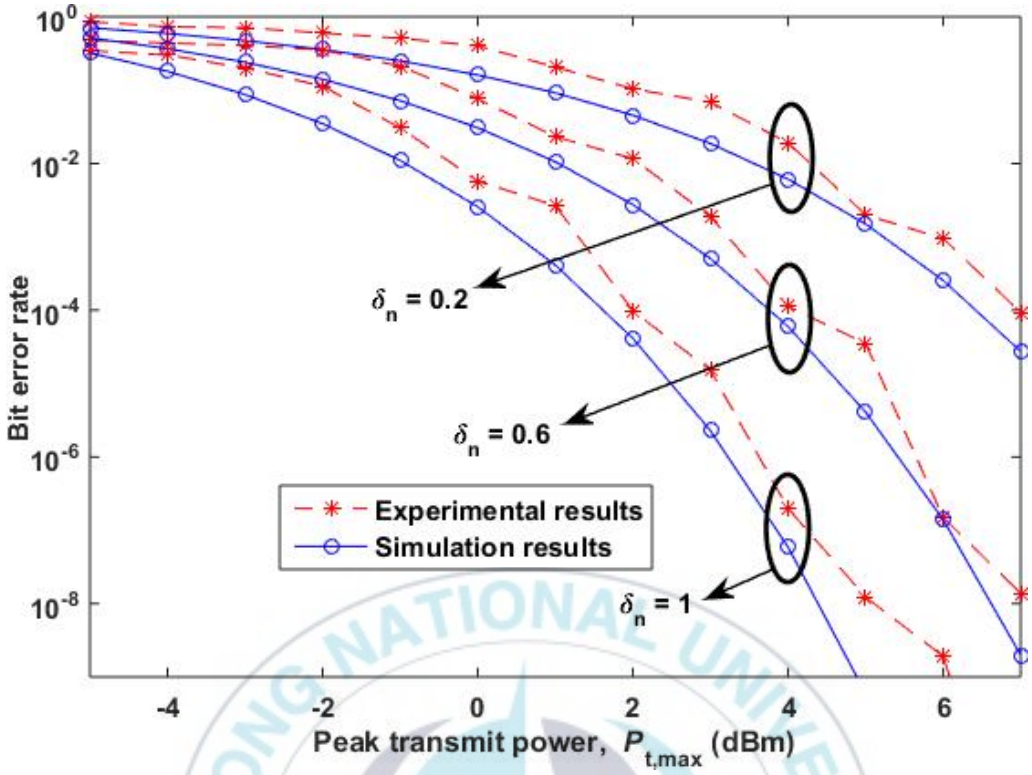


Figure 5.8 Experimentally measured BER against the peak transmit power.

# 6 Orbital Angular Momentum Assisted Optical Communications

In the recent past, the potential of the orbital angular momentum (OAM) has been explored to increase the data rate and to support multiple users. Different OAM states act as a new orthogoanl dimension and form a basis for an interference-free multiuser access technology.

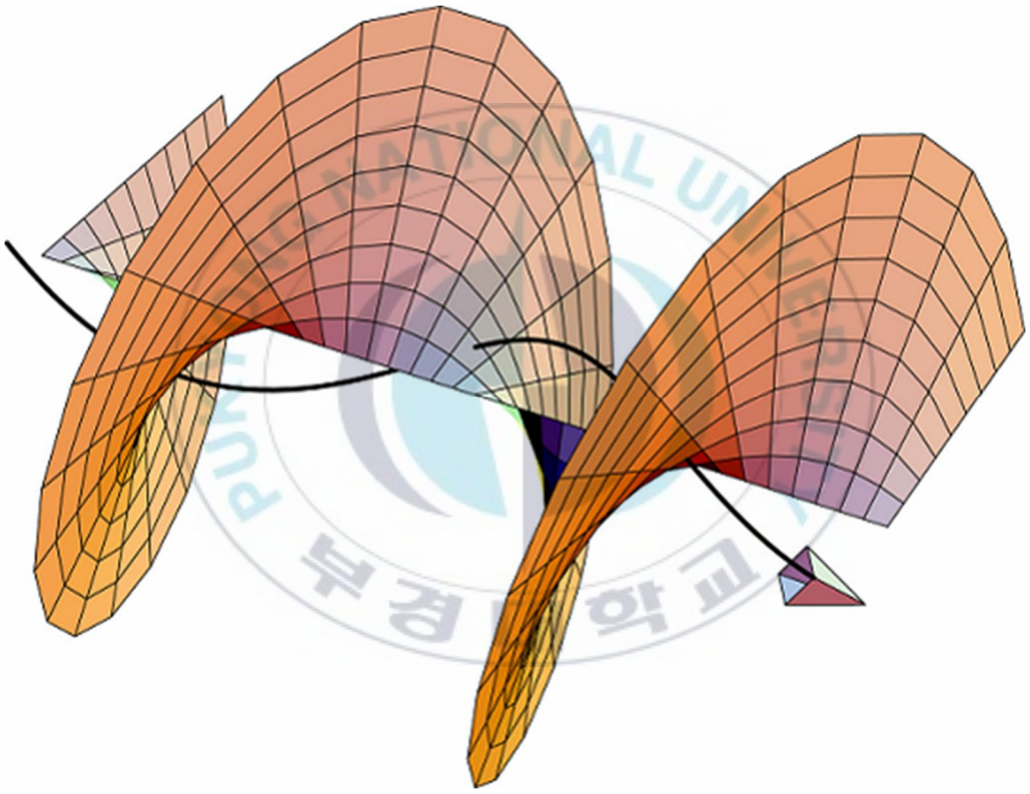

Figure 6.1 An OAM carrying optical beam with helical wavefront.

As a method to improvise the reliability of the UV communication system, we develop an OAM-based UV communication system. Our work presents a significant increase in the UV channel capacity. It is demonstrated that the proposed OAM-based UV communication outperforms the conventional IM/DD-based UV systems.

### 6.1 Signal Model

The cylindrical link geometry of the OAM-assisted UV communication system is illustrated in Figure 6.2. The cylindrical coordinate system $(r,\phi,z)$ is utilized for the system analysis where we assume the reference plane is the Cartesian $xy$-plane with equation $z = 0$. $r$ is the radius and $\phi$ is the azimuth angle between the reference direction on the chosen plane and the line from the origin to the projection of the receiver $R_x$ on the plane. $z$ is the axial distance between the transmitter and the receiver. The transmitter $T_x$ is located at the coordinate (0, 0, 0). $d$ represents the link distance between $T_x$ and $R_x$ located at the coordinates $(r,\phi,z)$.

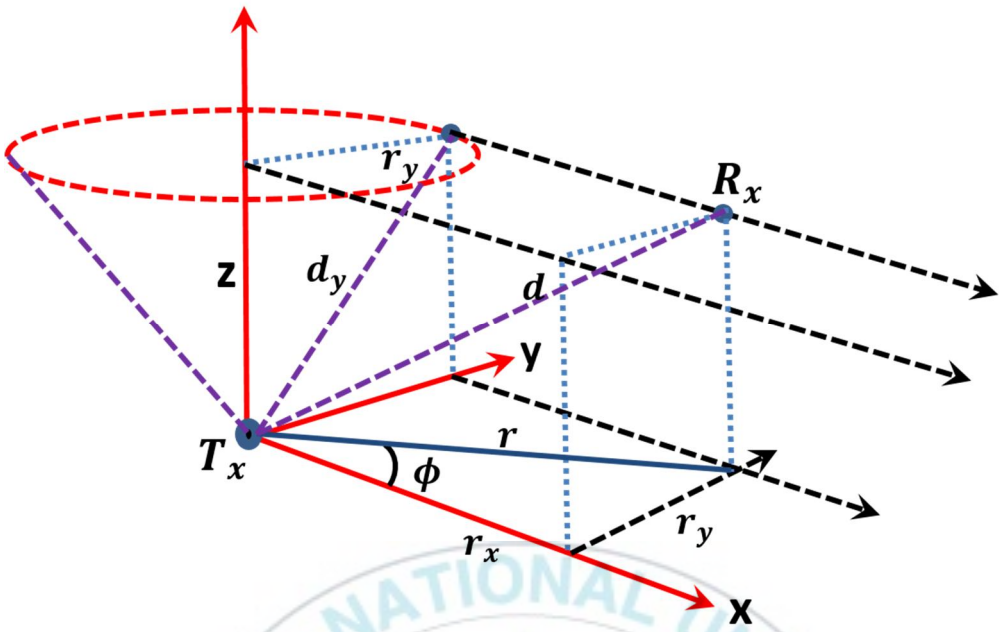


Figure 6.2 OAM-assisted UV communication link geometry in cylindrical coordinates.

The electric field of a Laguerre-Gaussian beam propagating along z-direction can be expressed in cylindrical coordinates as

$$\vec{E} = U(r,\phi,z)\hat{a}, \tag{6.1}$$

where $\hat{a}$ is a constant unit vector and the term $U(r,\phi,z)$ is given by

$$U(r,\phi,z)=\alpha\sqrt{\frac{p!}{\pi\left(p+|l|\right)!}}\frac{1}{w(z)}\left(\frac{\sqrt{2}r}{w(z)}\right)^{|l|}L_p^{|l|}\left(\frac{2r^2}{w^2(z)}\right)$$
$$\times\exp\left(-\frac{r^2}{w^2(z)}\right)\exp\left[-j\frac{z}{z_R}\left(\frac{r}{w(z)}\right)^2\right] \quad , \qquad (6.2)$$
$$\times\exp\left[-j\left(|l|+2p+1\right)\varphi(z)\right]\exp\left(-jl\phi\right)\exp\left(-jkz\right)$$

where the variables $p$ and $l$ represent the radial and azimuthal mode numbers, respectively. For a fixed $p$ , the OAM states of Laguerre-Gaussian beam are mutually orthogonal, as shown below:

$$\begin{aligned}&\left(U_l(r,\phi,z),U_m(r,\phi,z)\right)\\&=\int U_l(r,\phi,z)U_m^*(r,\phi,z)rdrd\phi \quad ,\\&=\begin{cases}0, & \forall m\neq l\\ \int\left|U_l(r,\phi,z)\right|^2 rdrd\phi, & m=l\end{cases}\end{aligned} \qquad (6.3)$$

where the operator (.,.) denotes the scalar product and * denotes the complex conjugate. As shown in Equation (6.3), therefore, different OAM states for fixed radial mode numbers $p$ are mutually orthogonal and can be used as basis functions for OAM modulation.

In addition, each OAM beam is spatially orthogonal to all other OAM beams with different OAM states when they propagate along the same axis through a single pair of apertures. Also, a pure OAM-mode is characterized by an integer and different OAM-modes are orthogonal with each other. When the

OAM-mode is a non-integer, the phase term $\exp(jl\phi)$ can be expressed by the sum of the Fourier series of orthogonal OAM-modes.

We model the channel impulse as

$$h_p^l = \beta_p^l \frac{\lambda}{4\pi d} \exp\left( j\frac{2\pi d}{\lambda} \right) \exp(jl\phi) \ , \tag{6.4}$$

with $\beta_p^l$ defines the channel gain coefficient and denotes the attenuation during the propagation of an OAM-carrying Laguerre-Gaussian UV beam. It is modeled as

$$\beta_p^l = \sqrt{G_s G_a \left| A_p^l(b,\theta) \right|^2} \ , \tag{6.5}$$

where the terms $G_s$ and $G_a$ represent the power attenuation due to the atmospheric absorption and scattering, respectively. $A_p^l(b,\theta)$ is the amplitude function of the Laguerre-Gaussian beam.

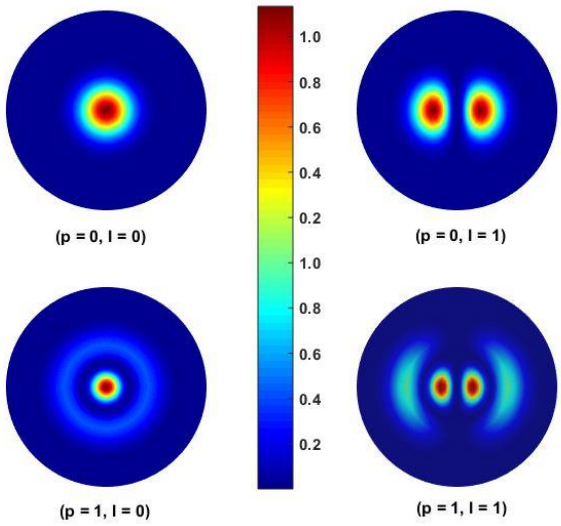


Figure 6.3 Normalized intensity distributions of various modes of the Laguerre-Gaussian beam.

It is important to note that, since the time scales of these fading processes ($\approx 10^{-3} - 10^{-4}$ seconds ) are far larger than the transmitted bit interval (3 – 5 nano-seconds) , $h_p^l$ can therefore be considered constant over a larger amount of transmitted bits. As a result, an optical channel is often termed a slow-fading flat channel and can be considered fixed over a block of bits. In addition, in a slow-fading flat optical channel, the amplitude and the phase change imposed by the channel can be considered constant over the period of use; hence, it can be written as $h_p^l(n) = h_p^l$. In addition, the delay spread in a UV channel is negligible as described in the literature [29]. For UV channels, the reported delay spreads

are on the order of one hundred nanoseconds and can thus be assumed negligible. Therefore, the optical channel is safe to be assumed as the flat channel.

## 6.2 Transmitter and Receiver Design

Next, we provide the schematic of the transmitter and the receiver sections.

### 6.2.1 Transmitter Section

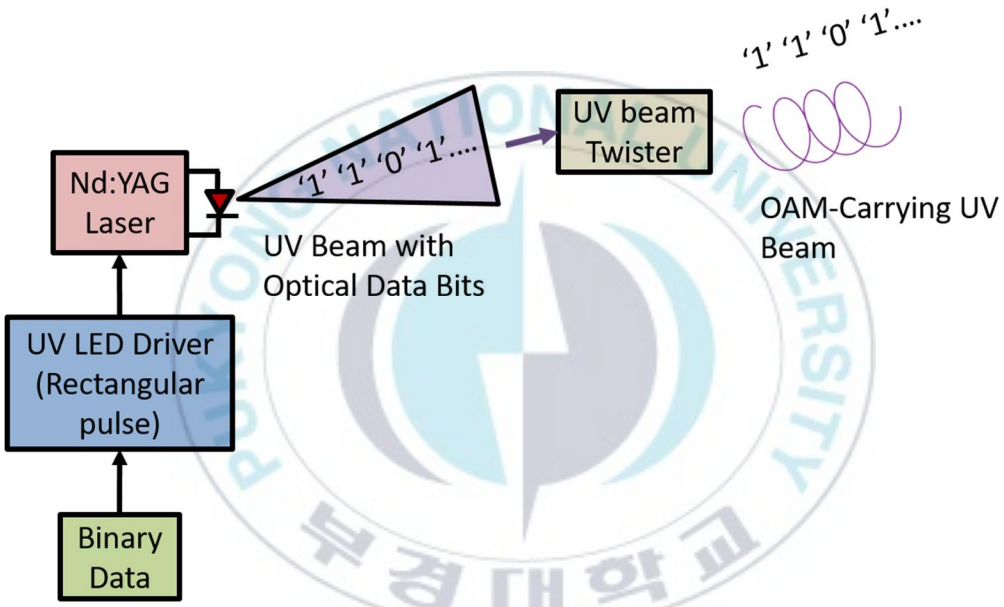


Figure 6.4 Transmitter Section

### 6.2.2 Receiver Section

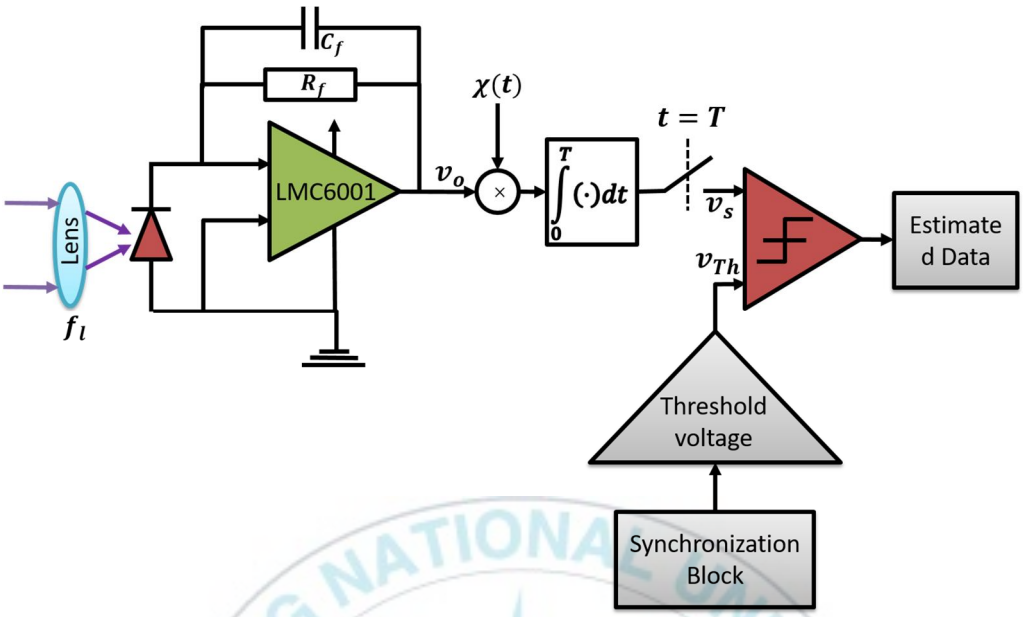


Figure 6.5 Transmitter Section

### 6.2.3 Detection of Total OAM

Equation (6.6) is derived from Maxwell's theory of electromagnetic radiation and is an important formula as it is a basis to understand the atomic physics related to the angular momentum. The angular momentum density associated with the transverse electromagnetic field of a Laguerre-Gaussian beam is given by [64]

$$\vec{M} = \varepsilon_0 \vec{r} \times \left( \vec{E} \times \vec{B} \right) \tag{6.6}$$

**Method I:**

Using Equation (6.6), the total angular momentum (consisting of the OAM and the spin angular momentum) of the Laguerre-Gaussian beam can then readily be obtained as

$$\vec{J} = \varepsilon_0 \int \vec{r} \times \left( \vec{E} \times \vec{B} \right) dr \ , \tag{6.7}$$

where

$$\vec{J} = \vec{L} + \vec{S} \ , \tag{6.8}$$

with $\vec{L}$ and $\vec{S}$ representing the OAM and the spin angular momentum, respectively. Solving Equation (6.7), the magnitudes of the spin angular momentum and OAM are then obtained as [64]

$$S = \frac{1}{4\pi c} \int_V \vec{E} \times \vec{A} dV \ , \tag{6.9}$$

$$L = \frac{1}{4\pi c} \int_V \sum_{k=x,y,z} E_k \left( \vec{r} \times \nabla \right) dV A_k dV \tag{6.10}$$

Equation (6.10) provides the exact number of the OAM mode. The amplitude of a Laguerre-Gaussian mode has an azimuthal angular dependence of $\exp(-jl\phi)$, where $l$ represents the topological charge, i.e., the OAM mode number. These modes are the eigenmodes of the angular momentum operator and carry an orbital angular momentum $l\ \hbar$ per photon [65], where $\hbar$ is equal to $\frac{h}{2\pi}$, and $h$ is Planck's constant.

**Method II:**

Alternatively, the OAM from Equation (6.6) can also be determined using the steps provided in [66] and [67]. Using Equation (6.6), the time average of the real part of $\varepsilon_0 \vec{E} \times \vec{B}$ , which is the linear momentum density, is given by

$$\frac{\varepsilon_0}{2}\left(\vec{E}^* \times \vec{B} + \vec{E} \times \vec{B}^*\right) = jw\frac{\varepsilon_0}{2}\left(U^* \nabla U - U \nabla U^*\right) + wk\varepsilon_0 |U|^2 \hat{z}, \qquad (6.11)$$

where $U(r, \phi, z)$ is defined as

$$\begin{aligned} U(r,\phi,z) = \alpha & \sqrt{\frac{p!}{\pi (p+|l|)!}} \frac{1}{w(z)} \left(\frac{\sqrt{2}r}{w(z)}\right)^{|l|} L_p^{|l|}\left(\frac{2r^2}{w^2(z)}\right) \\ & \times \exp\left(-\frac{r^2}{w^2(z)}\right) \exp\left[-j\frac{z}{z_R}\left(\frac{r}{w(z)}\right)^2\right] \\ & \times \exp\left[-j\left(|l|+2p+1\right)\varphi(z)\right] \exp(-jl\phi) \exp(-jkz) \end{aligned} . \qquad (6.12)$$

As defined in the manuscript, $L_p^{|l|}$ is the Laguerre polynomial associated with the orbital angular momentum index $l$ .

Now, considering $L_p^{|l|}$, the orbital angular momentum of a Laguerre-Gaussian beam can be measured by first converting or decomposing a Laguerre-Gaussian mode into the Hermite-Gaussian modes as follows:

$$\sum_{k=0}^{n+m}(2i)^k P_k^{(n-k,m-k)}(0)H_{n+m-k}(x)H_k(y)$$
$$=2^{n+m}\times\begin{cases}(-1)^m m!(x+jy)^{n-m}L_m^{n-m}(x^2+y^2), n\geq m\\ (-1)^n n!(x+jy)^{m-n}L_n^{m-n}(x^2+y^2), m>n\end{cases}, \quad (6.13)$$

where $H_n(x)$ and $H_m(y)$ are the Hermite polynomials associated with $TEM_{nmq}$ modes. $P_k^{(n-k,m-k)}(0)$ is defined as

$$P_k^{(n-k,m-k)}(0)=\frac{(-1)^k}{2^k k!}\frac{d^k}{dt^k}\left[(1-t)^n(1+t)^m\right]\Big|_{t=0}. \quad (6.14)$$

Now, as shown in [68], connecting the Hermite polynomials to their $45^0$ transformed value:

$$\sum_{k=0}^{n+m}(2i)^k P_k^{(n-k,m-k)}(0)H_{n+m-k}(x)H_k(y)=\left(\sqrt{2}\right)^{n+m}H_n\left(\frac{x-y}{\sqrt{2}}\right)H_m\left(\frac{x+y}{\sqrt{2}}\right). \quad (6.15)$$

It may be seen that the summation in Equation (6.15) is the same as that in Equation (6.13). *k* is an integer associated with the Hermite polynomial in the y-direction, $H_k(y)$. From Equation (6.15), we can show that

$$\begin{aligned}&\left(\sqrt{2}\right)^5 H_3\left(\frac{x-y}{\sqrt{2}}\right)H_2\left(\frac{x+y}{\sqrt{2}}\right)\\ &=H_5(x)H_0(y)-H_4(x)H_1(y)-2H_3(x)H_2(y).\\ &+2H_2(x)H_3(y)+H_1(x)H_4(y)-H_0(x)H_5(y)\end{aligned} \quad (6.16)$$

Similarly from Equation (6.13), we obtain

$$
\begin{aligned}
&32re^{j\phi}L_2^1\left(r^2\right)= \\
&H_5\left(x\right)H_0\left(y\right)+jH_4\left(x\right)H_1\left(y\right)+2H_3\left(x\right)H_2\left(y\right) \\
&+j2H_2\left(x\right)H_3\left(y\right)+H_1\left(x\right)H_4\left(y\right)+jH_0\left(x\right)H_5\left(y\right)
\end{aligned} \quad . \tag{6.17}
$$

From Equations (6.16) and (6.17), it can be easily verified that a Hermite-Gaussian mode with spatial dependence $H_n\left(x\right)H_m\left(y\right)$ gives the information of the Laguerre-Gaussian mode defined by $L_p^l\left(r^2\right)$ as in this example, $L_p^l\left(r^2\right)=L_2^1\left(r^2\right)$.

More specifically, for $L_m^{n-m}\left(r^2\right)$, $n \geq m$, we may identify $\left(n-m\right)$ as the orbital angular momentum of the photon in units of $\hbar$.

### 6.3 Results and Discussions

The average error rate of the proposed OAM-carrying Laguerre-Gaussian beam is illustrated in Figure 6.6. The radial index $p$ is set to one. For the proof of concept, the performance is compared with the conventional UV link utilizing OOK modulation. As expected, the performance is found to be a function of the radial distance $z$. An important observation can be inferred that the proposed OAM assisted UV link outperforms the conventional UV link equipped with OOK modulation. This can be attributed to the fact the propagation mechanism of the Laguerre-Gaussian beam is significantly different from the conventional beam. The energy of the OAM-carrying Laguerre-

Gaussian beam is focused within a circular region surrounding the beam axis. It yields different propagation gains within the circle and outside the circle region. This phenomenon provides superiority in the performance of the UV link with the OAM-carrying Laguerre-Gaussian beam over the conventional UV link.

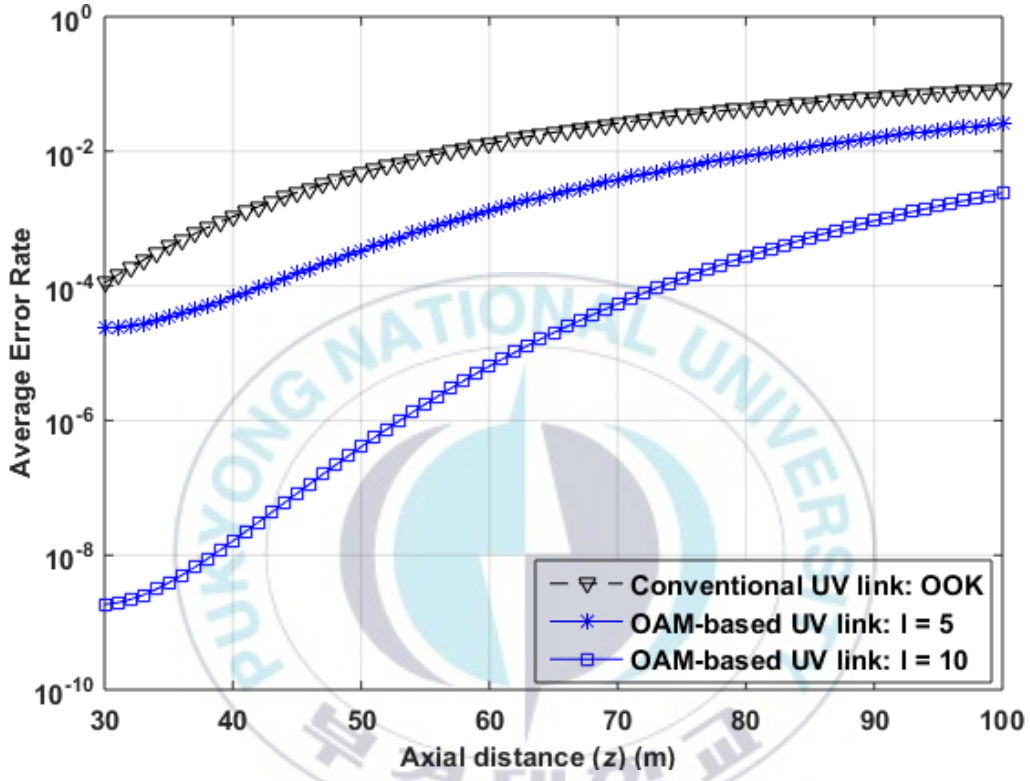


Figure 6.6 Average error rate as a function of the axial distance $z$.

The average symbol error rate performance as a function of the topological charge $l$ and the radial index $p$ is depicted in Figure 6.6. Two important observations can be made. First, keeping the radial index $p$ value

constant, while increasing the topological charge $l$ value, the average error rate decreases. The justification for this behavior is provided below.

The radii of the outer ring of the OAM-carrying Laguerre-Gaussian beam are proportional to $\sqrt{l}$. The OAM-carrying Laguerre-Gaussian beam has a ring-shaped intensity profile. Because the outermost ring of the beam is relatively wide, a considerable amount of total beam energy is allocated to the outermost ring. For instance, for the Laguerre-Gaussian beam with $l = 5$ and $p = 1$, the outermost ring accounts for $44.4\%$ of the total beam energy, whereas the intensity at the center is approximately zero [69]. Therefore, with $l$, the size of the outermost ring increases with lower destructive interference. It results in higher received energy over a given distance for a fixed $p$.

The second important observation made is that with fixed topological charge $l$, the average symbol error rate increases with the radial index $p$. This behavior is because the spot size decreases in the focal region as the radial index $p$ value increases. The decrease in the spot size is due to the destructive interference produced by the longitudinal electric field components of the inner rings to the outermost rings. For instance, in an OAM-carrying Laguerre-Gaussian beam with $p = 2$, the focal spot size is effectively reduced because of the existence of $180^0$ phase shift between the inner and the outer ring. Therefore, as the degree of radial polarization increases, the number of rings of OAM-

carrying beam increases and the destructive interference increases, thereby leading to a reduction in the focal spot size, and hence higher error rate.

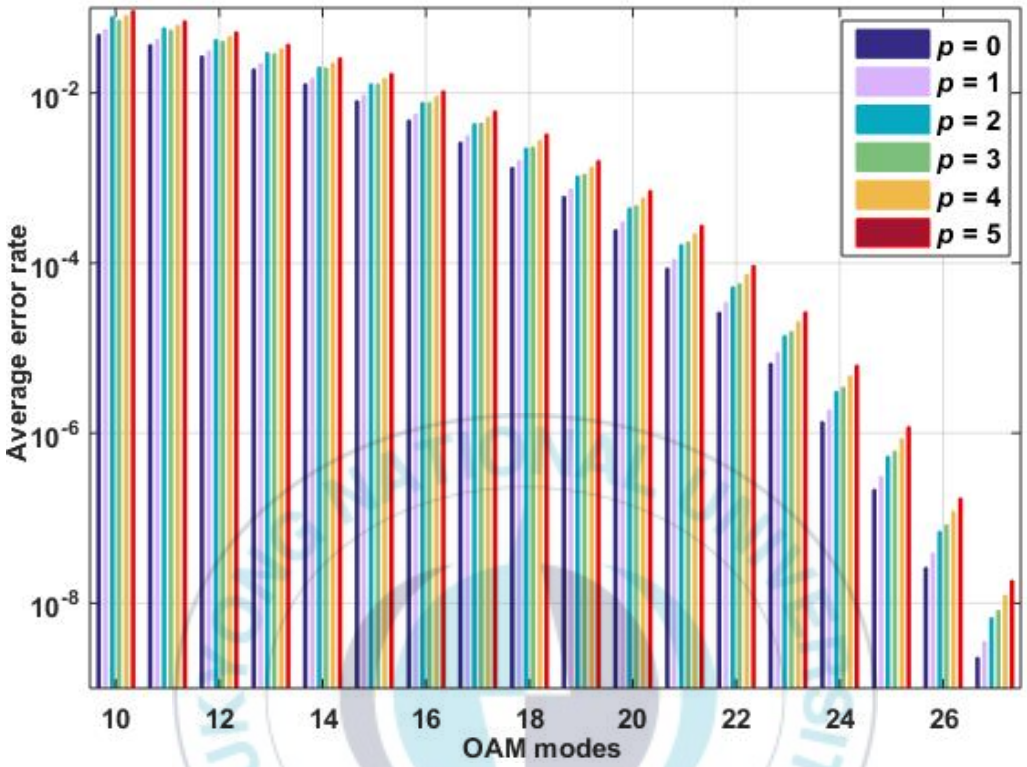


Figure 6.7 Average error rate as a function of the OAM modes $l$ for the given radial index $p$.

# 7 Optical Scattering Based Intervehicular Communications

Given unique propagation features of radiation in the Ultraviolet-C (UV-C) band that ranges from 200 to 280 nanometers, ultraviolet communications become increasingly popular. This chapter presents a novel self-organizing non-line-of-sight (NLOS) ultraviolet (UV) based intervehicular communication (IVC). In contrast to conventional IVCs based on radio frequency (RF), infrared (IR), and visible light, the UV based IVC bypasses the need for expensive infrastructure, supports non-line-of-sight (NLOS) vehicle-to-vehicle communications over a long distance, and can also be implemented using simple networking protocols with less stringent pointing, acquisition, and tracking (PAT) requirements. Furthermore, the UV-IVC system is compact and requires low primary power for operation. Experiments for proof-of-principle purposes were conducted with two vehicles in both stationary and time-varying UV channels. It is demonstrated that the proposed UV-IVC is capable of providing low-cost, low-power, and NLOS capable intervehicular communications with acceptable performance.

Bluetooth radio technology was also adopted in intervehicular and road-to-vehicle communications in traffic jam conditions in the context of the intelligent transport system (ITS) [70]. The most critical drawback in adopting Bluetooth for IVC is that it imposes a piconet structure that is difficult to

maintain in a dynamic IVC. Furthermore, new vehicle nodes joining existing piconets would encounter significant delays [71]. IR laser was utilized in IVC as an intervehicular networking method for bidirectional information exchange by applying a spread spectrum [72]. This laser-based IVC was dedicated to determining the exact location of the vehicles and the distance between them. Apparently, this IVC is vulnerable to any blockage in the link, due to the directionality of the laser beam. Visible light communication (VLC) was also applied for IVC, based on the controller area network [73]. Unfortunately, this IVC is limited to line-of-sight (LOS) transmission only for a distance of up to 20 m. In addition, outdoor visible light-based IVCs would suffer from sunlight noise that causes photodetector saturation problems. The outdoor solar background or fluorescent noise may significantly limit the performance of IR and visible light receivers [74]. A comparison of existing IVC network access technologies are listed in Table 7.1 [75].

Table 5.2 Comparison of IVC network access technology.

| Access Type | Bluetooth | Infrared Data | VLC | 802.11p |
|---|---|---|---|---|

| Features | | Association (IrDA) | | |
|---|---|---|---|---|
| **Frequency Band/Wavelength** | 2.4 GHz ISM band | 850-900 nm | 400-780 nm | 5.8-5.9 GHz |
| **Data rate** | 1 Mbps | 4-16 Mbps | 400 Mbps | 54 Mbps |
| **Range** | 100 m | 2 m | 100 m | 1 km |
| **License** | Free | Free | Free | Licensed |
| **Cost** | Low | Low | Low | High |
| **Mobility** | Very low | No | Low | High |
| **Weather condition** | Robust | Less sensitive | Sensitive | Robust |
| **Ambient light interference** | Not affected | Less sensitive | Very sensitive | Not affected |
| **LOS required** | No | Yes | Yes | No |

### 7.1 System Overview and Experimental Setup

The pictorial representation of the UV-based IVC communication is illustrated in Figure 7.1. In regard to geometry parameters, $\beta_{Tx}$ (transmit off-axis angle) is defined as the angle between the baseline distance and the projection of the transmit beam axis on the horizontal plane (ground plane). Similarly, $\beta_{Rx}$

(receiver off-axis angle) represents the angle between the baseline distance and the projection of the receiver FOV on the horizontal plane. If the transmitter and the receiver are moving in the same lane, then $\beta_{Tx}$ and $\beta_{Rx}$ will be equal to zero, resulting in the coplanar geometry. If any of the angles $\beta_{Tx}$ and $\beta_{Rx}$ is non-zero, the link geometry will be non-coplanar. The non-coplanar link geometry generally occurs when the transmitter and the receiver are moving in a different lane. As described previously, the common volume formed from this geometry in space plays an important role in UVC, contributing to the strength of the received signal. The common volume is determined by parameters including the baseline distance $d$ between the transmitter and the receiver, the off-axis angles $\beta_{Tx}$ and $\beta_{Rx}$, the transmitter beam angle $\Phi_{Tx}$, the receiver FOV $\Phi_{Rx}$, and the transmitter and receiver focal (or apex) angles $\Psi_{Tx}$ and $\Psi_{Rx}$. In addition to this common volume, the received signal is influenced by the photon density incident on the volume and characteristics of scattering particles within the volume.

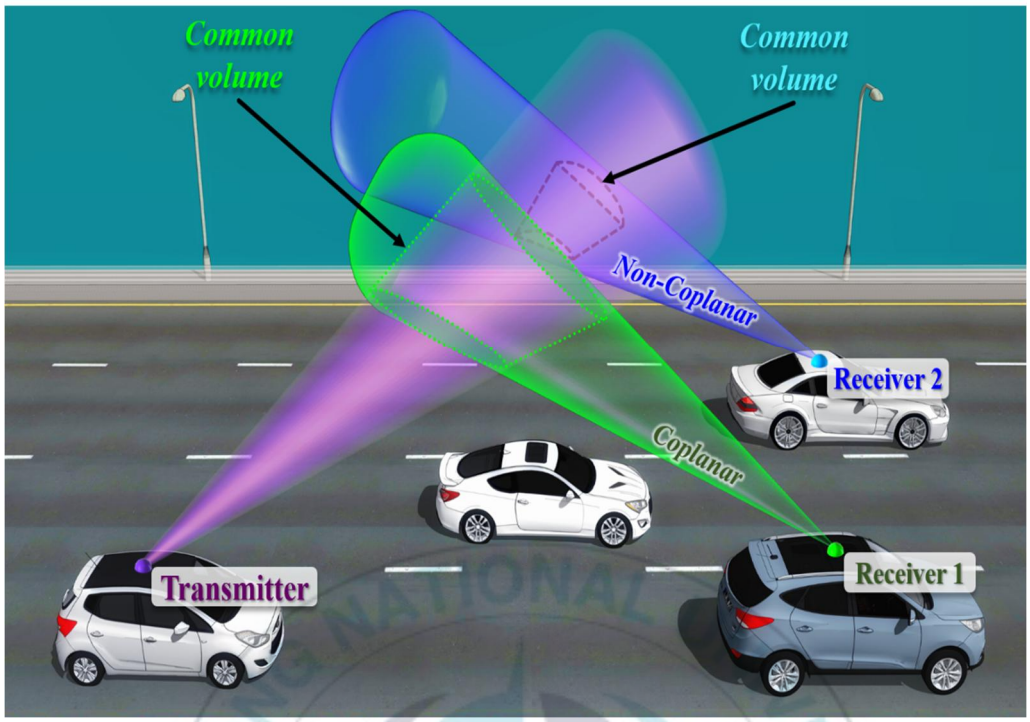


Figure 7.1 Optical scattering based NLOS IVC communications.

The system model is depicted in Figure 7.2. The transmitter employs a waveform generator feeding binary sequences to current driver circuitry that powers the UV LED. The binary data is used to modulate the intensity of the optical carrier, i.e. a continuous wave UV LED. At the receiver, the incoming UV radiation is passed through an OBPF and is then converted into an electrical signal by the direct detection photodiode. The OBPF is used to limit the amount of background radiation noise. The PMT is employed at the receiver. The PMT

output current is directed to the low noise amplifier followed by a photon counter unit.

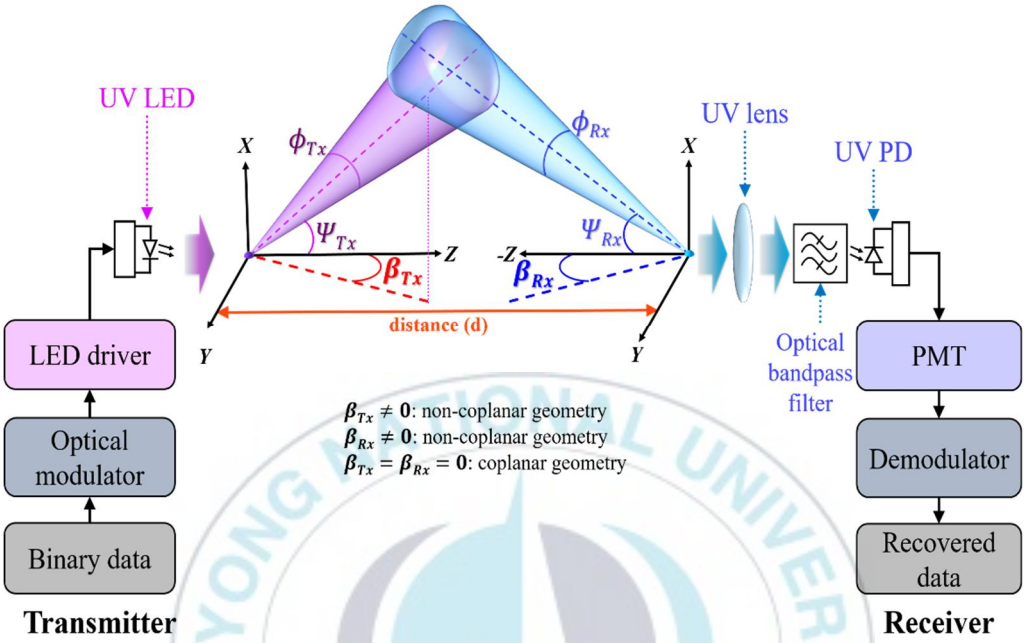


Figure 7.2 System model.

The proposed UV-IVC can be implemented with a low-power miniaturized transceiver. To validate the potential of the UV-IVC, we performed experiments with the following transceiver. For the transmitter, a 280 nm UV LED array was deployed with 1.5 mW average output optical power with a forward current of 20 mA and $\Phi_{Tx}$ equal to 114°. The transmitting pulse width was set to 10 μs, ensuring that sufficient photons were emitted from the LED with a duty cycle of approximately 20 percent. In the receiver, a PMT was

deployed along with the silicon carbide (SiC) based UV photodiode with a FOV ($\Phi_{Rx}$) of 100° for 60 percent of the normalized signal output. It is responsive to wavelengths from 221 nm to 358 nm with a wavelength of maximum spectral responsivity equal to 280 nm with a responsivity of 0.13 $AW^{-1}$ and dark current of 1.7 fA at a reverse voltage of 1 V. For the correct reading of the photodiode, a trans-impedance amplifier was employed at the receiver. The apex angle of both the transmitter and the receiver was set to 45°.

### 7.2 Experimental Conditions and Environment

The following measurements were carried out across three different sites. Sites A and B are the open field campus areas and Site C is outside the campus on an urban highway. On Site A, the two test vehicles drove on the same lane and therefore can be thought of as a coplanar link. On Site B, the two test vehicles drove on different lanes forming a non-coplanar geometry. The mid-points of the two lanes are separated by 16 m. Figure 5 displays a snapshot of the streets inside and outside the campus. The channel measurements were conducted during the daytime from 10 a.m. to 4 p.m., November 5 through 23. The outdoor temperature was ranged from 8.8 degrees Centigrade to 17.2 degrees Centigrade and the wind speed measured during the experiment periods was 5.1 m/s to 5.36 m/s. The average relative humidity was measured at 57%.

Unless otherwise stated, during the measurement, the vehicles maintained an average constant speed of 40 km/h.

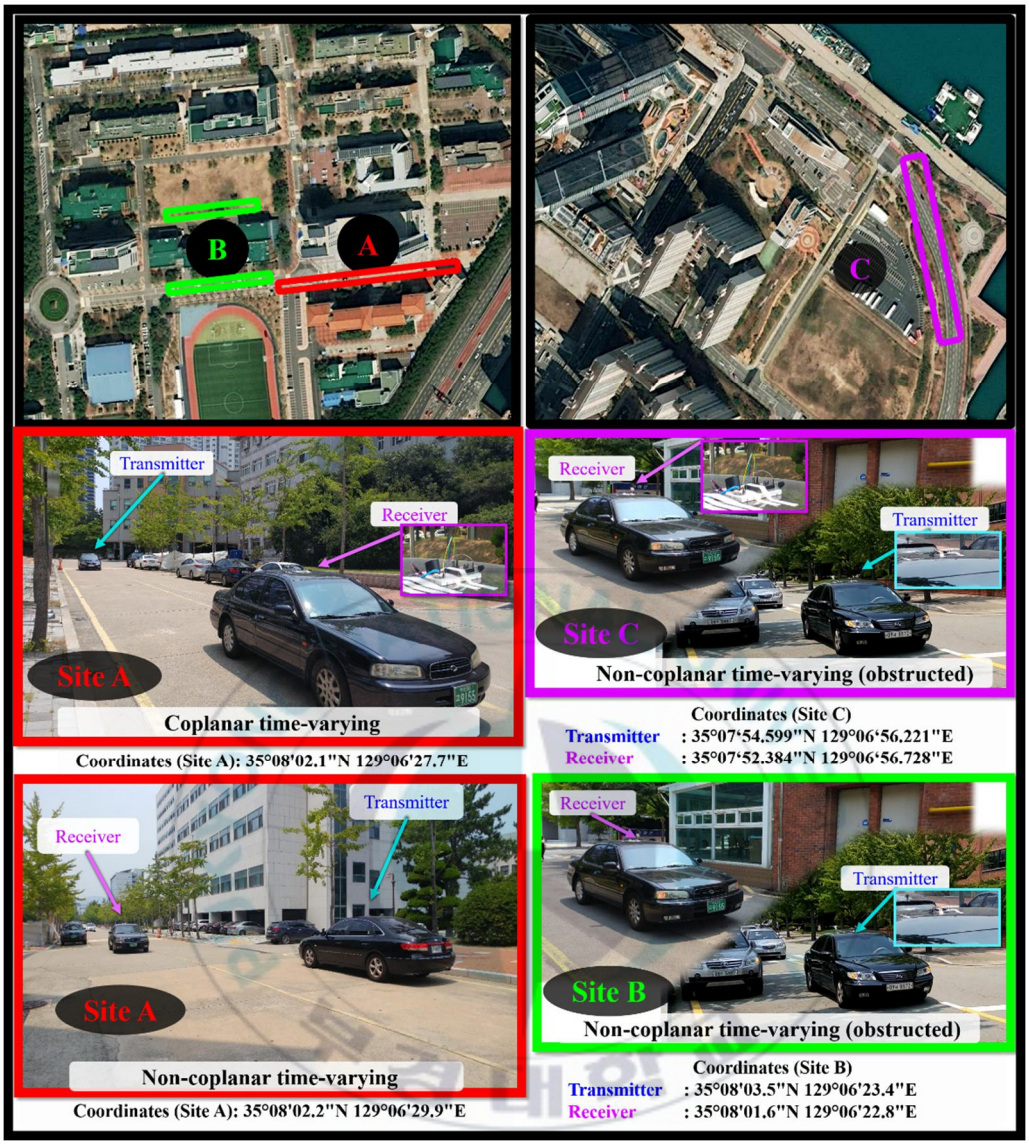


Figure 7.3 Site locations for experimental verification.

## 7.3 Received Power Profile

The received power measurement relative to the distance is illustrated in Figure 7.4. The random variation in the received power represents multiple unresolvable components by a single process.

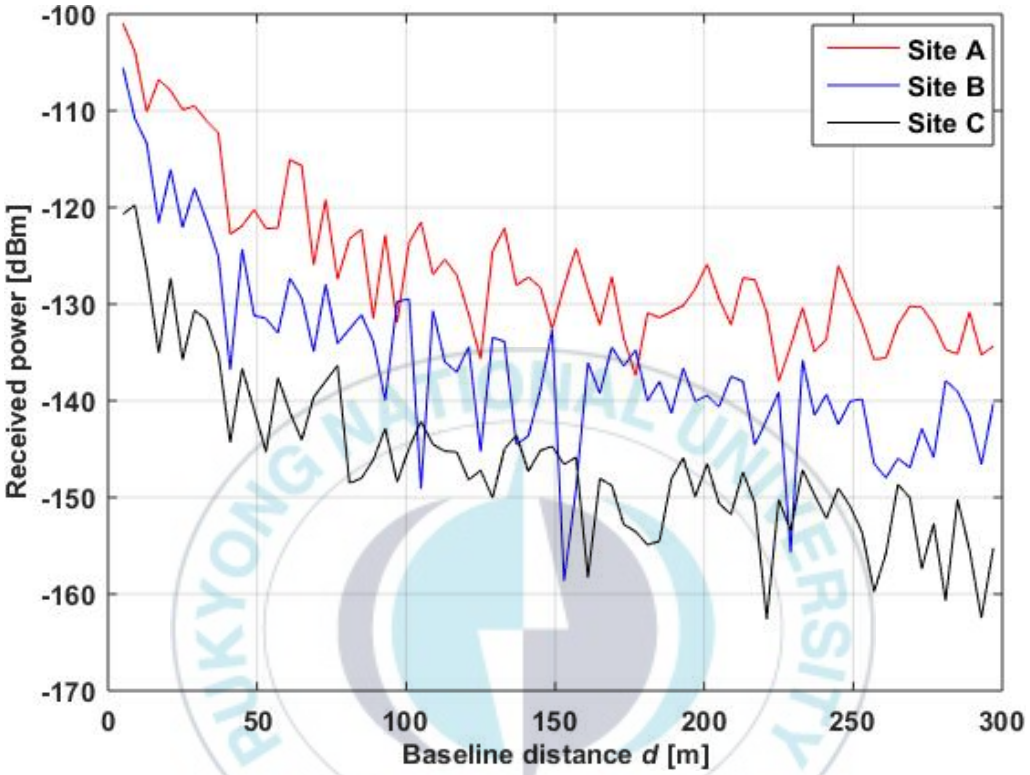


Figure 7.4 Measurement of the received power as a function of baseline distance at different sites.

The PDFs of the fading statistics measured at different sites are illustrated in Figure 7.5. The estimation of the fading statistics can be well fitted by an appropriate distribution model. We applied a test with a 95% confidence interval to ensure that an appropriate fit is obtained. The sliding window size is

set to $10\lambda$. The standard deviation values of the fading are obtained by averaging repeated measurements.

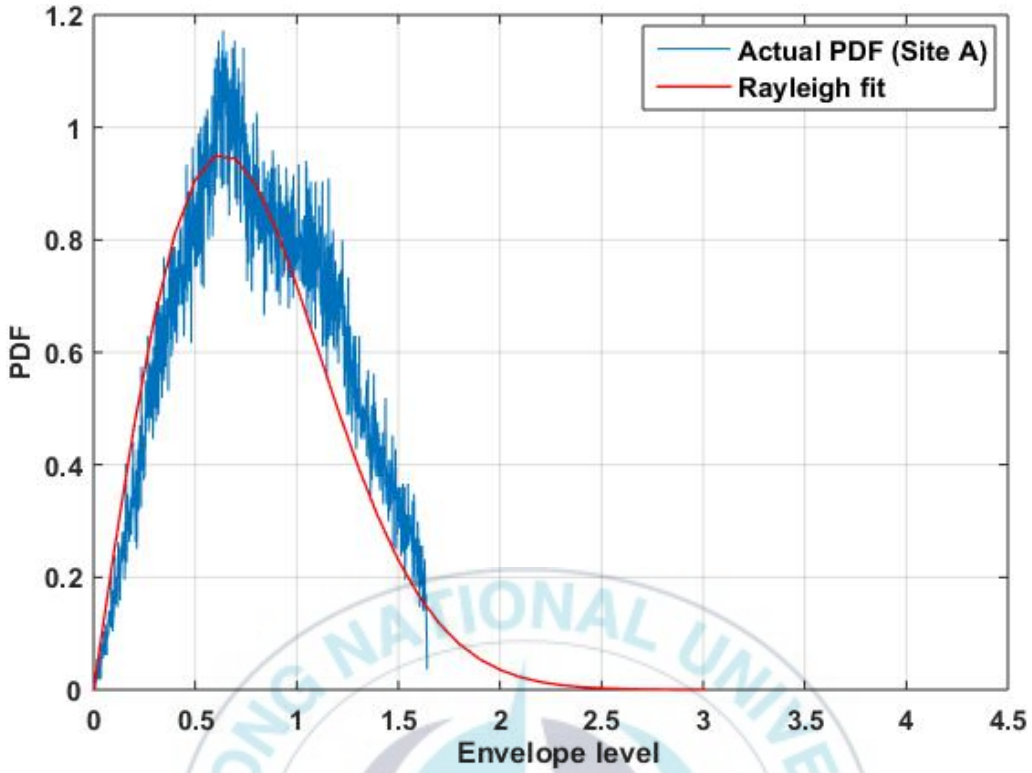


(a) Fading statistics at Site A.

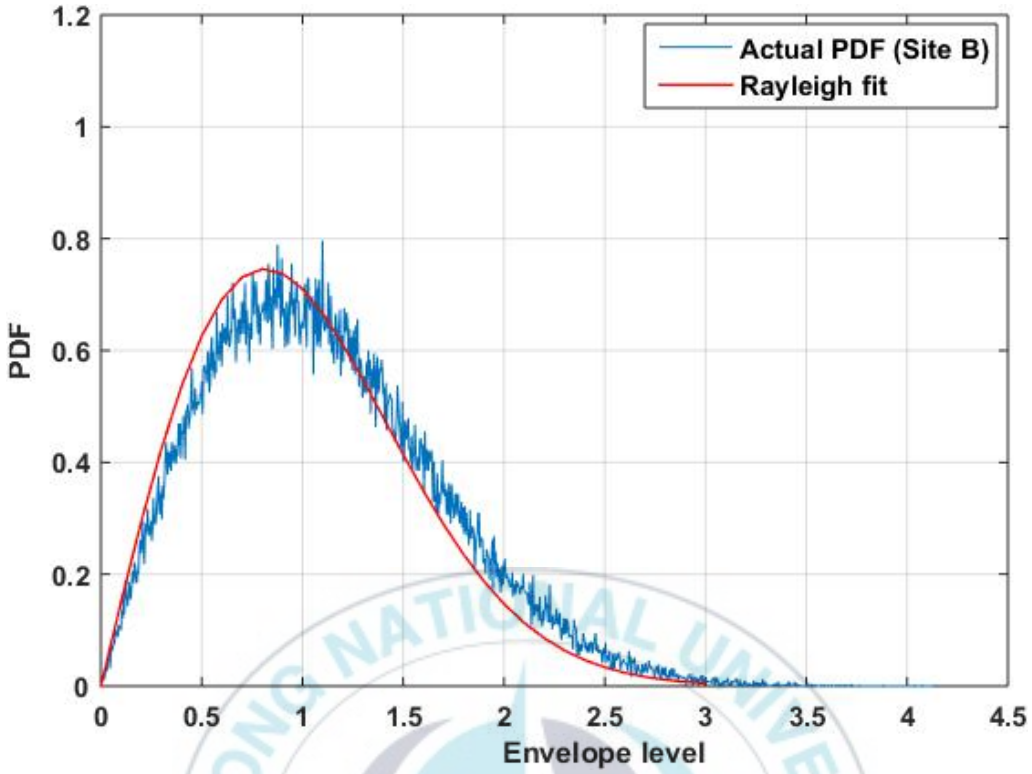


(b) Fading statistics at Site B.

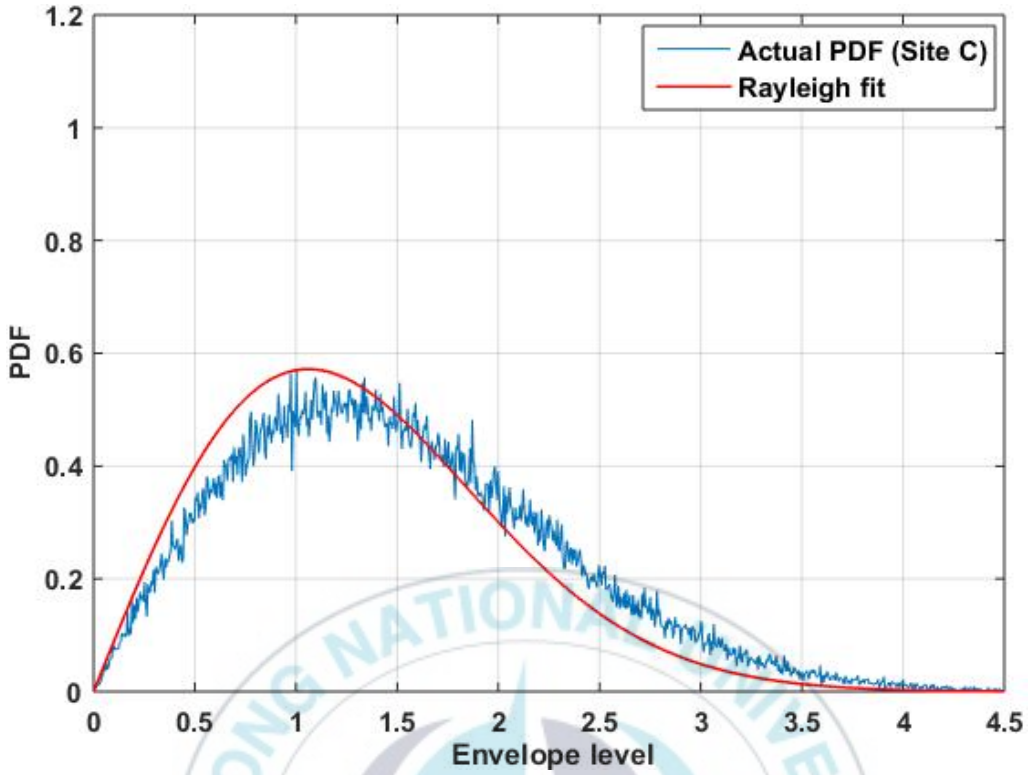


(c) Fading statistics at Site C.

Figure 7.5 Channel characteristic measurements at different sites.

To analyze the large-scale fading statistics, we first average the received optical power for each time instant, such that

$$P_r(t) = \frac{1}{T_{avg}} \sum_{t'=t-T_{avg}/2}^{t+T_{avg}/2} \left| H[t', f] \right|^2 \tag{7.1}$$

Subsequently, we further average over the small-scale fading by using a moving window spanning $T_{avg}$. The choice of $T_{avg}$ is such that the small-scale fading is

averaged out. Finally, we obtain the large-scale fading $LS_F|_{dB}$ as the variation of

$$F_{\text{Large-scale}}(t,f)\Big|_{dB} = P_r\big|_{dB} - E_t\left\{P_r\big|_{dB}\right\}, \tag{7.2}$$

where $E_t\{\cdot\}$ represents the sample mean over the time axis. The Rayleigh distribution has been empirically confirmed for fitting the amplitude distribution of shadow fading.

Table 7.2 Measurement of the Path Loss Exponent.

| Site | Path Loss Exponent |
|---|---|
| A | 1.9 |
| B | 2.1 |
| C | 2.2 |

## 7.4 Baseband Representation of the UV-based IVC Channel

The channel impulse response model and the baseband representation of the non-stationary uncorrelated scattering channel for ultraviolet-based vehicular communication are illustrated in Figures 7.6 and 7.7, respectively.

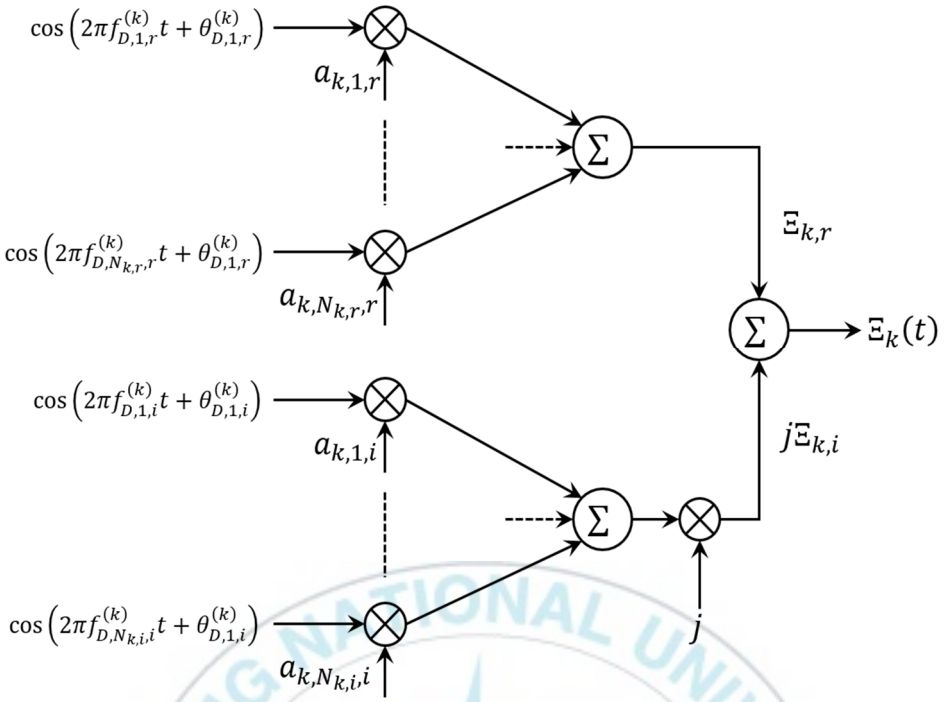


Figure 7.6 Channel impulse response model for UV-based IVC.

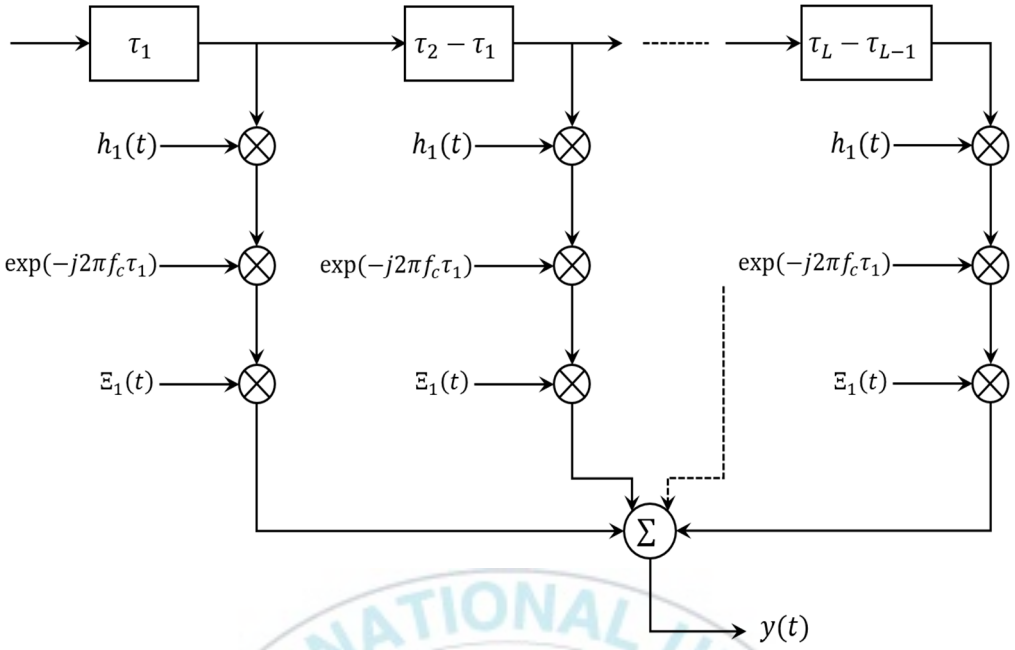


Figure 7.7 Baseband representation of the non-stationary uncorrelated scattering channel IVC communication.

To investigate the signal dispersion further and to gain more insight, we develop an algorithm to track the time-varying delay. In this algorithm, we estimate the differential delay between the two multipath components at each time instant. For an unknown time-varying transmitter, receiver, and scatter position $\mathbf{T}_p$, $\boldsymbol{R}_p$, and $\boldsymbol{S}_p$, respectively, the path delay $\tau_k(t)$ is given by

$$\tau_k(t) = \frac{1}{c}\left(\left\|\mathbf{S}_p - \mathbf{T}_p\right\| + \left\|\mathbf{R}_p - \mathbf{S}_p\right\|\right) \tag{7.3}$$

where $c$ is the speed of light. Using (7.3), the Doppler frequency component over the $k^{\text{th}}$ propagation path is formulated as

$$f_{D,T}^{(k)} + f_{D,R}^{(k)} = \frac{f_c}{c}\left( v_{T_x} \frac{\mathbf{S}_p^{(k)} - \mathbf{T}_p}{\left\| \mathbf{S}_p^{(k)} - \mathbf{T}_p \right\|} + v_{R_x} \frac{\mathbf{R}_p - \mathbf{S}_p^{(k)}}{\left\| \mathbf{R}_p - \mathbf{S}_p^{(k)} \right\|} \right) \tag{7.4}$$

where $v_{T_x}$ and $v_{R_x}$ represent the transmitter and receiver velocity, respectively. $f_D^{(k)} = f_{D,T}^{(k)} + f_{D,R}^{(k)}$ . $\tau_k(t)$ and $f_D^{(k)}$ are represented jointly as a multivariate Gaussian distribution $\Upsilon \sim N(\varpi, \sum)$ defined in the parameter space $\delta_k(t)$ observable in the measured snapshot of time $t$ as

$$\delta_k = \begin{bmatrix} \tau_k \\ f_D^{(k)} \end{bmatrix}, \tag{7.5}$$

where $\varpi = \left[ E[\tau_k],\ E\left[ f_D^{(k)} \right] \right]^T$ is a vector of mean values. The covariance matrix is given by

$$\sum = \begin{bmatrix} \sigma_{\tau_k}^2 & 0 \\ 0 & \sigma_{f_D^{(k)}}^2 \end{bmatrix}, \tag{7.6}$$

Based on $\Upsilon \sim N(\varpi, \sum)$ , the PDF of $\delta_k$ can readily be obtained as

$$f_{\delta_k}\left(\delta_k; \varpi, \Sigma\right) = \frac{1}{2\pi\sigma_\tau \sigma_{f_D}} \exp\left[ -\frac{\left(\tau_k - E[\tau_k]\right)^2}{2\sigma_\tau^2} - \frac{\left(f_D^{(k)} - E\left[f_D^{(k)}\right]\right)^2}{2\sigma_{f_D^{(k)}}^2} \right] \tag{7.7}$$

For the $k^{\text{th}}$ path, we represent the time-variant parameters as $b_k(t) = [\delta_k(t)^T,\ \Delta\delta_k(t)^T]^T$, where $\Delta\delta_k(t)$ denotes the nonobservable rate values of the observable parameters $\delta_k(t)$.

The process equation can be formulated as

$$\mathbf{B}\left(t+\Delta t\right) = \mathbf{T}_{t,t+1}\mathbf{B}(t) + \boldsymbol{\lambda}_p\left(t\right), \tag{7.8}$$

where $T_{t,t+\Delta t}$ denotes the transition matrix taking the state $\mathbf{B}(t)$ from time $t$ to time $t+\Delta t$. $\lambda_p(t)$ denotes the background process noise. Following (7.8), the measurement equation can readily be expressed as

$$\mathbf{y}(t) = \mathbf{M}\mathbf{B}\left(t\right) + \boldsymbol{\lambda}_m\left(t\right), \tag{7.9}$$

where $\mathbf{y}(t)$ is observable at time $t$ and $M$ denotes the measurement matrix. $\boldsymbol{\lambda}_m(t)$ is the measurement noise and is uncorrelated to the process noise $\boldsymbol{\lambda}_p(t)$. Let $\hat{\mathbf{B}}^{-}(t)$ denote *a priori* estimate of the state vector $\hat{\mathbf{B}}(t)$. The *a posteriori* estimate of the state vector can then be expressed as

$$\hat{\mathbf{B}}\left(t\right) = \mathbf{G}_B\left(t\right)\mathbf{B}^{-}\left(t\right) + \mathbf{G}_y\left(t\right)\mathbf{y}\left(t\right), \tag{7.10}$$

where $\mathbf{G}_B(t)$ is the multiplying matrix factor and $\mathbf{G}_y(t)$ is the Kalman gain matrix. Define the state error vector

$$\tilde{\mathbf{B}}\left(t\right) = \mathbf{B}\left(t\right) - \hat{\mathbf{B}}\left(t\right), \tag{7.11}$$

and apply the principle of orthogonality, it yields

$$E\left[\tilde{\mathbf{B}}(t)\mathbf{y}^T(t')\right]=0\ \forall\ t'<t \quad . \tag{7.12}$$

We employ the maximum-likelihood ($ML$) estimation defined by

$$ML\left\{\mathbf{y}(t),\hat{\mathbf{B}}^{-}(t)\right\}=\mathbf{B}_{ML}(t) \quad , \tag{7.13}$$

such that the output of the $ML$ estimator converges around the *a priori* estimate $\hat{\mathbf{B}}^{-}(t)$ . It follows

$$E\left[\left(\mathbf{B}(t)-\hat{\mathbf{B}}^{-}(t)\right)\left(ML\left\{\mathbf{y}(t'),\mathbf{B}^{-}(t)\right\}\right)^T\right]=0\ \forall\ t'<t \quad . \tag{7.14}$$

Using (7.11), (7.12), and (7.14), and applying the fact that the process and measurement noise are uncorrelated, we obtain

$$E\left\{\left(\mathbf{I}-\mathbf{G}_y(t)\mathbf{M}-\mathbf{G}_B(t)\right)\mathbf{B}(t)\left(ML\left\{\mathbf{y}(t'),\hat{\mathbf{B}}^{-}(t)\right\}\right)^T\right\}$$
$$+E\left\{\mathbf{G}_B(t)\left(\mathbf{B}(t)-\hat{\mathbf{B}}^{-}(t)\right)\left(ML\left\{\mathbf{y}(t'),\mathbf{B}^{-}(t)\right\}\right)^T\right\}=0 \quad . \tag{7.15}$$

From (7.13), it can be shown that (7.15) holds true for any arbitrary state vector $\mathbf{B}(t)$ and observable $\mathbf{y}(t')$ if and only if

$$\mathbf{G}_B(t)=\mathbf{I}-\mathbf{G}_y(t)\mathbf{M} \quad , \tag{7.16}$$

thereby yielding the necessary condition for $\mathbf{G}_B(t)$. Following this, the *a posteriori* estimate of the state $\mathbf{B}(t)$ at time $t$ can be expressed as

$$\hat{\mathbf{B}}^{-}(t) = \mathbf{B}^{-}(t) - \mathbf{G}_{y}(t)\left\{\left(ML\left\{\mathbf{y}(t'), \hat{\mathbf{B}}^{+}(t)\right\}\right) - \mathbf{M}\mathbf{B}^{-}(t)\right\}. \quad (7.17)$$

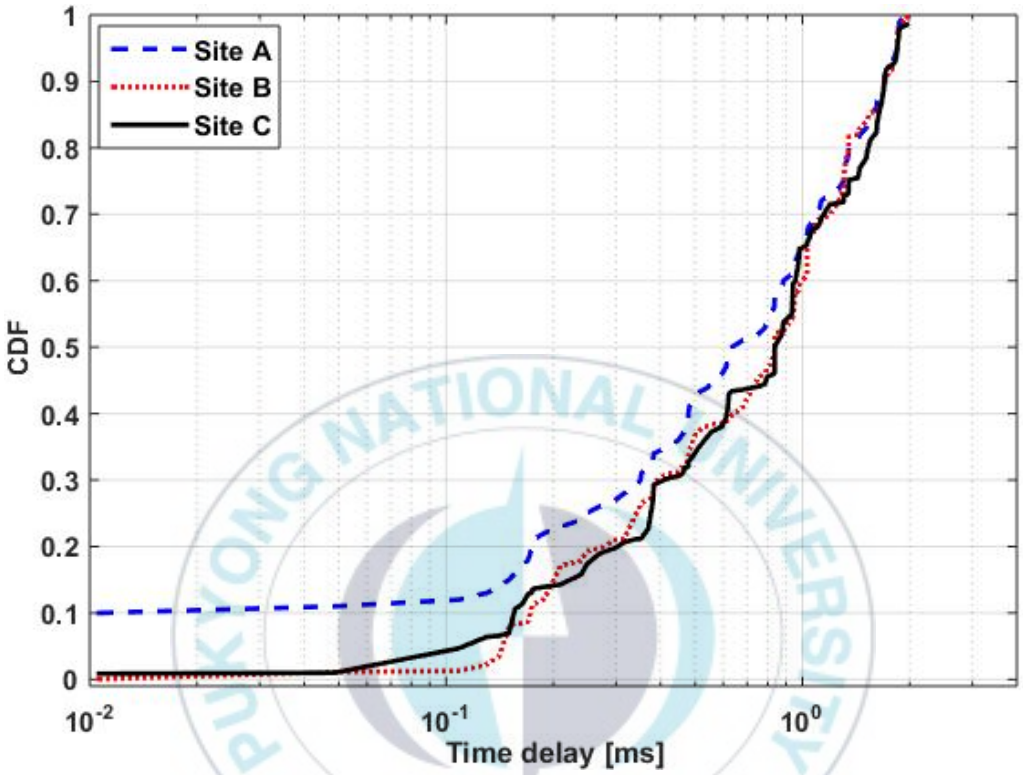


Figure 7.8 Measurement of time-delay statistics at different sites.

In the process of analyzing the time-varying scattering channel, the main objective is to obtain information about the statistical distribution of spatial-temporal characteristics of the underlying channel. Figure 13 displays typical time-delay statistics. Among the various measurements performed at different

sites, Site A shows the lowest delay spread, while Site B and Site C display slightly higher delay spreads.

### 7.5 Future Scope

A new V2V communication system based on the NLOS ultraviolet transmission has been proposed with a few attractive features inherited from its propagation characteristics such as low-cost, low-power, long-distance, and non-line-of-sight transmission capability. A more rigorous study on this UV-IVC is still needed to be more viable. For example, when many vehicles are involved in the transmission, the synchronization issue needs to be addressed. An extension can also be made by considering multiple access schemes over spatial, temporal, wavelength, and code dimensions. Over more realistic traffic conditions with varying transmitter beam and/or receiver FOV angles, the UV-IVC needs to be further investigated. More importantly, the NLOS transmission capability of the UV-IVC needs to be rigorously studied under various weather conditions. It is, however, envisioned that even over unfriendly weather conditions, the UV-IVC can still maintain superiority with multi-hop transmission schemes that would minimize the effect of atmospheric conditions over a relatively short distance between hops. The present scheme can also be enhanced by designing a hybrid architecture to integrate its access to different wireless network technologies with the aim of enabling seamless use of

communication services for users inside a vehicle. To accommodate the need for many classes of applications, comprehensive networking protocols and solutions are also worth exploring.

# 8 Conclusion

This thesis has delivered the design and modeling of state-of-the-art NLOS optical scattering communication systems. This thesis has also explored multiple aspects of optical scattering communication systems and networks, including receive and transmit diversity techniques, optical spectrum sensing, game theory, ANN, indoor optical communications, and OAM.

In the first part of the thesis, the spatial diversity techniques have been analyzed in the correlated turbulence channel. With received signal characterized by a continuous waveform detector, we have investigated the SSC receive diversity and maximal selection transmit diversity techniques. It has been demonstrated that the maximal selection transmits diversity technique significantly outperforms the RC and OSTBC techniques.

The next study has focused on developing optical spectrum sensing techniques. First, an energy detection-based optical spectrum sensing technique has been presented for a continuous waveform detector. It has been demonstrated that the proposed technique guarantees a reliable optical spectrum sensing performance while enhancing spectrum utilization efficiency. In addition, a generic blind spectrum sensing has been developed. Next, for a system where the received signal is characterized as a photon-counting receiver, we have proposed two novel cooperative optical spectrum sensing techniques:

centralized and decentralized techniques. In the centralized technique, it has been assumed that the decision-making capability is only available at the fusion center, whereas the decentralized spectrum sensing technique requires only one-bit information (a local binary decision), instead of all the raw data, to be sent to the fusion center by each collaborative user.

We have also introduced an ANN-based learning approach to the classification and detection problem in optical scattering communications. We have proposed a classification algorithm that is adaptive to varying channel conditions. Moreover, an analytical tool has been developed to estimate the fading parameters.

The next part of the thesis has focused on the development of novel and state-of-the-art UV-based indoor communications. The indoor channel model has been developed. Various design issues in indoor UV communication have been considered. It is shown that the UV indoor channel can be characterized completely by their path loss and delay spread. It is found that, in the absence of shadow fading, the impulse response with LOS components yields the smallest delay spread ranging from 0.1 to 0.4 ns. For the diffused and the scattered environment, the delay spread is found to vary between 1 and 4 ns.

In addition, a free space wireless channel model for the Laguerre-Gaussian UV beam with the fixed OAM mode has been considered. The exact

closed-form expressions for the ASER and the channel capacity have first been derived. Based on these novel expressions, the performance and capacity have been analyzed. It is demonstrated that the OAM-carrying UV communication system outperforms the conventional UV communication system in terms of performance and capacity. The received beam divergence is found to be a limiting factor as the distance increases. This limitation is, however, envisioned to be readily addressed by employing multiple receivers.

The last section proposed a novel non-line-of-sight capable V2V communication system using solar-blind ultraviolet signal has been presented. With no necessity of expensive infrastructure, the proposed UV-IVC can readily be deployed with miniaturized transceivers. To highlight the main features, the UV-IVC has been experimentally demonstrated in both stationary and time-varying UV channel conditions. Moreover, the non-coplanar geometry with the transmitter and the receiver obstructed by buildings has been evaluated. It is found that the proposed UV-IVC can provide good performance as long as sufficient common volume is formed in space. The performance degrades as the vehicle speed increases over a long distance. The UV-IVC system can be further enhanced with more sophisticated modulation schemes and networking protocols. As the UV-IVC is based on the common volume formed between the transmitter and the receiver in space, it is inherently capable of providing non-

line-of-sight transmission at a low cost. In addition, the beam pointing and acquisition are not necessary. Thus, the proposed UV-IVC can be envisioned as a low-cost, low-power, and compact alternate IVC to conventional RF based IVCs.

# 9 References


[1] A. S. Hamza, J. S. Deogun and D. R. Alexander, "Classification framework for free space optical communication links and systems," *IEEE Communications Surveys & Tutorials,* vol. 21, no. 2, pp. 1346-1382, 2018.

[2] M. A. Khalighi and M. Uysal, "Survey on free space optical communication: A communication theory perspective," *IEEE communications surveys \& tutorials,* vol. 16, no. 4, pp. 2231--2258, 2014.

[3] "Optical communication in space: Challenges and mitigation techniques," *IEEE Communications Surveys & Tutorials,* vol. 19, no. 1, pp. 57-96, 2016.

[4] Z. Xu and B. M. Sadler, "Ultraviolet communications: potential and state-of-the-art," *IEEE Communications Magazine,* vol. 46, no. 5, pp. 67-73, 2008.

[5] Z. Xu, "Approximate performance analysis of wireless ultraviolet links," in *IEEE International Conference on Acoustics, Speech and Signal Processing-ICASSP'07*, 2007.

[6] D. M. Reilly, D. T. Moriarty and J. A. Maynard, "Unique properties of solar blind ultraviolet communication systems for unattended ground sensor networks," *International Society for Optics and Photonics,* vol. 5611, pp. 244-255, 2004.

[7] H. C. van de Hulst, Light scattering by small particles, Wiley, 1957.

[8] W. Liu, D. Zou and Z. Xu, "Modeling of optical wireless scattering communication channels over broad spectra," *JOSA A,* vol. 32, no. 3, pp. 486-490, 2015.

[9] "Guidelines on limits of exposure to ultraviolet radiation of wavelengths between 180 nm and 400 nm (incoherent optical radiation)," *Health Physics,* vol. 87, no. 2, pp. 171-186, 2004.

[10] "IEC 61508 Functional safety of electrical/electronic/programmable electronic safety-related systems," *International Electrotechnical Commission, Geneva, Switzerland,* 1998.

[11] L. R. Koller, Ultraviolet radiation.//(Book on UV radiation covering arcs, incandescent radiation sources, solar radiation, transmission, reflection, detectors and application), New York: New York, John Wiley and Sons, Inc., 1965.

[12] J. Parrish, "UV-A: Biological effects of ultraviolet radiation with emphasis on human responses to longwave ultraviolet," *Springer Science & Business Media,* 2012.

[13] J. M. Kahn and J. R. Barry, "Wireless infrared communications," *Proceedings of the IEEE,* vol. 85, no. 2, pp. 265-298, 1997.

[14] S. Arya and Y. H. Chung, "Non-line-of-sight ultraviolet communication with receiver diversity in atmospheric turbulence," *IEEE Photonics Technology Letters,* vol. 30, no. 10, pp. 895-898, 2018.

[15] S. Arya and Y. H. Chung, "M-PSK subcarrier intensity modulation with switch-and-stay diversity for NLOS ultraviolet communication," in *TENCON 2018-2018 IEEE Region 10 Conference*, South Korea, 2018.

[16] S. Arya and Y. H. Chung, "Maximal Selective Transmit Diversity for Petahertz Wireless Communications With Continuous Waveform Detector," *IEEE Access,* vol. 9, pp. 118005-118018, 2021.

[17] S. Arya and Y. H. Chung, "Amplify-and-forward multihop non-line-of-sight ultraviolet communication in the gamma--gamma fading channel," *Journal of Optical Communications and Networking,* vol. 11, no. 8, pp. 422-436, 2019.

[18] T. A. Tsiftsis, H. G. Sandalidis, G. K. Karagiannidis and M. Uysal, "Optical wireless links with spatial diversity over strong atmospheric turbulence channels," *IEEE Transactions on Wireless Communications,* vol. 8, no. 2, pp. 951-957, 2009.

[19] T. Claudio, V. Vito, P. Boyan, L. Angelo and C. Alessandra, "Improved algorithm for calculations of Rayleigh-scattering optical depth in standard atmospheres," *Applied Optics,* vol. 44, no. 16, pp. 3320--3341, 2005.

[20] W. O. Popoola and Z. Ghassemlooy, "BPSK Subcarrier Intensity Modulated Free-Space Optical Communications in Atmospheric Turbulence," *Journal of Lightwave Technology,* vol. 27, no. 8, pp. 967 - 973, 2009.

[21] J. Li, J. Q. Liu and D. P. Taylor, "Optical Communication Using Subcarrier PSK Intensity Modulation Through Atmospheric Turbulence Channels," *IEEE Transactions on Communications,* vol. 55, no. 8, pp. 1598 - 1606, 2007.

[22] G. Yang, M.-A. Khalighi, Z. Ghassemlooy and S. Bourennane, "Performance evaluation of receive-diversity free-space optical communications over correlated gamma-gamma fading channels," *Applied Optics,* vol. 52, no. 24, p. 5903–5911, 2013.

[23] H. Moradi, H. Refai and P. LoPresti, "Switch-and-stay and switchand-examine dual diversity for high-speed free-space optics links," *IET Optoelectronics,* vol. 6, no. 1, pp. 34-42, 2012.

[24] M. H. Ardakani, A. R. Heidarpour and M. Uysal, "Performance analysis of relay-assisted NLOS ultraviolet communications over turbulence channels," *Journal of Optical Communications and Networking,* vol. 9, no. 1, pp. 109 - 118, 2017.

[25] L. C. Andrews and R. L. Phillips, Laser Beam Propagation Through Random Media, vol. 152, Bellingham, WA, USA: SPIE, 2005.

[26] H. Ding, *Modeling and characterization of ultraviolet scattering communication channels,* Riverside, CA, USA: Ph.D. dissertation, Dept. Elect. Eng., UC Riverside, 2011.

[27] J. C. Ricklin and F. M. Davidson, "Atmospheric turbulence effects on a partially coherent Gaussian beam: implications for free-space laser communication," *JOSA A,* vol. 19, no. 9, pp. 1794-1802, 2002.

[28] S. Z. Denic, I. Djordjevic, J. Anguita, B. Vasic and M. A. Neifeld, "Information theoretic limits for free-space optical channels with and without memory," *Journal of Lightwave Technology,* vol. 26, no. 19, pp. 3376-3384, 2008.

[29] B. Sharma, "Some formulae for generalized function of two variables," *Matemati{\v{c}}ki Vesnik,* vol. 5, no. 43, pp. 43-52, 1968.

[30] "The wolfram functions site wolfram research, inc.," [Online]. Available: http://functions.wolfram.com.

[31] G. C. A. K. M. a. Z. X. H. Ding, "A parametric single scattering channel model for non-line-of-sight ultraviolet communications," *SPIE,* vol. 7091, 2008.

[32] G. A. Shaw, A. M. Siegel and M. L. Nischan, "Demonstration system and applications for compact wireless ultraviolet communications," *SPIE,* vol. 5071, pp. 241-252, 2003.

[33] X. Zhu and J. M. Kahn, "Free-space optical communication through atmospheric turbulence channels," *IEEE Transactions on Communications,* vol. 50, no. 8, pp. 1293-1300, 2002.

[34] D. M. Junge, *Non-line-of-sight electro-optic laser communications in the middle ultraviolet,* California: Ph.D. dissertation,Naval Postgraduate School, 1977.

[35] C. Gong and Z. Xu, "Temporal spectrum sensing for optical wireless scattering communications," *Journal of Lightwave Technology,* vol. 33, no. 18, p. 3890–3900, 2015.

[36] X. Liu, C. Gong and Z. Xu, "Sequential detection for optical wireless scattering communication," *Journal of Optical Communications and Networking,* vol. 9, no. 9, p. D86–D95, 2017.

[37] J. C. Brandenburg and J. Q. Liu, "Optical signal detection in the turbulent atmosphere using pin photodiodes," *IEEE Journal on Selected Areas in Communications,* vol. 27, no. 9, p. 1564–1571, 2009.

[38] S. Arya and Y. H. Chung, "Spectrum sensing for free space optical communications in strong atmospheric turbulence channel," *Optics Communications,* vol. 445, pp. 24-28, 2019.

[39] X. Zhu and J. M. Kahn, "Free-space optical communication through atmospheric turbulence channels," *IEEE Transactions on communications,* vol. 50, no. 8, pp. 1293-1300, 2002.

[40] S. Karp, R. M. Gagliardi, S. E. Moran and L. B. Stotts, Optical channels: fibers, clouds, water, and the atmosphere, Springer Science \& Business Media, 2013.

[41] A. Garcia-Zambrana, "Error rate performance for STBC in free-space optical communications through strong atmospheric turbulence," *IEEE communications letters,* vol. 11, no. 5, pp. 390-392, 2007.

[42] S. Arya and Y. H. Chung, "A novel blind spectrum sensing technique for multi-user ultraviolet communications in atmospheric turbulence channel," *IEEE Access,* vol. 7, pp. 58314-58323, 2019.

[43] S. C. Y. H. Arya, "Generic blind spectrum sensing scheme for all optical-wavelength multi-user free space optical communications," *Optics Communications,* vol. 450, pp. 316-321, 2019.

[44] I. Gradshteyn and I. Ryzhik, Table of Integrals, Series, and Products, Academic Press, 2014.

[45] S. Arya and Y. H. Chung, "Spectrum Sensing for Optical Wireless Scattering Communications Over M{\'a}laga Fading-A Cooperative Approach with Hard Decision Fusion," *IEEE Transactions on Communications,* vol. 69, no. 7, pp. 4615-4631, 2021.

[46] H. Ding, G. Chen, A. K. Majumdar, B. M. Sadler and Z. Xu, "Modeling of non-line-of-sight ultraviolet scattering channels for communication," *IEEE Journal on Selected Areas in Communications,* vol. 27, no. 9, pp. 1535-1544, 2009.

[47] H. Ding, Z. Xu and B. M. Sadler, "A path loss model for non-line-of-sight ultraviolet multiple scattering channels," *EURASIP Journal on Wireless Communications and Networking,* vol. 2010, pp. 1-12, 2010.

[48] R. J. Drost, T. J. Moore and B. M. Sadler, "UV communications channel modeling incorporating multiple scattering interactions," *JOSA A,* vol. 28, no. 4, pp. 686-695, 2011.

[49] P. Wang and Z. Xu, "Characteristics of ultraviolet scattering and turbulent channels," *Optics Letters,* vol. 38, no. 15, pp. 2773-2775, 2013.

[50] W. Liu and Z. Xu, "Characteristics of optical scattering and turbulence communication channels," in *2014 48th IEEE Asilomar Conference on Signals, Systems and Computers*, 2014.

[51] Y. A. Brychkov, O. I. Marichev and N. V. Savischenko, Handbook of Mellin Transforms, CRC Press, 2018.

[52] K. Wang, C. Gong, D. Zou and Z. Xu, "Turbulence channel modeling and non-parametric estimation for optical wireless scattering communication," *Journal of Lightwave Technology,* vol. 35, no. 13, pp. 2746-2756, 2017.

[53] N. D. Chatzidiamantis, G. K. Karagiannidis and M. Uysal, "Generalized maximum-likelihood sequence detection for photon-counting free space optical systems," *IEEE transactions on communications,* vol. 58, no. 12, pp. 3381-3385, 2010.

[54] Y. Zeng and Y.-C. Liang, "Eigenvalue-based spectrum sensing algorithms for cognitive radio," *IEEE Transactions on Communications,* vol. 57, no. 6, pp. 1784-1793, 2009.

[55] C. Cao, H. Li, Z. Hu and H. Zeng, "One-bit transceiver cluster for relay transmission," *IEEE Communications Letters,* vol. 21, no. 4, pp. 925-928, 2016.

[56] N. Farsad and A. Goldsmith, "Neural network detection of data sequences in communication systems," *IEEE Transactions on Signal Processing,* vol. 66, no. 21, pp. 5663-5678, 2018.

[57] H. Lee, S. H. Lee, T. Q. Quek and I. Lee, "Deep learning framework for wireless systems: Applications to optical wireless communications," *IEEE Communications Magazine,* vol. 57, no. 3, pp. 35-41, 2019.

[58] P. G. Pachpande, M. H. Khadr, A. F. Hussein and H. Elgala, "Visible light communication using deep learning techniques," in *2018 IEEE 39th Sarnoff Symposium*, 2018.

[59] S. Arya and Y. H. Chung, "Novel indoor ultraviolet wireless communication: design implementation, channel modeling, and challenges," *IEEE Systems Journal,* vol. 15, no. 2, pp. 2349-2360, 2020.

[60] R. J. Drost and B. M. Sadler, "Survey of ultraviolet non-line-of-sight communications," *Semiconductor Science and Technology,* vol. 29, no. 8, 2014.

[61] S. Arya and Y. H. Chung, "State-of-the-art ultraviolet multiuser indoor communication over power-constrained discrete-time Poisson channels," *Optical Engineering,* vol. 59, no. 10, p. 106106, 2020.

[62] S. Arya and Y. H. Chung, "Novel Multiuser Indoor Ultraviolet Communications," in *GLOBECOM 2020 - 2020 IEEE Global Communications Conference, 2020*, 2020.

[63] M. L. Riediger, R. Schober and L. Lampe, "Multiple-symbol detection for photon-counting mimo free-space optical communications," *IEEE Transactions on Wireless Communications,* vol. 7, no. 12, p. 5369–5379, 2008.

[64] J. Jackson, Classical Electrodynamics, Thrid, Ed., John Wiley \& Sons, 1999.

[65] D. Marcuse, Light Transmission Optics, Van Nostrand, New York, 1972.

[66] R. A. Beth, "Mechanical detection and measurement of the angular momentum of light," *Physical Review,* vol. 50, no. 2, p. 115, 1936.

[67] L. Allen, M. W. Beijersbergen, R. Spreeuw and J. Woerdman, "Orbital angular momentum of light and the transformation of Laguerre-Gaussian laser modes," *Physical Review A,* vol. 45, no. 11, p. 8185, 1992.

[68] E. Abramochkin and V. Volostnikov, "Beam transformations and nontransformed beams," *Optics Communications,* vol. 83, no. 1-2, pp. 123-135, 1991.

[69] Y. Kozawa and S. Sato, "Focusing of higher-order radially polarized Laguerre-Gaussian beam," *Optical Society of America,* vol. 29, no. 11, pp. 2439-2443, 2012.

[70] A. Sugiura and C. Dermawan, "In traffic jam IVC-RVC system for ITS using Bluetooth," *IEEE Transactions on Intelligent Transportation Systems,* vol. 6, no. 3, pp. 302-313, 2005.

[71] M. L. Sichitiu and M. Kihl, "Inter-vehicle communication systems: a survey," *IEEE Communications Surveys \& Tutorials,* vol. 10, no. 2, pp. 88-105, 2008.

[72] T. Yashiro, T. Kondo, H. Yagome, M. Higuchi and Y. Matsushita, "A network based on inter-vehicle communication," in *Proceedings of the Intelligent Vehicles' 93 Symposium*, 1993.

[73] D.-R. Kim, S.-H. Yang, H.-S. Kim, Y.-H. Son and S.-K. Han, "Outdoor visible light communication for inter-vehicle communication using controller area network," in *2012 Fourth International Conference on Communications and Electronics (ICCE)*.

[74] Z. Xu and B. M. Sadler, "Ultraviolet communications: potential and state-of-the-art," *IEEE Communications Magazine,* vol. 46, no. 5, pp. 67-73, 2008.

[75] M. a. G. Z. Uysal, A. Bekkali, A. Kadri and H. Menouar, "Visible light communication for vehicular networking: Performance study of a V2V system using a measured headlamp beam pattern model," *IEEE Vehicular Technology Magazine,* vol. 10, no. 4, pp. 45-53, 2015.

## List of Publications

### *Journal Papers*


[1] **Arya, Sudhanshu** and Yeon Ho Chung. "Maximal Selective Transmit Diversity for Petahertz Wireless Communications With Continuous Waveform Detector." *IEEE Access* 9 (2021): 118005-118018.

[2] **Arya, Sudhanshu** and Y. H. Chung, "Spectrum Sensing for Optical Wireless Scattering Communications Over Málaga Fading—A Cooperative Approach With Hard Decision Fusion," in *IEEE Transactions on Communications*, vol. 69, no. 7, pp. 4615-4631, July 2021, doi: 10.1109/TCOMM.2021.3073968.

[3] **Arya, Sudhanshu,** Yeon Ho Chung, Wan-Young Chung, Jong-Jin Kim, and Nam-Ho Kim. "Transmit power optimization over low-power Poisson channel in multiuser MISO indoor optical communications." *ICT Express* 7, no. 3 (2021): 361-365.

[4] **Arya, Sudhanshu** and Yeon Ho Chung. "Capacity Maximization Using Nash Bargaining in Indoor Optical Multiuser Interference-Limited Poisson Channel." *IEEE Photonics Journal* 12, no. 6 (2020): 1-12.

[5] **Arya, Sudhanshu** and Yeon Ho Chung. "State-of-the-art ultraviolet multiuser indoor communication over power-constrained discrete-time Poisson channels." *Optical Engineering* 59, no. 10 (2020): 106106.

[6] **Arya, Sudhanshu** and Yeon Ho Chung. "Ann-assisted real-time blind signal detection over time-varying doubly-stochastic poisson channel for indoor optical wireless communications." *IEEE Photonics Journal* 12, no. 5 (2020): 1-18.

[7] **Arya, Sudhanshu** and Yeon-Ho Chung. "Multiuser Interference-Limited Petahertz Wireless Communications Over Málaga Fading Channels." *IEEE Access* 8 (2020): 137356-137369.

[8] **Arya, Sudhanshu** and Yeon Ho Chung. "Novel indoor ultraviolet wireless communication: design implementation, channel modeling, and challenges." *IEEE Systems Journal* 15, no. 2 (2020): 2349-2360.

[9] **Arya, Sudhanshu** and Yeon Ho Chung. "Artificial neural network estimation of data and channel characteristics in free-space ultraviolet communications." *Applied Optics* 59, no. 13 (2020): 3806-3818.

[10] **Arya, Sudhanshu** and Yeon Ho Chung. "A unified statistical model for Málaga distributed optical scattering communications." *Optics Communications* 463 (2020): 125402.

[11] **Arya, Sudhanshu** and Yeon Ho Chung. "High-performance and high-capacity ultraviolet communication with orbital angular momentum." *IEEE Access* 7 (2019): 116734-116740.

[12] **Arya, Sudhanshu** and Yeon Ho Chung. "Amplify-and-forward multihop non-line-of-sight ultraviolet communication in the gamma–gamma fading channel." *Journal of Optical Communications and Networking* 11, no. 8 (2019): 422-436.

[13] **Arya, Sudhanshu** and Yeon Ho Chung. "Generic blind spectrum sensing scheme for all optical-wavelength multi-user free space optical communications." *Optics Communications* 450 (2019): 316-321.

[14] **Arya, Sudhanshu** and Yeon Ho Chung. "A novel blind spectrum sensing technique for multi-user ultraviolet communications in atmospheric turbulence channel." *IEEE Access* 7 (2019): 58314-58323.

[15] **Arya, Sudhanshu** and Yeon Ho Chung. "Spectrum sensing for free space optical communications in strong atmospheric turbulence channel." *Optics Communications* 445 (2019): 24-28.

[16] **Arya, Sudhanshu** and Yeon Ho Chung. "Non-line-of-sight ultraviolet communication with receiver diversity in atmospheric turbulence." *IEEE Photonics Technology Letters* 30, no. 10 (2018): 895-898.

[17] **Arya, Sudhanshu** and Yeon Ho Chung. "Novel Optical Scattering Based V2V Communications with Experimetnal Analysis." *IEEE Transactions on Intelligent Transportation Sytems* (Revision).

[18] Kim, Yeonghae, **Arya Sudhanshu**, and Yeon Ho Chung. "An optimal energy harvesting scheme for simultaneous lightwave information and power transfer over multi-layer turbulence-induced underwater channel." *Optics Communications* 501 (2021): 127382.

[19] Dhatchayeny, Durai Rajan, **Arya Sudhanshu**, and Yeon Ho Chung. "Novel multi-patient biomedical data transmission using CPoLSK modulation technique." *Optics Communications* 480 (2021): 126507.

[20] Aung, Thinn Yu, **Arya Sudhanshu**, and Yeon Ho Chung. "A Dynamic Beamforming Technique for Ultraviolet-Based Indoor Communications." *IEEE Sensors Journal* 20, no. 18 (2020): 10547-10553.

[21] Biswal, Manas Ranjan, **Arya Sudhanshu**, and Yeon Ho Chung. "Effect of turbulence and noise on ultraviolet and mid-infrared spectrum in optical wireless communications." *Photonic Network Communications* (2020): 1-6.

[22] Aung, Thinn Yu, **Arya Sudhanshu**, and Yeon Ho Chung. "Performance dependence of non-line-of-sight ultraviolet communications on atmospheric parameters of the ultraviolet channel." *Optics Communications* 443 (2019): 7-11.

[23] Dhatchayeny, Durai Rajan, **Arya Sudhanshu**, and Yeon Ho Chung. "Patient mobility support for indoor non-directed optical body area networks." *Sensors* 19, no. 10 (2019): 2297.

[24] Dhatchayeny, Durai Rajan, **Arya Sudhanshu**, and Yeon Ho Chung. "Infrared-based multiple-patient monitoring in indoor optical wireless healthcare systems." *IEEE Sensors Journal* 19, no. 14 (2019): 5594-5599.

***International Conferences***


[1] **Arya, Sudhanshu** and Y. H. Chung, "Supervised Learning-Based Noisy Optical Signal Estimation for Underwater Optical Wireless Communications," *2021 Twelfth International Conference on Ubiquitous and Future Networks (ICUFN)*, 2021, pp. 155-158, doi: 10.1109/ICUFN49451.2021.9528775.

[2] **Arya, Sudhanshu** and Y. H. Chung, "Novel Multiuser Indoor Ultraviolet Communications," *GLOBECOM 2020 - 2020 IEEE Global Communications Conference*, 2020, pp. 1-6, doi: 10.1109/GLOBECOM42002.2020.9322102

[3] **Arya, Sudhanshu,** Yeon Ho Chung, and Zabih Ghassemlooy. "Optimum Cooperative Spectrum Sensing Technique for Multiuser Ultraviolet Wireless Communications." In *2020 12th International Symposium on Communication Systems, Networks and Digital Signal Processing (CSNDSP)*, pp. 1-6. IEEE, 2020

[4] **Arya, Sudhanshu** and Yeon Ho Chung. "M-PSK subcarrier intensity modulation with switch-and-stay diversity for NLOS ultraviolet communication." In *TENCON 2018-2018 IEEE Region 10 Conference*, pp. 0524-0529. IEEE, 2018

[5] **Arya, Sudhanshu,** Shivani Teli, Willy Anugrah Cahyadi, and Yeon Ho Chung, UV Propagation Channel for Non-line-of-sight Optical Communication, In *International Conference on Green and Human Information Technology (ICGHIT 2018)*, pp. 21-24, 2018.

[6] Delwar, Tahesin Samira, **Arya Sudhanshu**, Yeon Ho Chung, and Robert Bestak. "Multiuser interference mitigation using CSK in indoor visible light communications." In *2019 International Conference on Green and Human Information Technology (ICGHIT)*, pp. 39-42. IEEE, 2019.

***Domestic Conferences***

[1] **Arya, Sudhanshu,** Thinn Yu Aung, and Yeon Ho Chung, Impact of Pointing Jitter on the Performance of Free-Space Optical Communications over Doubly Stochastic Turbulence Channel, In *The Conference of the Korea Institute of Communications and Information Sciences (KICS)*, pp. 170-172, 2020.

[2] **Arya, Sudhanshu,** Thinn Yu Aung, and Yeon Ho Chung, Ultraviolet Bands for Underwater Communications in Military Applications, In *The Conference of the Korea Institute of Communications and Information Sciences (KICS)*, pp. 13-14, 2019.

[3] **Arya, Sudhanshu,** Thinn Yu Aung, and Yeon Ho Chung, A Novel Ultraviolet based Unmanned Aerial Vehicle Communication Technique for Military Applications, In *The Conference of the Korea Institute of Communications and Information Sciences (KICS)*, pp. 79-81, 2019.

[4] Ji Eun Kwak, **Arya, Sudhanshu,** and Yeon Ho Chung, A Low-Complexity CNN-based Image Classification Algorithm for Vehicular Applications, In *The Conference of the Korea Institute of Communications and Information Sciences (KICS)*, pp. 73-75, 2021

[5] Jung Min Park, **Arya, Sudhanshu,** Yeong Hae Kim, and Yeon Ho Chung, Noise Signal Analysis based on Artificial Neural Network, In *The Conference of the Korea Institute of Communications and Information Sciences (KICS)*, pp. 26-28, 2020.

[6] Yeong Hae Kim, Jung Min Park, **Arya, Sudhanshu,** and Yeon Ho Chung, Analysis of Optimal Energy Harvesting Time for Time Splitting based SLIPT, In *The Conference of the Korea Institute of Communications and Information Sciences (KICS)*, pp. 22-25, 2020

[7] Thinn Yu Aung, **Arya Sudhanshu** and Yeon Ho Chung, Performance Analysis of Ultraviolet based Underwater Communication Systems, In *The Conference of the Korea Institute of Communications and Information Sciences (KICS)*, pp. 15-17, 2019.

[8] Biswal Manas Ranjan, **Arya Sudhanshu**, and Yeon Ho Chung, Performance Analysis of Ultraviolet based Underwater Communication Systems, In *The Conference of the Korea Institute of Communications and Information Sciences (KICS)*, pp. 82-84, 2019.

[9] Aung, Thinn Yu, **Arya Sudhanshu**, and Yeon Ho Chung, Performance Dependence of the Ultraviolet Communication Link on Rayleigh Scattering Optical Depth, In *The Conference of the Korea Institute of Communications and Information Sciences (KICS)*, pp. 51-53, 2018.

[10] Dhatchayeny, Durai Rajan, **Arya Sudhanshu**, and Yeon Ho Chung, Multiple Patient Vital Sign Transmission using Visible Light Communication, In *The Conference of the Korea Institute of Communications and Information Sciences (KICS)*, pp. 80-82, 2018.

[11] Willy Anugrah Cahyadi, **Arya Sudhanshu**, and Yeon Ho Chung, Camera Focul Techniques in Optical Camera Communication, In *The Conference of the Korea Institute of Communications and Information Sciences (KICS)*, pp. 74-76, 2018.